2014-04-21

Lateral Current Density Variation in PEM Fuel Cells with Interdigitated Flow Fields

Song Luo
University of Miami, mysongluo@gmail.com

UNIVERSITY OF MIAMI

LATERAL CURRENT DENSITY VARIATION IN PEM FUEL CELLS WITH INTERDIGITATED FLOW FIELDS

By

Song Luo

A DISSERTATION

Submitted to the Faculty
of the University of Miami
in partial fulfillment of the requirements for
the degree of Doctor of Philosophy

Coral Gables, Florida

May 2014

UNIVERSITY OF MIAMI

A dissertation submitted in partial fulfillment of
the requirements for the degree of
Doctor of Philosophy

LATERAL CURRENT DENSITY VARIATION IN PEM FUEL CELLS WITH INTERDIGITATED FLOW FIELDS

Song Luo

Approved:

_____ Hongtan Liu, Ph.D. Professor of Mechanical and Aerospace Engineering	_____ Xiangyang Zhou, Ph.D. Associate Professor of Mechanical and Aerospace Engineering
_____ Na Li, Ph.D. Assistant Professor of Mechanical and Aerospace Engineering	_____ M. Brian Blake, Ph.D. Dean of the Graduate School
_____ Wangda Zuo, Ph.D. Assistant Professor of Civil, Architectural, and Environmental Engineering	

SONG LUO (Ph.D., Mechanical Engineering)

Lateral Current Density Variation in PEM Fuel Cells with Interdigitated Flow Fields (May 2014)

Abstract of a dissertation at the University of Miami.

Dissertation supervised by Professor Hongtan Liu.
No. of pages in text. (138)

Proton exchange membrane (PEM) fuel cell is regarded as one of the most promising power systems for the future vehicles. When supplied with air and hydrogen, PEM fuel cells show various advantages, such as quick start-up, high efficiency and pollution-free. It is well known that the current distribution in a PEM fuel cell is not uniform. Although both experimental and modeling studies on current distributions have been conducted for parallel and serpentine flow fields, there are no experimental measurements of lateral current density distribution for the interdigitated flow field. The study of lateral current density variation in this dissertation is essential to PEM fuel cells with interdigitated flow field design optimizations.

Firstly, separate *in situ* measurements of current densities under the inlet channel, the land and the outlet channel in a PEM fuel cell with a single interdigitated flow field are conducted. Partially-catalyzed membrane electrolyte assembly (MEA) method is used to measure the local current density separately. The experimental results show that the local current density varies drastically in the lateral direction. In the lower current density region, the current density under the land is higher than that under the inlet channel. However, in the higher current density region, the current density under the inlet channel is higher than that under the land. The results have both similarities and

differences with those for parallel flow field and serpentine flow field [1, 2]. One significant difference is the large difference between the inlet and outlet channels. The local current densities under different cathode operation conditions are measured to study if the operation conditions affect the local current densities variations significantly. The experimental results show that different cathode flow rates and cathode back pressures have negligible effect on the pattern of relative magnitudes of local current densities among the three different areas, and the cathode humidification temperature has a drastic effect on the inlet channel current density. The local electrochemical areas (ECA) are also measured by cyclic voltammetry (CV) technique. The experimental results show that ECA under the outlet channel is lower than that under the inlet channel, and ECA under the land is the highest.

Furthermore, the lateral current distribution of PEM fuel cells with a single interdigitated flow field is studied with higher resolution. In this study, partially-catalyzed MEA method is also used measure the lateral current under seven locations separately. Different flow rates are applied and similar lateral current distribution tendency is obtained. At most typical PEM fuel cells operation voltages, the current densities under the land are the highest and the current densities under the inlet channel are much higher than that under the outlet channel. Then, CV and electrochemical impedance spectroscopy (EIS) tests are conducted to investigate the underlying reasons for the non-uniform lateral current density distribution. CV and EIS results are consistent with each other provide the mechanisms of the lateral current density variations.

Moreover, a two-dimensional model is developed to illustrate the mechanism of the variations in lateral current densities in PEM fuel cells with interdigitated flow fields.

Comparing with the previous modeling work, the lateral ECA distribution from the experimental study is integrated into the model, which makes this model more realistic. The modeling results agree with the experimental results very well. The modeling results show that the reactant concentration is decreasing along the lateral direction. Besides, it also shows that the lateral current density is not uniform. The current under the inlet channel is much higher than that under the outlet channel, and the current under the land is the highest in typical cell operation voltages. In addition, the dimensions of the land with, the outlet channel width and the under land gas diffusion layer (GDL) thickness are studied. The modeling results show that for interdigitated flow fields, wider lands and narrower outlet channels with thinner GDL are preferred.

Dedicated to my parents

Who have given me unconditional love

and

have raised my spirits to go on every adventure

ACKNOWLEDGEMENT

First and foremost, I want to express my deepest gratitude to my Ph. D. advisor and dissertation committee chairperson, Dr. Hongtan Liu. Dr. Liu has entrusted me with great degree of autonomy to explore a variety of doctoral topics, and has given me fruitful advice on a consistent basis with a positive, encouraging attitude. Under his guidance, I have learned to be not only enthusiastic to broaden my academic horizons, but also courageous to go beyond superficial phenomena to grasp fundamental mechanisms. In general, Dr. Liu enlightens me to pursue research rigor throughout my scientific research. Dr. Liu is also a life inspiration, from whom I have learned to appreciate an upright, optimistic life attitude. I could not have accomplished my Ph. D. work without his continuous support.

Meanwhile, I would like to thank the rest of my Ph. D. committee members, Dr. Xiangyang Zhou, Dr. Na Li and Dr. Wangda Zuo, for offering worthy suggestions and feedbacks. Their valuable inputs make this work integrated.

I am also thankful to the Department of Mechanical and Aerospace Engineering of the University of Miami for their financial and educational support to my Ph. D. study.

I am grateful to the China Scholarship Council for offering the State Scholarship Fund during the course of my Ph. D. study.

I would like to thank Dr. Jin Chen from Chongqing University for encouraging me to pursue my Ph. D. degree.

I would like to thank all my brilliant colleagues, Dr. Saif Matar, Dr. Hidetaka Taira, Dr. Shan Jia and Mr. Xuyang Zhang. Their comments and constructive criticisms have

complemented my work to a large degree. This work has benefited greatly from our inspiring academic discussions and delightful casual conversations.

Last but not least, I would like to thank my family for supporting me in every possible way for the past years. Without their encouragement and sacrifice, none of this work would have been happened.

TABLE OF CONTENTS

Page

LIST OF FIGURES

LIST OF TABLES

LIST OF NOMENCLATURE

a_v	Specific reaction area $(1/m)$
C	Molar concentration (mol/m^3)
CHT	Cathode humidification temperatures (K)
CV	Cyclic Voltammetry
D	Diffusivity (m^2/s)
d	Diffusion driving force $(1/m)$
D^*	Multicomponent Fick diffusivities$(\mathrm{m}^2/\mathrm{s})$
E_{ocv}	Open circuit voltage (V)
ECA	Electrochemical areas (m^2/kg)
EIS	Electrochemical impedance spectroscopy
F	Faraday constant $(96{,}487\ C/mol)$
g^0	Gibbs free energy under standard-state conditions(kJ/mol)
GDE	Gas diffusion electrode
GDL	Gas diffusion layer
h	Enthalpy (kJ/mol)
j_0	Exchange current density (A/m^2)
j	Current density (A/m^2)
J	Current density (A)
j_L	Limiting current density (A/m^2)
M	Molar mass (kg/mol)
MEA	Membrane electrolyte assembly

p	Pressure (Pa)
PEM	Proton exchange membrane
$[Pt]$	Platinum loading ($0.4\ mg/cm^2$)
R	Universal gas constant ($8.314\ J/(mol \cdot K)$)
RH	Relative humidity
t	Thickness (m)
T	Temperature (K)
TPB	Triple phase boundaries
$\boldsymbol{u}$	Velocity field (m/s)
W	Width (m)

Greek symbols

ρ	Density (kg/m^3)
ε_p	Porosity
κ	Permeability (m^2)
α_c	Anodic transfer coefficient
α_c	Cathodic transfer coefficient
η	Over potential (V)
η_p	Pumping efficiency (0.85)
Φ	Potential (V)
μ	Viscosity ($Pa \cdot s$)
σ	Ionic and electrical conductivity (S/m)
x	Mole fraction

ω	Mass fraction

Superscripts

a	Anode
c	Cathode
C	Channels
IC	Inlet channel
L	Land
OC	Outlet channel
ref	Reference
sat	Saturation
x	x direction
y	y direction

Subscripts

acl	Anode catalyst layer
ccl	Cathode catalyst layer
cl	Catalyst layer
g	GDL
m	Membrane phase
s	Solid phase
i, j, k	Species

CHAPTER 1

INTRODUCTION

1.1 Background

In recent years, the world population expands significantly. One of the primary effects of the large population is the increasing world energy consumption as shown in Fig. 1.1. Usually, the energy consumption is accompanied with environmental pollutions. Fig. 1.2 shows carbon dioxide emissions by different fuel types. It can be seen that the emissions from consuming coals and liquids are the major emission sources. Nowadays, people are more concerning about human health, environment protections and energy recycling, so it is urgent to impel the development of renewable energy.

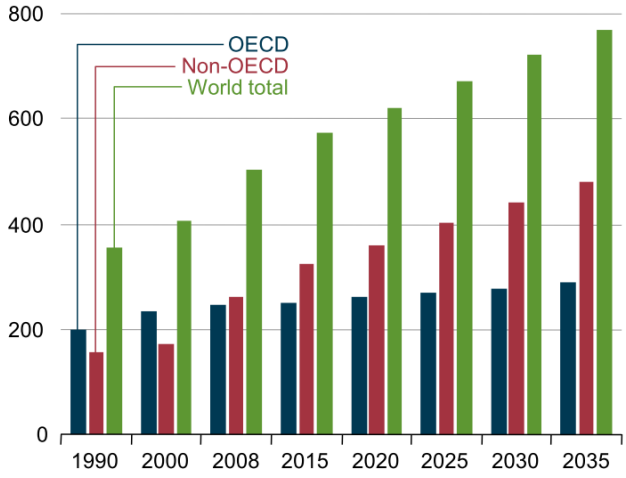

Fig. 1.1 World energy consumption, 1990-2035 (quadrillion Btu) [3]

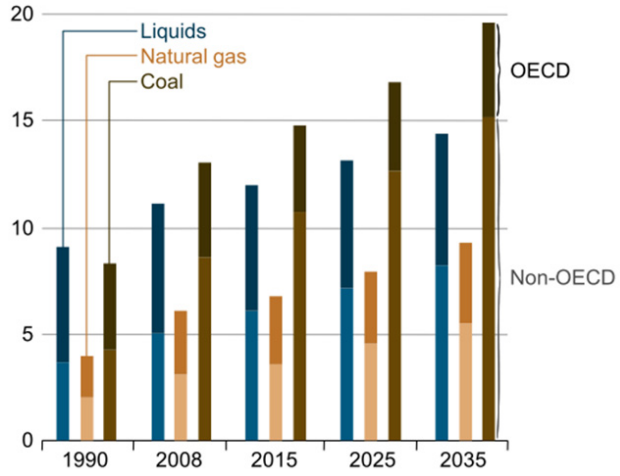

Fig. 1.2 OECD and non-OECD energy-related carbon dioxide emissions by fuel type, 1990-2035 (billion metric tons) [3]

Many types of renewable energy have been developed both by industries and academia, such as solar, wind, geothermal and hydropower, etc. However, they are mainly used in the electricity plants. While in the portable devices and transportation application fields, they are not the optimal options. Instead, fuel cells approach the vision of the whole world.

1.2 An introduction to fuel cells

The first fuel cell is developed in 1839 by William Grove as shown in Fig. 1.3. Under the extra power supply condition, the water can be electrolyzed into hydrogen and oxygen as shown in Fig. 1.3 (a). It is reversible to the process shown in Fig. 1.3 (b), in which case electrochemical reactions occur at the interfaces of the two electrodes. The hydrogen and oxygen are combined together into water. During this combining process, current can be generated [4].

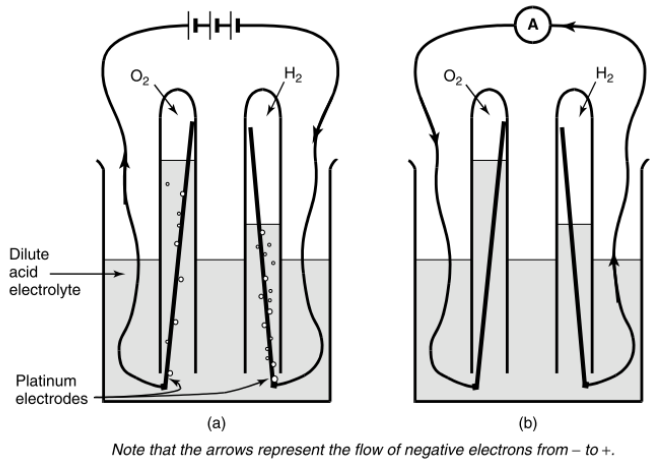

Fig. 1.3 (a) Water is electrolyzed. (b) Current is generated. [4]

1.3 Fuel cell types and applications

Although many types of novel fuel cells are proposed nowadays, typically there are five main fuel cells as shown in Table 1.1. Different cells are mainly distinguished by various electrolytes [5]. In each type of fuel cell, the charge carrier may be different. In addition, each type of fuel cell is applicable within a range of operation temperature. All these different characteristics lead to different applications.

In this study, proton exchange membrane (PEM) fuel cell is focused. Although PEM fuel cell has many disadvantages, its advantages attract more attention. The low emission and simplicity make PEM fuel cell a practical option for environmental clean vehicles and portable devices. The details of PEM fuel cell advantages and disadvantages will be discussed in later sections.

Table 1.1 Main fuel cell types [4-6]

Fuel cell	Proton Exchange Membrane (PEMFC)	Phosphoric Acid (PAFC)	Alkaline (AFC)	Molten Carbonate (MCFC)	Solid Oxide (SOFC)
Electrolyte	Polymer membrane	Liquid H_3PO_4	Liquid KOH	Molten carbonate	Ceramic
Charge carrier	H^+	H^+	OH^+	CO_2^{3-}	O_2^-
Operating temperature (℃)	80	200	60-220	650	600-1000
Catalyst	Pt	Pt	Pt	Nickel	Ceramic
Cell components	Carbon based	Carbon based	Carbon based	Stainless based	Ceramic based
Fuel compatibility	H_2 methanol	H_2	H_2	H_2, CH_4	H_2, CH_4, CO
Application	-Vehicles -Mobile	-Large numbers of 200 KW CHP system	-Space vehicles	-Medium to large scale of CHP system, up to MW capacity	-All sizes CHP system

There are three major types of fuel cells regarding to the applications: portable, stationary power stations and transport [7]. Table 1.2 compares the three types of applications [7]. The power range of the stationary fuel cells is the much larger than that of the portable fuel cells. The transport fuel cells power range stays between these two types of fuel cells.

Table 1.2 Fuel cells applications [7]

Application type	Portable	Stationary	Transport
Definition	Designed to be moved	-Provide electricity -Not designed to be moved	-Provide propulsive power or range extension to a vehicle
Typical power range	5W-20KW	0.5KW-400KW	1KW-100KW
Typical technology	PEMFC DMFC	MCFC PAFC PEMFC SOFC	PEMFC DMFC
Examples	-Non-motive APU -Military applications -Personal electronics	-Uninterruptible power supplies (UPS)	-Trucks and buses

1.4 Summary of advantages and disadvantages

Advantages [4, 5]:

- Efficiency

For traditional internal combustion engine, a long energy consumption process is needed in order to obtain electricity. The chemical energy will be converted to heat, then mechanical work, and finally electricity. During this process, energy lost is a serious problem, which is the main reason for the low efficiency of internal combustion engine. Comparing with internal combustion engine, fuel cells produce electricity in another manner. The electricity can be converted from chemical energy directly. This simple and short conversion process can lead to a much higher efficiency than the traditional internal combustion engine.

- Simplicity

The fuel cells components and electrochemical reactions are very simple, which will be explained in the later section in this chapter. In typical fuel cells, there are few moving components, which can result in a reliable and silent fuel cell system.

- Low emission

Fuel cells are environmental friendly energy converting device. Any poisoning or undesirable products will not be produced or emitted by fuel cells. Especially, for hydrogen-oxygen PEM fuel cells, only water will be produced finally.

Disadvantages [8]:

- High cost

The main cost of fuel cells is coming from proton exchange membrane and catalyst Pt [8, 9]. Fig. 1.4 shows the fuel cell cost break down [10].

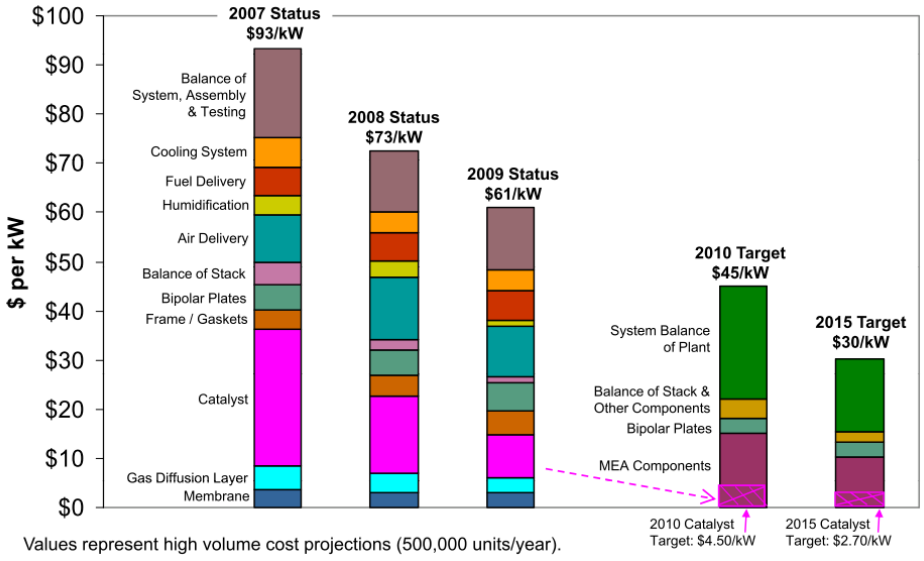

Fig. 1.4 Fuel cell cost break down [10]

- Durability

To commercialize fuel cells, the lifetime is required to reach 5000 operation hours for mobile and 40000 hours for stationary applications with less than 10% performance decay. However, these could only be obtained in the lab test now. Most fuel cells performance decay significantly after 1000 hours operation [8, 9, 11, 12]. Short durability can weaken preference of potential customers, and then hinder the commercialization development of fuel cells.

1.5 Basic electrochemical reactions of PEM fuel cells

Fig. 1.5 shows the details of electrochemical reactions of a typical proton exchange membrane (PEM) fuel cell. The operation of a PEM fuel cell insists of four major steps [5].

- Reactant transport

Hydrogen and oxygen are needed to produce electricity for PEM fuel cells. Delivering gases efficiently to the reaction sits is extremely important for PEM fuel cell performance optimization. The flow plates and the porous medias at both anode and cathode sides play an important role in gases distribution. The flow plate consists of flow channels and lands. The dimensions of channels and lands can affect the flow distribution by affecting the flow pressure and velocity. Besides, different flow patterns can lead to various flow distributions. Porous media can influent the flow distribution significantly. The porosity and permeability can impact the fluid mechanics properties, such as pressure, velocity, mass diffusion, convection, etc.

- Electrochemical reactions

After gases delivery, electricity will be generated by electrochemical reactions. At anode catalyst/membrane interface, protons will be produced by removing electrons from hydrogen. The half-cell process at anode side is shown as in Eq. (1.1). At cathode catalyst/membrane interface, electrons will combine with the oxygen, and water will be produced. The half-cell process at cathode side is shown as in Eq. (1.2). The overall reaction is shown in Eq. (1.3). The ionic and electronic conductions will be discussed in the next step.

$$Anode\ side: \quad H_2 \rightarrow 2H^+ + 2e^- \tag{1.1}$$

$$Cathode\ side: \quad \frac{1}{2}O_2 + 2H^+ + 2e^- \rightarrow H_2O \tag{1.2}$$

$$Overall: \quad H_2 + \frac{1}{2}O_2 \rightarrow H_2O \tag{1.3}$$

- Ionic and electronic conduction

Anode and cathode is separated by proton exchange membrane. Only protons can be transported through the proton exchange membrane. However, electrons produced at anode side have to go through the outside circuit. The electronic conduction in a circuit is much easier than the ionic conduction in a membrane. So the ionic conduction is one of the major impedances in a PEM fuel cell.

- Product removal

For hydrogen-oxygen PEM fuel cells, only water will be produced at cathode side. Usually, product removal is not a significant issue. However, under high current density operation condition, a large amount of water will lead to undesirable flooding problem.

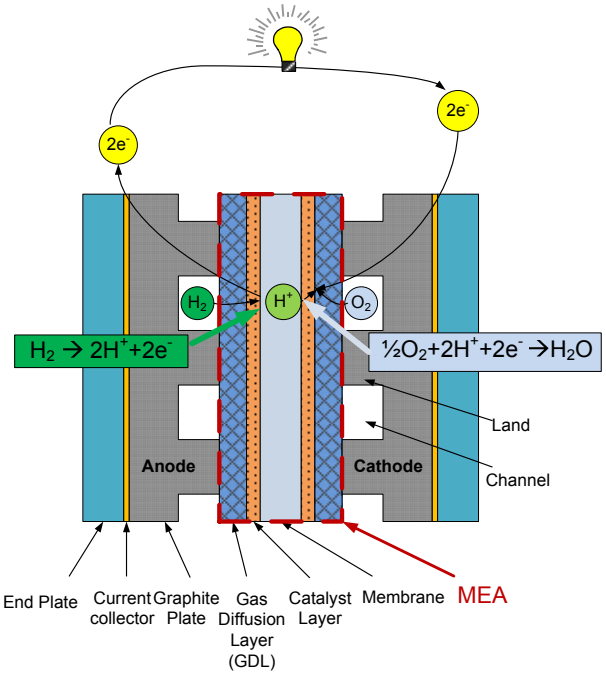

Fig. 1.5 Basic electrochemical reactions of PEM fuel cells

The performance of PEM fuel cells can be represented by a graph of current-voltage characteristics [5], which is called polarization curve. A sample of polarization curve is shown in Fig. 1.6 [13]. In order to compare the performance for different PEM fuel cells, current normalization technique is needed. The most practical way is to normalize the current by the electrochemical reaction area. The current produced by unit electrochemical reaction area is called current density, which is the horizontal axis in the polarization curve.

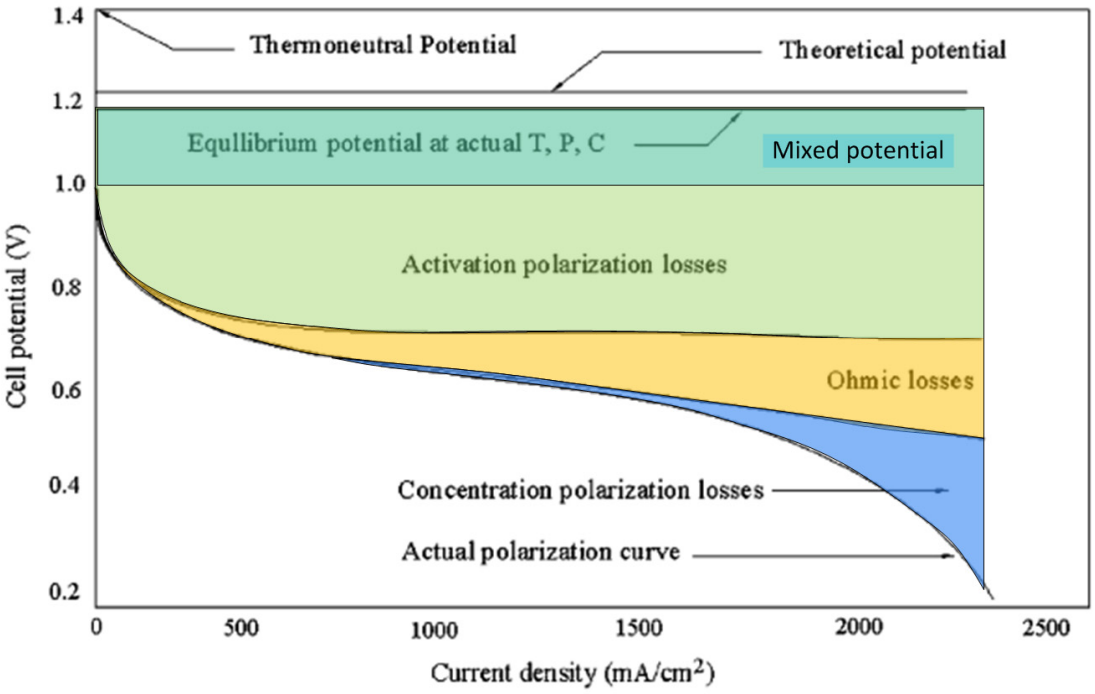

Fig. 1.6 A sample of polarization curve of PEM fuel cells [13]

The entire heat released from the reaction at constant pressure is expressed as enthalpy change Δh, and the fuel cell potential regarding to the enthalpy change is named as thermoneutral potential E_t [14]:

$$E_t = -\frac{\Delta h}{nF} \tag{1.4}$$

The theoretic potential E^0 is related to the maximum electrical work output, which is the Gibbs free energy Δg^0 under standard-state conditions [5, 14]:

$$E^0 = -\frac{\Delta g^0}{nF} \tag{1.5}$$

Under non-standard-state conditions, the equilibrium potential of PEM fuel cells is defined by Nernst equation [5]:

$$E = E^0 - \frac{RT}{nF} ln \frac{\prod a_{products}^{vi}}{\prod a_{reactants}^{vi}} \quad (1.6)$$

The mixed potential is mainly due to the fuel crossover between anode and cathode [15]. The hydrogen oxidation reaction (HOR) in the cathode side and the oxygen reduction reaction (ORR) in the anode side will decrease the open circuit potential (OCP) from theoretical potential to a practical OVP, around 0.95 V to 1.0 V [15].

There are three major losses in PEM fuel cells [4]. In the low current density region, the dominating loss is the activation loss which is due to the slowness of reactions [4]. The activation loss can be calculated by Tafel equation [5]:

$$\eta_{act} = \frac{RT}{\alpha nF} \ln \frac{j}{j_0} \quad (1.7)$$

Where j is current density, j_0 is the exchange current density, and α is the reactant activity.

In the intermediate current region, the dominating loss is ohmic loss which is due to the ohmic resistance of a fuel cell. Two types of charges exist in PEM fuel cells: electrons and ions, and it is more difficult to transfer the ions. The ohmic loss is calculated as [5]:

$$\eta_{ohmic} = JR \quad (1.8)$$

And in the high current density region, concentration loss is the dominating loss which is due to the nonsufficient reactants at the reaction sites [5]. Concentration loss can be calculated as [4]:

$$\eta_{conc} = \frac{RT}{nF} \ln \frac{j_L}{j_L - j} \quad (1.9)$$

So the practical fuel cell output voltage is listed as [5]:

$$V = E - \eta_{act} - \eta_{ohmic} - \eta_{conc} \tag{1.10}$$

1.6 Fuel cell components

The components of a typical PEM fuel cell is shown in Fig. 1.7 [6]. All the components are sandwiched together by bolts. The functions of each component will be explained as followings.

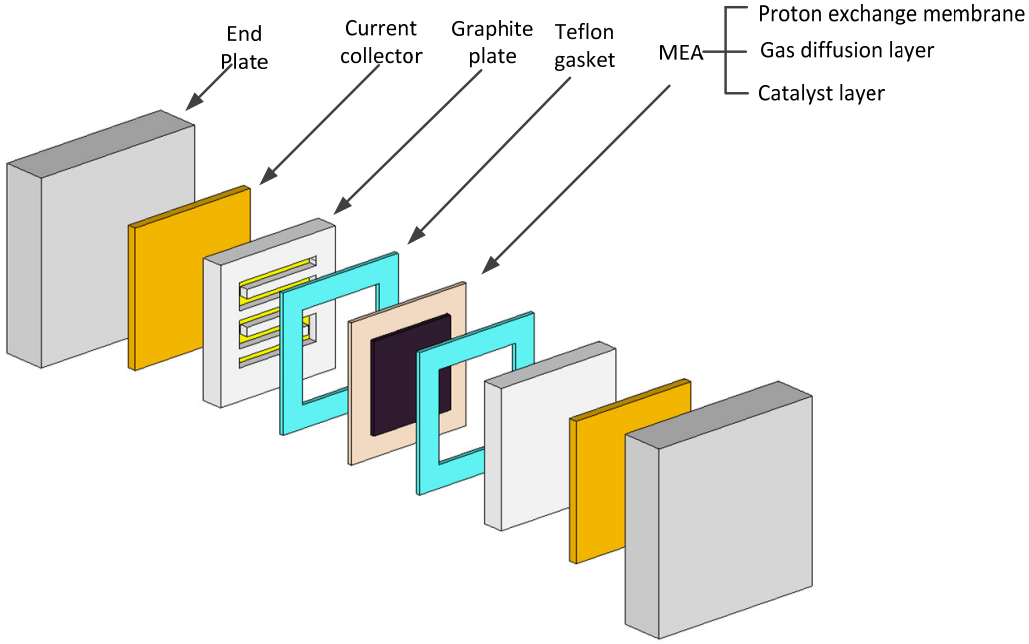

Fig. 1.7 Components of a typical PEM fuel cell [6]

1.6.1 Flow field

Flow field mainly provides two functions. First, flow field is used to feed gases and remove the electrochemical reaction products. In addition, flow field offers electron conduction paths for fuel cells [5, 6]. Although a large number of flow field designs have

been proposed by researchers, nowadays, the most widely used three types of flow fields are shown in Fig. 1.8 [5, 16].

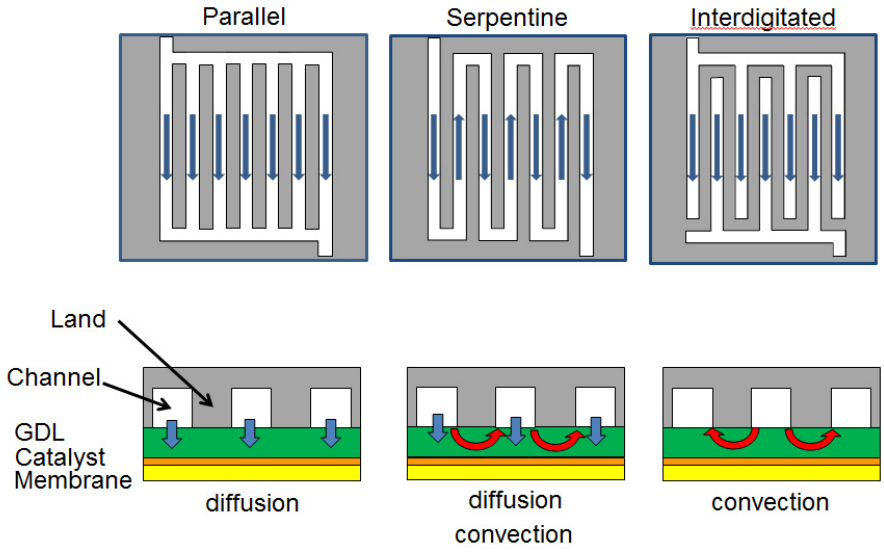

Fig. 1.8 Three types of typical flow field designs [5, 6]

Parallel flow field is relatively simple. The reactants move along the straight channels in parallel and it is distributed to MEA by diffusion. Since the inlet and outlet are connected, parallel flow field shows low pressure drop from inlet and outlet. However, one of the disadvantages is the non-uniform flow distribution. This could lead to non-uniform electrochemical reactions inside a PEM fuel cell. So water accumulation is also non-uniform.

Serpentine flow field is the most common used flow pattern. For the serpentine flow filed, there is only one flow path. So the pressure difference occurs between adjacent channels. This pressure difference generates the convection flow, so the reactant is distributed by both diffusion and convection. Since there is only one flow channel, all the

water inside the flow channel has to be expelled out along with the gas. The water removal ability is much better comparing with the parallel flow field. The significant disadvantage of serpentine flow field is the larger pressure drop along the flow direction. The pressure drop will become much bigger for the fuel cells with larger sizes.

For the interdigitated channel, both the inlet and the outlet are divided into several channels, and they finally meet the dead-end. So, the reactant is forced from inlet channels to outlet channels by convection. It can provide a better water management, while accompanying with significant pressure drop.

1.6.2 Membrane electrolyte assembly

Membrane electrolyte assembly (MEA) is the core part of a PEM fuel cell. It contains a proton exchange membrane, gas diffusion layer (GDL) and catalyst layer. Each component will be introduced as followings.

- Proton exchange membrane

Proton exchange membrane serves as electrolyte in PEM fuel cells. The electrolyte should meet the following requirements [5]:

  - High ionic conductivity
  - Low electronic conductivity
  - High stability to the oxidation and reduction reactions
  - Easy to be manufactured

Several electrolytes have been developed regarding to different fuel cells types, such as polymer, aqueous and ceramics. For polymer electrolyte, the most widely used material is Nafion® from Dupont. The main purpose of the Nafion® proton exchange membrane is to conduct protons from anode to cathode. Typical thickness of a proton

exchange membrane is about 10 to $100\,\mu m$ [8]. Nafion® membrane has a polytetrafluoroethylene (Teflon) backbone with sulfonic acid (SO_3^-) functional group at the end. An example of this structure is as shown in Fig. 1.9 [4]. Teflon backbone provides the mechanical strength for the Nafion® membrane, while the SO_3^- group makes the ionic conduction possible. With the presence of enough water, the protons can move freely from one acid site to another.

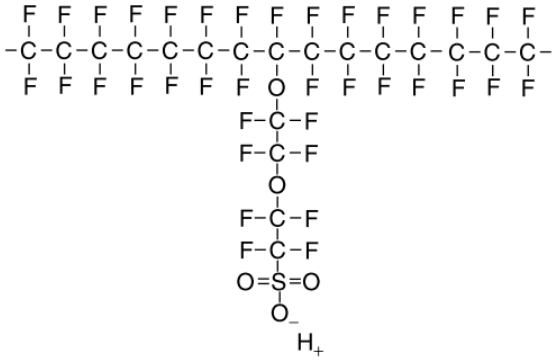

Fig. 1.9 Example structure of membrane [4]

- Gas diffusion layer (GDL)

Gas diffusion layer (GDL) is a porous diffusion media with a typical thickness of 100 to 300 μm . GDL can provide multi-functions to fuel cells [8].

- Electronic path
- Gas transport
- Protection of catalyst

Many types of GDLs have been developed, and among which, two of the most popular GDLs are carbon cloth and carbon paper as shown in Fig. 1.10 [17].

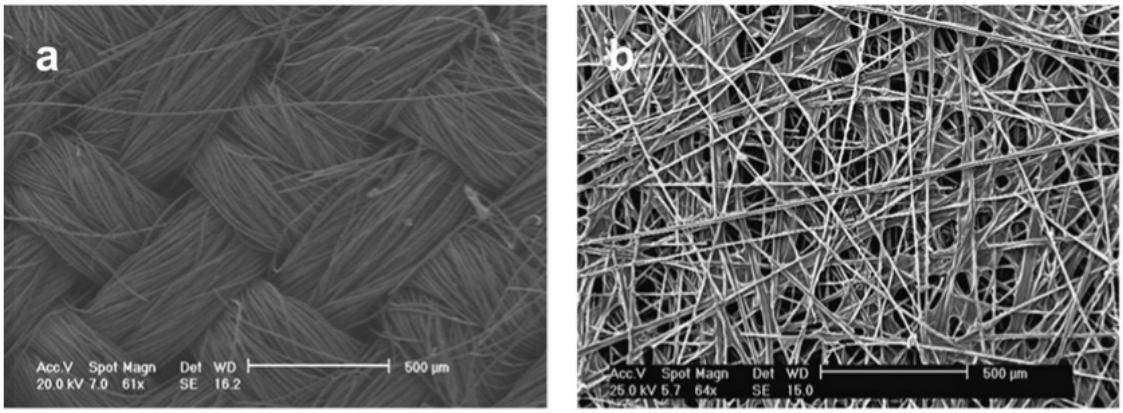

Fig. 1.10 SEM image of two types of GDLs. (a) Carbon cloth-Ballard 1071 HCB; (b) Carbon paper –Toray H-060 [17]

- Catalyst

In fuel cells, the electrochemical reactions only occur at the places where the gas pores, catalyst and membrane are in contact. This region is called triple phase boundaries (TPB) as shown in Fig. 1.11 schematically [5]. In order to make the reaction happen, the gas pores are needed to provide the reactant. Catalyst particle is essential to enhance the reaction and to conduct the electrons. In addition, membrane is needed to provide the protons.

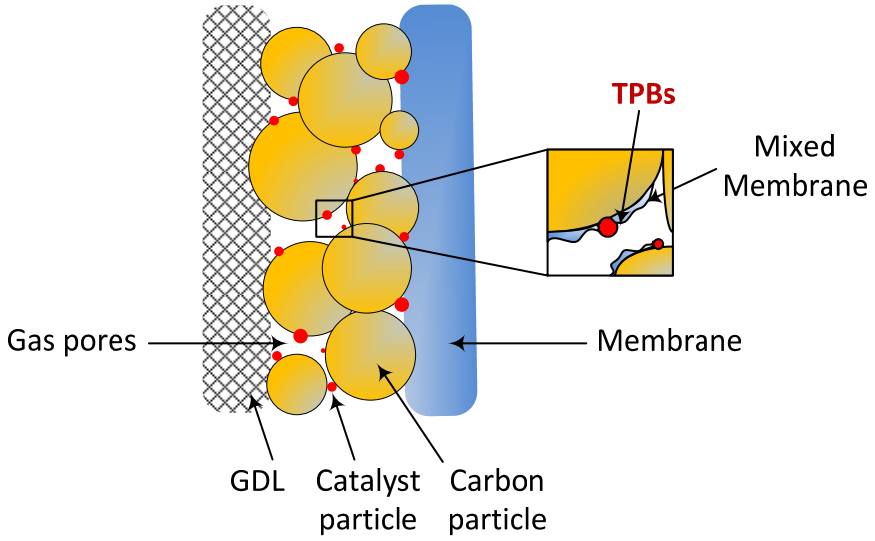

Fig. 1.11 Schematic of electrochemical reaction sites (Triple phase boundaries) [5]

The basic requirements of catalyst are [5]:

- High electrical conductivity
- Low corrosion
- High catalytic activity
- High porosity

Platinum or platinum alloys can be used as catalyst [8]. In PEM fuel cells, platinum is the most common catalyst. This precious catalyst contributes to the high cost of PEM fuel cells.

1.6.3 Other parts

- Current collector

The current collector is made of copper plate coated with a thin layer of gold. The current collector is electrical connected with the graphite plate while electrical isolated

from the end plate. This special design can provide a complete electrical path for electrons.

- Teflon gasket

  Teflon gasket is used to prevent any possible gas leakage.

- End plate

  Two end plates can be used to assemble the whole fuel cells together by bolts. Proper mechanical strength can be provided by the end plates.

1.7 Outline of this dissertation

Nine chapters are organized in this dissertation. Chapter 1 provides basic knowledge about fuel cells. A comprehensive literature review on different research topics is presented in Chapter 2. Chapter 3 presents the objective of this study. The experimental methodologies are introduced in Chapter 4. Chapter 5 is an experimental study on the direct measurements of current densities under the channels and the land in a PEM Fuel Cell with an interdigitated flow field. Further, Chapter 6 studies the lateral current variation in a PEM Fuel Cell with an interdigitated flow field. A two-dimensional PEM fuel cell model is presented in Chapter 7. Chapter 8 shows the numerical results of current variation in interdigitated flow field and the numerical optimization results. Finally, Chapter 9 states the conclusions of this dissertation and future research suggestions.

CHAPTER 2

LITERATURE REVIEW

Since the early development of PEM fuel cells, great efforts have been devoted to various research topics by many researchers. Both experimental and numerical studies are conducted, which can provide a comprehensive understanding of PEM fuel cells, and guide the future performance optimizations. In this literature view, all the previous works are classified by different research topics.

2.1 Current distribution

2.1.1 Experimental study

Significant advancements have been made in the proton exchange membrane (PEM) fuel cell technology in the recent decade. In order to further improve its performance and durability flow field design optimization for PEM fuel cell is essential and the knowledge of the local current density variations is essential for such design optimizations. Significant efforts have been devoted by researchers to measure the current distribution in PEM fuel cells with different devices and techniques.

Printed circuit board (PCB) devices were adopted by researchers to measure local current distribution in PEM fuel cells [18, 19]. Cleghorn et al. [18] applied a PCB device to measure the current distribution in a PEM fuel cell with a serpentine flow field. The anode current collector and flow plate were segmented into eighteen small parts, each of which contained both channels and lands. The effects of cathode flow rate, anode and cathode humidity were studied. Brett et al. [19] applied a similar technique to a PEM fuel

cell with one single flow channel, which was segmented into ten small parts. The current distribution along the single flow channel was measured.

Stumper et al. [20] described three methods to measure current distribution in a PEM fuel cell with serpentine flow field, i.e. the method of partial membrane electrode assembly (MEA), the sub-cell method and mapping method. The partial MEA method was relative simple and easy to implement. The authors used three different MEAs, and each of which covered three different parts of the flow plate. The sub-cell method could provide the local current density within a smaller region compared with the partial MEA method. Liu et al. [21] applied this technique to study the current density distribution in a PEM fuel cell with a serpentine flow field. Twelve small segments were adopted on the anode side, each of which contained three channels and four lands. The effects of different operation conditions were studied. The mapping technique could be used to study the dynamic performance of fuel cells. Brett et al. [19] conducted experiments to obtain the real-time current responses. Naponen et al.[22] also use this technique to study the current distribution in a free-breathing PEM fuel cell with a parallel flow field. There were no segments on the cathode side flow field plate; however, the lands of the cathode flow field plate were made of stainless steel coated with gold metal while other parts were made of non-conductive materials.

Wilkinson et al. [23] obtained current density in a PEM fuel cell with serpentine flow field by measuring the local temperature. It was shown that the current density was proportional to the local temperature change with time. By the correlations provided by the authors, it was possible to obtain the current density distribution. The simplicity of

temperature measurement by thermal couples made this method easy to implement. The authors measured the current distribution along flow channels direction.

Some researchers proposed techniques based on magnetic effect to measure the current density [24, 25]. Wieser et al. [24] reported the open-loop Hall sensor technique to map the local current density in a PEM fuel cell with a parallel flow field. Both the anode flow plate and the electrode were segmented. The hall sensors were placed under the flow field plate. Geiger et al. [25] demonstrated the closed-loop Hall sensor method to measure the local current in a direct methanol fuel cell with a serpentine cathode flow field. It was stated that the closed-loop Hall sensor technique had various advantages compared with the open-loop technique, such as higher accuracy, easier calibration and better linearity.

Sun et al. [26] developed a simple technique to measure the current density in a PEM fuel cell with serpentine flow field by using a measurement gasket, which was placed between the flow plate and the MEA. Local current distribution was obtained by measuring the current under 21 measuring strips. Each strip contained two half flow channels and one land. One of the main advantages was that it was inexpensive and easy to implement. The results showed that gas flow rate, humidity and cell temperature affected fuel cell performance significantly.

All of the studies mentioned above [18-26] measured current variations either along the flow channels or in segments of the fuel cell containing both channels and lands, but none were able to differentiate the current densities under the land and the channel. Yet, due to the different structures and different mass transport mechanisms under the channel and the land, it is obvious that the current density can be very different under these

regions. Thus it is very important to know the current densities in different regions in the lateral direction in order to design optimized flow fields for PEM fuel cells.

Using an indirect technique, Freunberger et al. [27, 28] obtained the local current density variations in the lateral direction by measuring the local potential under the channel and the land. Golden wires were placed between the catalyst layer and the gas diffusion layer (GDL), and the local electrical potential under channel and land could be probed separately. By Laplace's equation and Ohm's Law, the current density under the channel and land could be calculated separately. The authors concluded that when the fuel cell load was decreased, the maximum current peak would shift from the channel to the land.

Wang and Liu [1] used a partially catalyzed MEA method to separately measure the current densities under the land and channel in PEM fuel cell with a parallel flow field that had two channels and one land. The results showed that the current under the land area is significantly higher than that under the channel area. It was further shown by Higier and Liu [29] that the main reason for such a significant difference is the much higher electrochemical area (ECA) under the land area due to the direct compression from the land structure of the flow field plate. In a similar manner, current densities under the land and channel were separately measured in a PEM fuel cell with a serpentine flow field [2].

2.1.2 Modeling study

Few experimental studies have been conducted to measure the current density distribution in lateral direction in the interdigitated flow fields, and most researchers have

resorted to models to simulate the current density distribution in the interdigitated flow fields.

Kazim et al. [30] used a two-dimensional (2D) model to compare the parallel and interdigitated flow fields. Their results showed that the interdigitated flow fields performed much better than the parallel field due to the enhanced mass transport. Besides, the modeling results showed that the lateral current density distribution of the interdigitated flow field was highly non-uniform. The maximal current density occurred at the corners of the land close to the inlet region. Except the maximal current density location, mainly, the current density was decreasing along the channel-land direction, and the current under the outlet channel was significantly lower than that under the inlet channel. Other 2D modeling results [31] and [32] agreed with [30] very well.

He et al. [31] developed a 2D, two-phase model to study the performance of PEM fuel cells with interdigitated flow field. Their results showed that the current density under the land was the highest, and the current density under the inlet channel was much higher than that under the outlet channel. The authors suggested that larger numbers of channel and smaller width of land were better for PEM fuel cells performance.

Liu et al. [32] developed a 2D, two-phase and isothermal model to study the performance of a PEM fuel cell with interdigitated flow field. Their results showed that under lower current density condition, the water content in the outlet channel was higher; and under higher current density condition, the water distributed uniformly. The authors also showed that a decreasing of the outlet channel width could result in an increasing of the performance of the downstream regions, and a more uniform current distribution.

In addition to 2D models, three dimensional (3D) models were also reported. Um and Wang [33] developed a three-dimensional (3D) model to study the mass transport and the electrochemical kinetics in parallel and interdigitated flow fields. Their results elucidated that although the interdigitated flow field outperformed than the parallel flow field regarding to the averaged current density, the current density distribution inside the interdigitated flow field was much more non-uniform. Along the flow channels, both parallel and interdigitated flow field showed the similar current density distribution, which decreased along the channels due to the decreased reactant concentration. However, in the channel-land direction, current density distribution was different for these two plates. For the parallel field, the current density distribution was almost symmetric with the centerline of the land, and the minimal current density occurred under the land. For the interdigitated flow field, the current density in channel-land direction was highly non-uniform. Both the maximal current density and oxygen concentration occurred at the entrance region of the land, and decreased greatly toward the outlet channel. Similar results were also reported by [34] and [35].

Weng et al. [36] used a 3D model to simulate the convection and mass transfer process of a PEM fuel cell with full interdigitated flow field. Their results showed that under high current density operation conditions, non-uniform gas distribution and non-uniform current density was much more severe. The authors also stated that the cell performance non-uniformity and pressure drop was highly dependent on the land width. Proper land width was important for fuel cell performance optimization.

Prasad and Jayanti [37] simulated the flow distribution in PEM fuel cells with interdigitated flow field by a 3D model with systematic consideration of pressure drop

characteristics. Their calculations displayed that lower pressure drop which may be from the larger permeability could result in an increasing of flow non-uniformity. The authors indicated that the dimensions of the channels and the land were essential to the flow distribution in interdigitated flow field.

Chen et al. [38] applied Lattice Boltzman method to study the mass transport in a PEM fuel cell with interdigitated flow field. Non-homogeneous GDL structure was considered. Their numerical results showed that the current density under the inlet channel, the land and the outlet channel was not uniform. The local current density was decreasing along the lateral direction. And the authors also indicated that narrower land was preferred due to the easier water removal.

2.2 Operation conditions

Operation conditions, such as flow rate, back pressure, relative humidity and temperature etc., are essential to PEM fuel cells performance. In this literature review, the effects of flow rate, back pressure and relative humidity are focused, both experimentally and numerically.

2.2.1 Effect of flow rate

Flow rate is directly related to the amount of available reactant, and it is a critical parameter to determine the operation stoichiometric ratio, current density, etc.

Wang and Liu [39] conducted series experiments to study the effects of cathode flow rate on the PEM fuel cells with interdigitated flow field. When the cathode flow rate increased initially, the performance responded quickly; when high enough cathode flow rate was obtained, the performance changed slightly.

Besides the experimental study above, Different models were used to further study the effect of flow rate.

Guvelioglu and Stenger [40] developed a 2D finite element model to investigate the effects of flow rate on the PEM fuel cell performance. The authors showed that under high relative humidity condition, high anode flow rate and low cathode flow rate was preferable for PEM fuel cell performance. High hydrogen flow rate was suggested due to the potential to improve the electro-osmotic drag. Low oxygen flow rate was proposed due to the consideration of water accumulation at cathode side. The authors displayed that the effect of flow rate was interacting with relative humidity.

Ding et al. [41] constructed a 3D, two phase flow PEM fuel cell model. The effect of gas stoichiometric ratios was studied. The authors stated that higher gas stoichiometric ratios could result in higher current density effectively. However, too high gas stoichiometric ratios would not be beneficial to PEM fuel cell performance.

2.2.2 Effect of pressure

It has been widely realized that the gas pressure plays an important role in transporting reactant in PEM fuel cells. Many experimental and numerical works have been published during the past decades.

Boyer et al. [42] numerically studied the effects of operation pressure on the PEM fuel cell performance. They stated that the higher pressure could be helpful to improve the oxygen mass transfer process to the reaction sites, and finally optimize the flow distribution in flow plates. However, higher operation pressure may lead to higher operation cost. When there was sufficient oxygen, increasing operation pressure may not

be able to improve the PEM fuel cell performance. Ideally, in this case, the PEM fuel cell could be operated under atmospheric pressure while retaining high enough efficiency.

Wang and Liu [39] investigated the effects of back pressure on the interdigitated PEM fuel cell both experimentally and numerically. Both anode and cathode back pressure were considered. Their results showed that the open circuit voltage, exchange current density increased with the increasing back pressure. This was due to the increased reactant partial pressure. The modeling results agreed with the experimental data very well.

Al-Baghdadi and Al-Janabi [43] developed a 3D, non-isothermal model of PEM fuel cell with straight flow channels. A comprehensive effect of operation effect on solid mechanics stress, heat transfer and mass transfer were obtained. The authors showed that under higher pressure condition, the local current density distribution was much uniform, and the von Mises stress was much smaller.

Sun et al. [26] experimentally measured the effect of pressure on the local current distribution. In general, the PEM fuel cell performance increased with higher operation pressure. Their results showed that under higher pressure condition, the local current density around the inlet regions was higher than that around the outlet regions. The authors stated that the higher operation pressure mainly affects the inlet regions.

Maddirala and Subramanian [44] applied a numerical technique to obtain the approximated analytical solution of current density and pressure distribution at the cathode side of PEM fuel cells. Laplace's equation was adopted in their model. Their model results showed reasonable comparisons with other numerical solutions.

2.2.3 Effect of relative humidity

Humidification temperature is one of the essential operation parameters to PEM fuel cells, and numerous of researchers have investigated the effect of humidification temperature relative humidity (RH) and on PEM fuel cells performance.

Saleh et al. [45] studied the effects of RH for PEM fuel cells with a serpentine flow field. Two scenarios were investigated. One was the symmetric RH condition, where the RH of the anode and the cathode was equal to each other, while another was asymmetric RH condition, where keeping the RH of one side as 0% and changing other side between dry and fully humidified conditions. The authors concluded that the effect of symmetric RH condition was highly dependent on the fuel cell operation temperature. Under asymmetric RH condition, they concluded that the effect of cathode dry condition was more severe than that of anode dry condition.

Zhang et al. [46] investigated the performance of a PEM fuel cell with a serpentine flow field under dry and fully humidified conditions. Comparing with the PEM fuel cells operated under 100% RH condition, the non-humidified PEM fuel cells displayed lower performance and larger impedance. The authors concluded that it was due to the lower proton transfer ability to catalyst layer under lower RH condition.

Song et al. [47] described the performance of a PEM fuel cell with a serpentine flow field under four different RH conditions. For PEM fuel cells with thin membrane and operated under lower RH conditions, voltage jump from lower to higher value was observed. The authors suggested a possible cause that when the current reached at a critical value, the interface of the membrane and the anode may change to liquid phase, which may improve the anode kinetics and finally improved the performance.

Huang et al. [48] investigated the effect of air RH on the aging of PEM fuel cells. The authors showed that the low air RH could accelerate the aging of the membrane, the catalyst layers and the GDL. During the cycling test, the PEM fuel cell with low RH showed much lower performance.

All of the studies mentioned above [45-48] studied the effect of humidification temperature on the performance of an entire PEM fuel cell, but none were able to differentiate the effects on the local parts of a PEM fuel cell. Yet, due to the widely known non-uniform local current density and water distribution, it is obvious that the local effect of humidification temperature can be non-uniform. Thus, other researchers studied the effects of humidification temperature and RH on the local current distribution in PEM fuel cells [21, 49-52].

Natarajan et al. [49] measured the local current density for a PEM fuel cell with a single flow channel under different hydrogen and air gases humidity conditions. The electrode and the current collector were segmented into six parts. Each part contained both the channels and the land. The authors found that under relatively low air flow rate operation condition, if both cell temperature and anode humidity were increased, the current under those segments near the inlet was increased, while the downstream current was decreased.

Liu et al. [21] applied a sub-cell method to study the effect of lower cathode humidification temperature (CHT) in a PEM fuel cell with a serpentine flow field. Twelve segments were used in this method. When the current was relatively lower, under low CHT condition, the membrane drying phenomenon was much more severe at the segments around inlet. And the performance became better without water flooding along

the flow channel, which was due to the increased accessibility to water along flow channels. When the current was relatively higher, although the membrane under the segments around the inlet was undergoing drying, the membrane around outlet region was experiencing water flooding.

Sun et al. [50] studied the effect of anode and CHT for a PEM fuel cell with a serpentine flow field. Local current were obtained by measuring the current under 21measuring strips. Each strip contained two half flow channels and one land. The authors measured the current for each strip under different combinations of RH conditions. The results showed that when the humidification temperature either at the anode or the cathode side was changed, the current change under 21 strips was not uniform.

Aboubakr et al. [51] measured the temperature and current distribution along a single channel of a PEM fuel cell with different gas RH. The air and hydrogen gases RH were changed symmetrically. The results showed that the temperature became more uniform when the RH was higher, which mainly was due to the cooling effect of water. The results also showed that more uniform current density could be obtained when the RH was increased.

Reshetenko et al. [52] studied the effect of gas humidity for a PEM fuel cell with a multi-serpentine flow field. The anode was divided into ten parts, and each of which contained several turns of channels and lands. The results showed that when the cathode RH was decreased, the activation and ohmic loss was increased, which was due to the dehydration of the membrane and catalyst layer. The electrochemical impedance results showed that the cathode charge transfer resistance was increased when the cathode RH

was decreased, especially at the low current density regions. Besides, the authors also stated that the change of RH could result in a non-homogeneous current change.

2.3 Local impendence and electrochemical area

From previous literature review, significant current density variation occurs inside PEM fuel cells. The variation can be influenced by many factors, such as operation conditions, flow plate hardware, edge effect, etc. [53]. So it is worthwhile to measure the internal electrochemical characteristics.

Brett et al. [53] measured the local impendence of a PEM duel cell along a single flow channel. In order to measure the local impendence, specialized cell configuration was designed. The length of the single flow channel was 110 mm, and it was separated into 10 segments. The current under each segment was collected individually, and there was no current flow cross any two of the segments. The frequency range applied was 10 KHz to 0.1 Hz. Two cell operation voltages were applied, i.e. 0.8 V and 0.6 V. At the cell voltage 0.8 V, the arc radius was increasing along the flow channel. Since the reactant concentration was decreasing along the flow channel, the authors proposed that the limitation of mass transport could lead to the increasing of arc radius along the flow channel. At the cell voltage 0.6 V, the arcs under the inlet parts showed similar trend as that at the 0.8 V. However, the outlet parts underwent reactant starvations, and the arc directions were reversed in this situation.

Schneider et al. [54] experimentally obtained the local cyclic voltammograms of a PEM fuel cell with single flow field. The flow field was divided into 9 segments along the flow channel. The experimental results showed significant difference of the cyclic voltammograms along the flow channel when inert gas was supplied. The authors

demonstrated that the non-uniformity came from the decreasing of the local cathodic hydrogen reduction currents along the flow channel.

Higier and Liu [55] measured the electrical resistance under the channel and the land. They showed that the total electrical resistance under the land was much lower than that under the channel for the flow field with wider channel (Channel width $\geq$ 2 mm). This could lead to the huge performance difference between that under the land and the channel. However, for narrower channel (Channel width $\leq$1mm), the total electrical resistance under the channel and land were close to each other. Higher and Liu [29] also studied the electrochemical areas (ECA) difference under the land and channel. Due to the larger compression under the land, the ECA under the land was higher than that under the channel, which could result in a better performance under the land.

2.4 Channel and land width

The geometric parameters of PEM fuel cells play an important role in determining the performance by affecting the gas diffusion, electricity resistance and other electrochemical properties. Many researchers have conducted both experimental and modeling work in order to achieve the optimization designs.

Yoon et al. [56] experimentally studied the effects of channel and land width. The channel width was kept as 1mm, while various land widths were adopted. The authors suggest that PEM fuel cells with narrower land were desirable.

Hsieh and Chu [57] conducted series experiments to investigate the effect of channel to land width ratio. The authors found that when considering the fuel cell performance only, the optimal ratio approached unity. With the consideration of pressure drop addition, the optimal ratio switched to about 0.67.

Goebel [58] investigated the impact of land and channel width experimentally. The author found that in the high current density region, the land width was the most important factor to fuel cell performance. Narrower land width was preferable. The author also showed that in order to prevent high electrical resistance, the land area fraction should be approaching about 50%.

Sun et al. [59] applied a 2D model to study the channel-land width ratio of PEM fuel cells. Their results showed that larger channel-land width ratio was preferable for PEM fuel cells. However, too narrower land may lead to reduction of electrical conductivity. A trade-off channel-land width ratio should be considered.

Shimpalee and Zee [60] investigated the effect of channel and land geometry on the PEM fuel cell with serpentine flow field numerically. Both stationary and automotive operation conditions were considered. Under stationary conditions, the authors stated that wider land was better for heat transfer. And narrower land could lead to non-uniform current distribution. However, the results were reversed when automotive operation conditions were considered. When the channel/land width increased, the fuel cell performance was improved.

Pend et al. [61] used the design of experiments method and an annealing optimization method to obtain the optimal critical geometric dimensions of graphite plate. Considering the performance and manufacture, the author showed the optimized values for channel depth, channel width, land width and chamfer radius are 0.5, 1.0, 1.6 and 0.5mm.

Wang et al. [62] developed a 3D, two-phase model to study the PEM fuel cell mechanism. Single and triple serpentine flow fields were considered in their study. For

both flow field, in the higher cell voltage regions (cell voltage > 0.7 V), the channel aspect ratio (channel width/channel height) was not important to PEM fuel cell performance. However, in lower cell voltage regions, the performance would be improved with smaller channel aspect ratios.

Manso et al. [63] studied the effect of channel aspect ratio on the PEM fuel cell with serpentine flow field numerically. The current density, velocity and temperature distribution inside the PEM fuel cell under different channel aspect ratio were studied. The authors showed that under low channel aspect ratio, current density, velocity and temperature distribution were less uniform that under the higher channel aspect ratio.

Lu et al. [64] researched the effect of channel-land width ratio and channel alignment on the PEM fuel cell performance by modeling method. For the well aligned channels, the channel-land width ratio affected the in-plane stress distribution not obviously. For the alternation gas channels, the in-plane stress could be changed due to different channel-land width ratios.

2.5 Novel flow field designs

Three types of the most common used flow plates are parallel, serpentine and interdigitated flow plates, which have been introduced in Chapter 1. In recent years, a lot of novel flow field designs have been proposed by numerous researchers.

Tüber et al. [65] designed a new flow distribution plate as shown in Fig. 2.1. The fractal structures were developed by the 'FracTherm' algorithm. Comparing with parallel and fractal plates, the latter one required less energy input due to the smaller pressure drop. When only one phase was considered, the fractal structure could improve the cell performance.

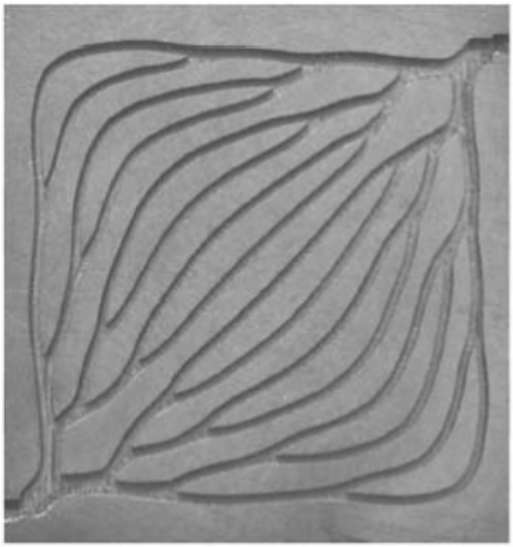

Fig. 2.1 Designs of flow plates with fractal structures [65]

In order to force more reactant into the reaction sites in the catalyst layer, Liu et al. [66] numerically designed baffle-blocked flow channels as shown in Fig. 2.2. Their numerical results showed that the baffles had positive effect on the mass transport and cell performance. Prediction showed that at the higher operating voltages, the baffle effect could be ignored, while at the lower operating voltages, the baffle effect was significant, especially on the local current density under the baffles. Thitakamol et al. [67] designed a similar mid-baffled plate later. Their experimental results showed that comparing with the conventional interdigitated flow field, the cell performance was increased about 1.2 to 1.3 times. It should be noticed that the locations of the baffles had not been considered in [66] and [67]. Furthermore, Jang et al. [68] optimized the baffles locations by conjugate-gradient method (SCGM). The optimized cell performance was increased by 14%.

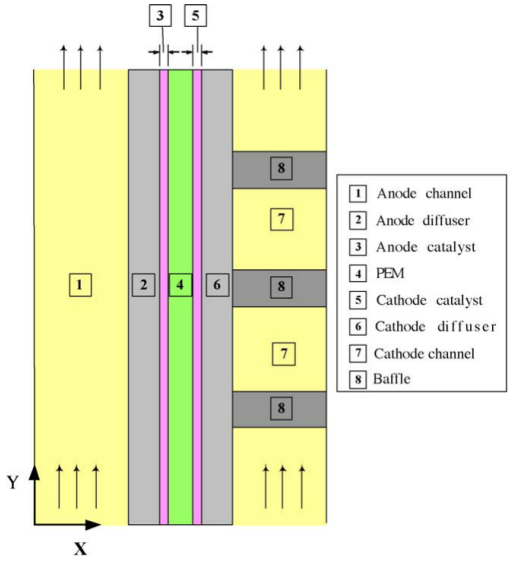

Fig. 2.2 Designs of baffle-blocked flow channels [66]

Sun et al. [69] used a 3D, single phase model to aid the design of a serpentine channel with a trapezoidal cross-sectional shape as shown in Fig. 2.3. The authors denoted a dimensionless channel shape ratio R as the ratio of B to A. Different channel shape ratio R could lead to different pressure distribution. Their results showed that the larger value R was preferable.

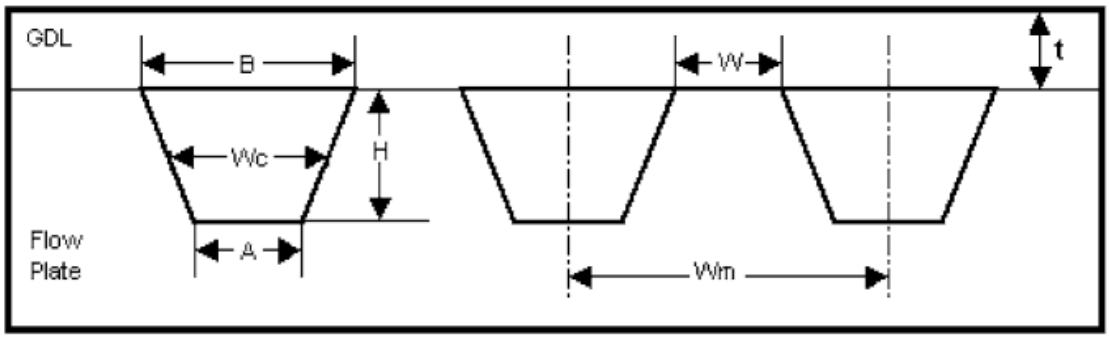

Fig. 2.3 Designs of trapezoidal cross-sectional channel [69]

Chiang et al. [70] applied a 3D model to investigate the performance improvement of the novel flow channel shown as in Fig. 2.4. The predictions showed that the optimal land/channel ratios were dependent on the cell operating conditions. In the most practical operation conditions, the current density under the land was higher than that under the channel. So the larger land/channel ratios at the outlet regions were preferable. However, in the higher current density regions, the effect of this configuration was small. The authors suggested that a divergent configuration with optimal lower land/channel ratios 0.67 was beneficial to cell performance when the cell voltage was 0.22 V.

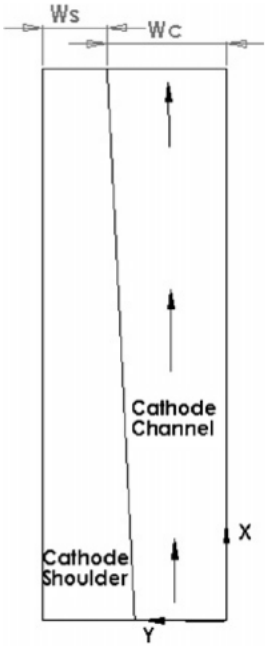

Fig. 2.4 Designs of flow channel with various land/channel ratios [70]

Comparing with the conventional serpentine flow field, Xu and Zhao [71] designed a convection-enhanced serpentine flow field (CESFF) shown as in Fig. 2.5. By both

numerical and experimental results, they found that the pressure drop between two adjacent channels were increased comparing with the conventional serpentine flow field. Thus, the convection was enhanced, and the mass transport was much easier and efficient. In addition, the high convection could be helpful to remove the liquid water droplet inside the cathode catalyst layer.

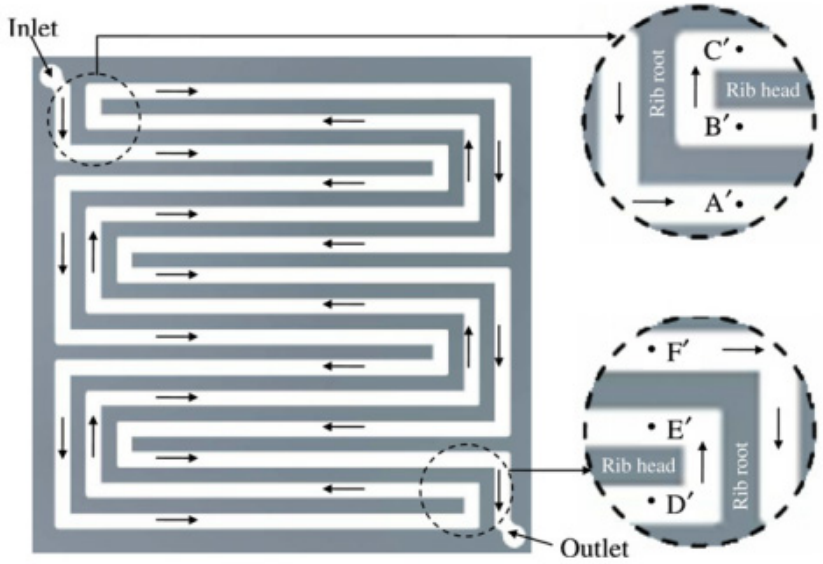

Fig. 2.5 Designs of convection-enhanced serpentine flow field (CESFF) [71]

Kuo et al. [72] developed a 3D model to study a newly designed wave-like flow field as shown in Fig. 2.6. The modeling results showed that the wave-like channel could improve the mass transport to the catalyst layer and the heat transfer rate. The performance of the wave-like flow field was much higher than the conventional fields.

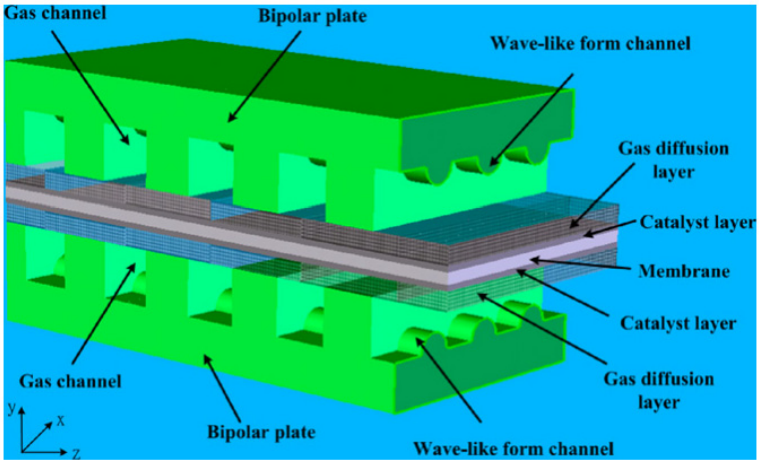

Fig. 2.6 Designs of wave-like flow field [72]

Yan et al.[73] modified the outlet channels of conventional serpentine flow channels as shown in Fig. 2.7. A 3D model was used to study the effect of the contracted outlet channels. Their numerical results showed that due to the contracted outlet channels, the reactant velocity, the mass transport and water removal was improved. Thus, the cell performance was enhanced comparing with the conventional serpentine flow channels. The authors also found that both the optimal height contraction ratio and length contraction ratio was 0.4 for their model.

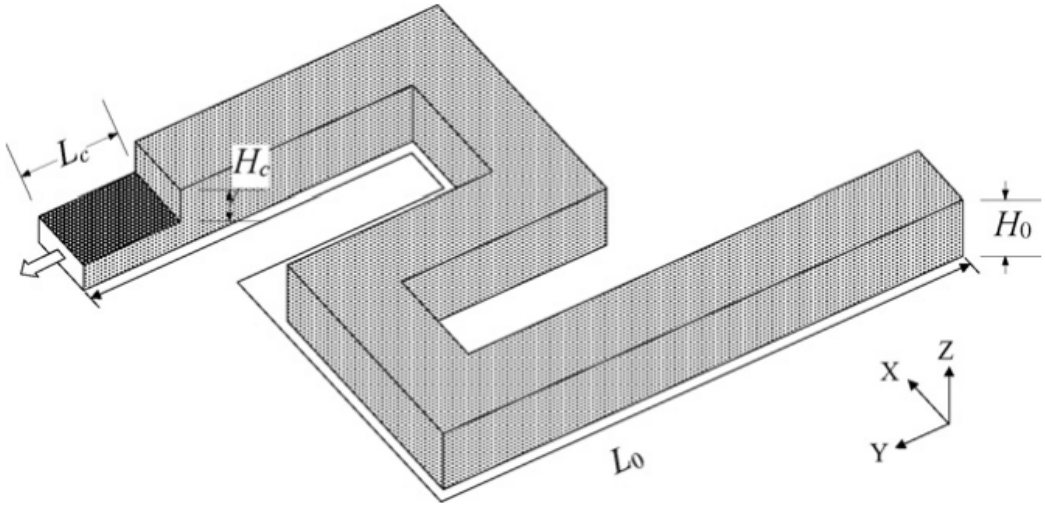

Fig. 2.7 Designs of contracted outlet channel [73]

Kloess et al. [74] was inspired by the bio-systems in nature. They designed two novel bio-inspired flow patterns as shown in Fig. 2.8. Both their numerical and experimental results showed that the bio-inspired flow patterns could provide higher cell performance than serpentine or interdigitated could. Their numerical predictions showed that the pressure drop was lower than the conventional serpentine or interdigitated flow fields. Besides, the flow distribution of these bio-inspired flow plates was much uniform. The experimental studies prove that the by adopting these novel flow plates, the maximum power density is enhanced up to 30%.

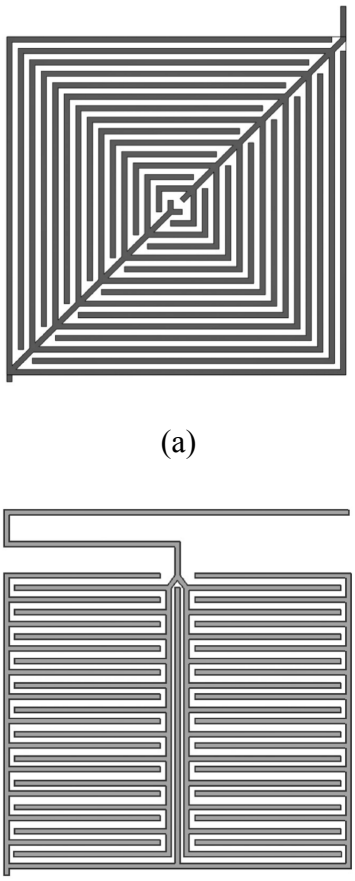

(a)

(b)

Fig. 2.8 Designs of new flow patterns. (a) leaf pattern; (b) lung pattern [74]

Similarly, Roshandel et al [75] numerically developed a new flow field as shown in Fig. 2.9. Their modeling results showed that the power density of this newly designed flow field was 56% higher than that of the parallel flow field, and 26% higher than that of the interdigitated flow field. Both [74] and [75] provided different vision to flow field designs.

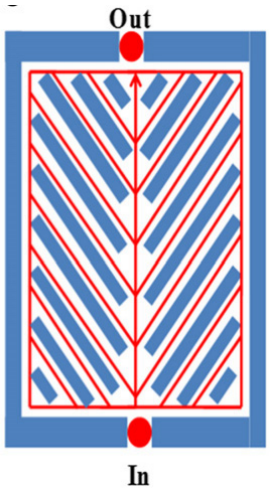

Fig. 2.9 Designs of bio-inspired flow field [75]

Min [76] proposed a stepped flow field with the aim of improving the gas diffusion as shown in Fig. 2.10. The author suggested that the smaller the channel height, the higher the performance.

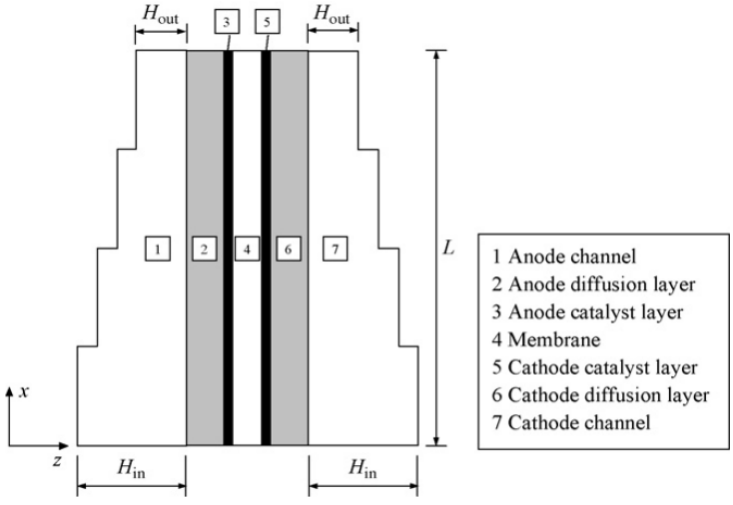

Fig. 2.10 Designs of a stepped flow field [76]

If expand the steps of the stepped flow field shown in Fig. 2.10 to infinity, a tapered flow channel could be obtained. Wang et al. [77] numerically designed a tapered plate as shown in Fig. 2.11. In their work, channels 2-4 were height-varying channels, and channel 5 was a diverging channel. They explained that the channels with varying height could improve the under land convection, and thus enhanced the local current density, while the diverging outlet channel could prevent any possible gas leakage. Their results showed that comparing with conventional channels, this newly designed channels could improve the performance about 11.9%.

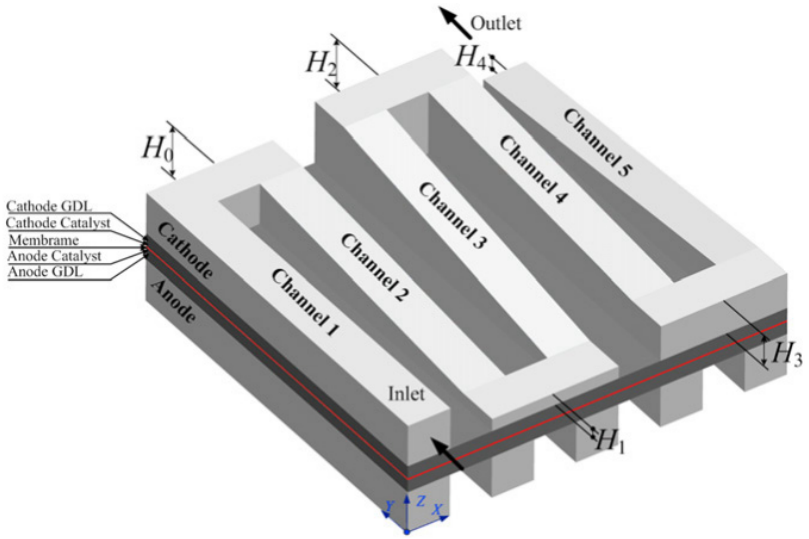

Fig. 2.11 Designs of serpentine flow channel with varying channel heights [77]

CHAPTER 3

OBJECTIVE OF STUDY

As can be seen from the literature review in Chapter 2, numerous of work has been done regarding with the current distribution in PEM fuel cells with either parallel or serpentine flow fields. And all of the previous work measured either the current under the channels and the lands together or the current under two channels together. However, only model work showed that the current distribution for interdigitated flow field is not uniform, and there are few systematic studies of the lateral current density variation for interdigitated flow field.

Interdigitated flow field is also one of the most commonly used flow fields in PEM fuel cells and the knowledge of lateral current density variation is critical for flow field design optimizations. Thus, the main objective of this study is to provide guidance for PEM fuel cells optimization designs. In order to fulfill this objective, series experiments are conducted to measure the current distribution in an interdigitated flow field. The first aspect deals with the direct measurements of the current under the inlet channel, the land and the outlet channel of PEM fuel cells with a single interdigitated flow field. In addition, the effects of cathode flow rate, cathode humidification temperature and cathode back pressure on the local current density are studied. Furthermore, few literatures discussed the current density distribution in the lateral direction with smaller scale. In this study, higher resolution lateral current density distribution in a single interdigitated flow field is measured. Partially-catalyzed membrane electrolyte assembly (MEA) method is adopted to measure the local current density. The local cyclic

voltammetry and electrochemical impedance spectroscopy (EIS) tests are used to study the current distribution phenomenon.

Besides, a two-dimensional model is developed to research the underlying mechanism of the PEM fuel cells with interdigitated flow field. From literature review, the effect of lateral ECA distribution is not considered in previous model work. In this study, the lateral ECA distribution is integrated into the model, and this makes the model much closer to the real situations. First, the lateral current distribution will be studied. Finally, optimizations of geometric dimensions will be studied.

Overall, experimental and numerical studies together can explore PEM fuel cells mechanisms, and thus, furnish the future PEM fuel cell optimization designs with worthy guidance.

CHAPTER 4

EXPERIMENTAL METHODOLOGY

4.1 Experimental system

The PEM fuel cells experimental system is shown as Fig. 4.1. Hydrogenics Test Systems® FCATS-G60 station from GREENLIGHT Company is used to control the gas flow rates, gas inlet temperatures, cell temperature and the back pressure. Cell voltage and current are recorded by VersaSTAT 3® station from AMETEK Company. The reactants enter the fuel cell flow fields through the humidifier and the flow-rates are maintained by the flow controllers at pre-determined values. Nitrogen gas is used to purge both the anode and cathode flow fields after each experiment. The back pressure regulators are used to adjust the cell's operating pressure.

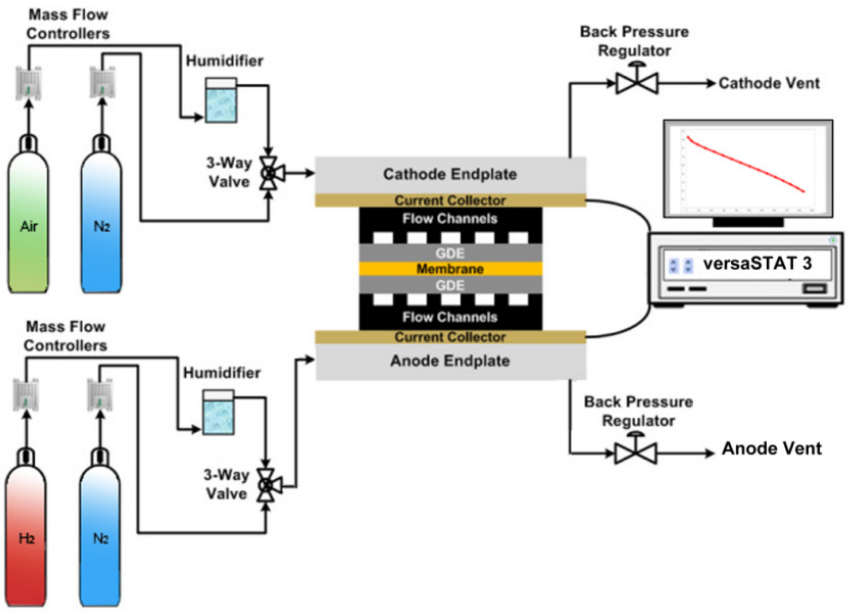

Fig. 4.1 Schematic of PEM fuel cells test system

4.2 Methodology of direct measurements of current

The partially-catalyzed membrane electrode assemblies (MEA) are fabricated in-house using commercial proton exchange membranes and gas diffusion electrodes (GDEs) by the hot-press technique. The proton exchange membrane used is Nafion® 117 from Alfa Aesar Company and the gas diffusion layer (GDL) used is the ELAT^{TM} carbon cloth from FuelCellsEtc Company. The platinum catalyst loading is $0.4\ \mathrm{mg \cdot cm^{-2}}$. A flow plate with an interdigitated flow field is used at the cathode side. The flow field consists of one inlet channel, one land and one outlet channel. The schematic of cathode flow plate is shown in Fig. 4.2. The anode flow plate has a single serpentine flow field with rectangular cross section channels. The dimension of anode channel is 1mm in depth, 1 mm in width and 7.1 mm in length. The anode is assembled with a full size MEA with an area of $50\ \mathrm{cm^2}$, and the channel orientation is perpendicular to the channels on the cathode side to eliminate any potential effects from anode side. In order to measure the currents under the inlet channel, the land and the outlet channel separately, three different fuel cells are assembled, each with one of the three partially-catalyzed cathode MEAs as shown in Fig. 4.3. For example, to measure the current density under the inlet channel, only the area under the inlet channel is catalyzed, while the areas under the land and under the outlet channel are catalyst free as shown in Fig. 4.3 (a). Thus all the current measured during the experiments with such an MEA must be generated in the area under the inlet channel. Similarly, currents in the area under the land and in the area under the outlet channel can be separately measured.

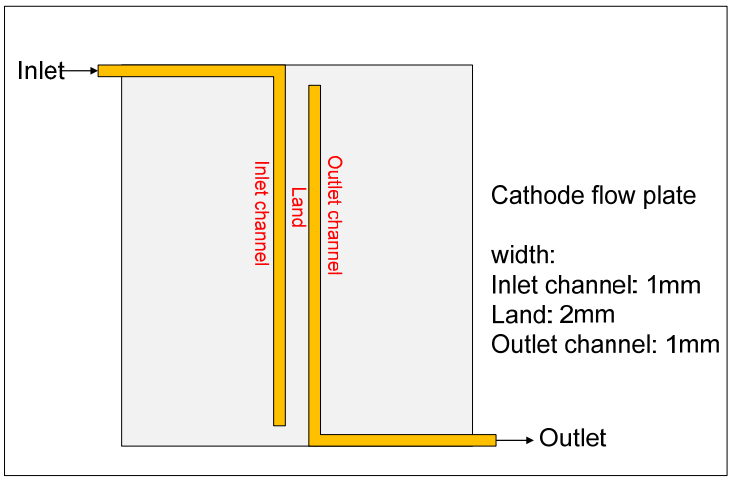

Fig. 4.2 Schematic of cathode flow field

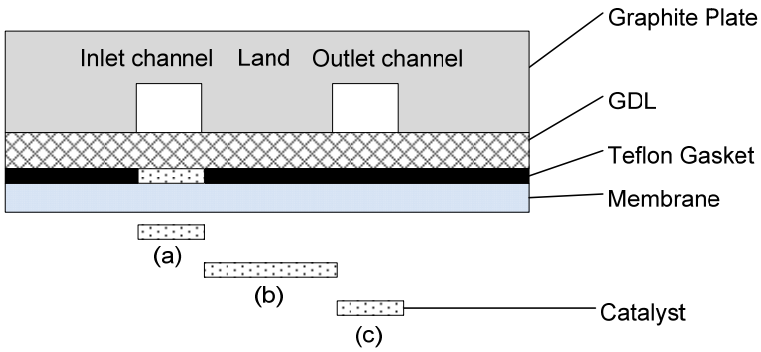

Fig. 4.3 Schematic of partially-catalyzed MEA at the cathode side: (a) MEA catalyzed under the inlet channel only; (b) MEA catalyzed under the land only; (c) MEA catalyzed under the outlet channel only

Before the measurement, break in process is highly recommended for any newly assembled fuel cells. In this dissertation, break in process consists of two steps, which are saturation step and potentiostat break in step with constant voltage 0.5V. Three polarization curves are measured after steady state been obtained. The final results are the averaged polarization curves.

4.3 Methodology of lateral current distribution measurements

The membrane electrode assembly (MEA) is made in house. The Nafion® 117 membrane from Alfa Aesar Company is used. The gas diffusion electrode (GDE) is ELAT™ carbon cloth from FuelCellsEtc Company. The catalyst loading at both anode and cathode is $0.4\ \mathrm{mg \cdot cm^{-2}}$. A full serpentine flow field is used as anode flow plate. The cross-sectional area of the flow channel is 1mm × 1mm. The land width is 1 mm. An interdigitated flow field with one inlet channel, one land and one outlet channel is used as cathode flow plate. The schematic of the cathode flow field is shown as in Fig. 4.2. The widths of the inlet channel, the land and the outlet channel are 1mm, 2mm and 1 mm. The anode catalyst loading area is $50\ \mathrm{cm^2}$, however, the cathode is partial catalyzed as shown in Fig. 4.4. The current densities under seven different lateral locations (P1-P7) are measured separately. Each time, catalyst is loaded under just one location while keeping other locations catalyst free. Finally, one memrane, two GDEs, two flow plates, two Teflon® gaskets, two current collectors and two end plates are assembled with $6.2\ \mathrm{N \cdot m}$ torque.

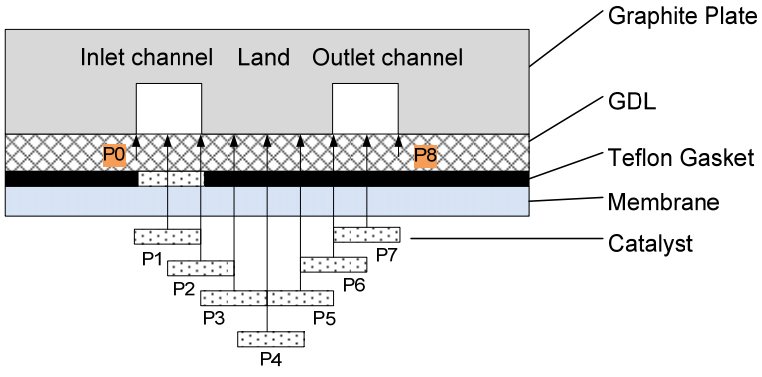

Fig. 4.4 Schematic of cathode partial MEA under different locations

4.4 Fuel cell characterization methodology

4.4.1 Polarization curve

The polarization curves are widely used to show the PEM fuel cells performance. During the experiments, the voltage is swept from 1 V to 0.2 V with a decrement of 0.01 V/s, and the current is measured after steady state obtained at each voltage. In this dissertation, for each case, three polarization curves are obtained and averaged finally.

4.4.2 Cyclic voltammetry

Cyclic voltammetry (CV) technique is applied to characterize PEM fuel cells electrochemical areas (ECA) [13]. In a typical CV test, the cell voltage is swept back and forth between two limiting voltages and the responding current is recorded. The plot of current versus potential is called cyclic voltammogram [5].

In this dissertation, CV test is carried out on a PEM fuel cell with hydrogen as anode gas and nitrogen as cathode gas. CV test is conducted by four-electrode configuration. Reference electrode and counter electrode are used at anode side, while working electrode and working sense are used at cathode side. The working electrode is applied to collect current at cathode side, and the counter electrode at anode side could provide a complete current path. The working sense and reference electrode could be used to control the cell voltage during the CV test. The cell voltage is swept between 0 V and 1 V. Voltage sweep rates are 0.10 and 0.15 V/s. Each CV test is repeated three times and finally averaged.

A sample of cyclic voltammogram is shown as in Fig. 4.5. The hydrogen desorption and adsorption processes are also shown in Fig. 4.5. When the voltage is swept forward

and past a critical voltage value, the active electrochemical reaction would be increased and the responding current would also be increased to a peak. This process is called hydrogen desorption. When the voltage is swept backward, the reversed current direction could be obtained, which is the cause of hydrogen adsorption [5, 13]. The adsorption and desorption process are reversible to each other as followings [29]:

$$\text{Desorption process: } Pt - H_{ads} \rightarrow Pt + H^+ + e^- \quad (4.1)$$

$$\text{Adsorption process: } Pt + H^+ + e^- \rightarrow Pt - H_{ads} \quad (4.2)$$

Where Pt denotes a proton adsorption site at the platinum surface, $Pt - H_{ads}$ denotes a chemisorbed proton to the platinum surface. Considering the reversibility, the protons adsorption and desorption charges should be equal in ideal condition. However, the amount of adsorption charge may differ from that of desorption charge [78]. There is no specific standard to choose which one to calculate ECA [78]. Some researchers used proton adsorption charge [79-81], while others used proton desorption charge [13, 29, 82, 83], or the averaged value of adsorption and desorption charge [84-86]. In this dissertation, proton desorption charge is used to characterize ECA due to the integrating limitations of the software.

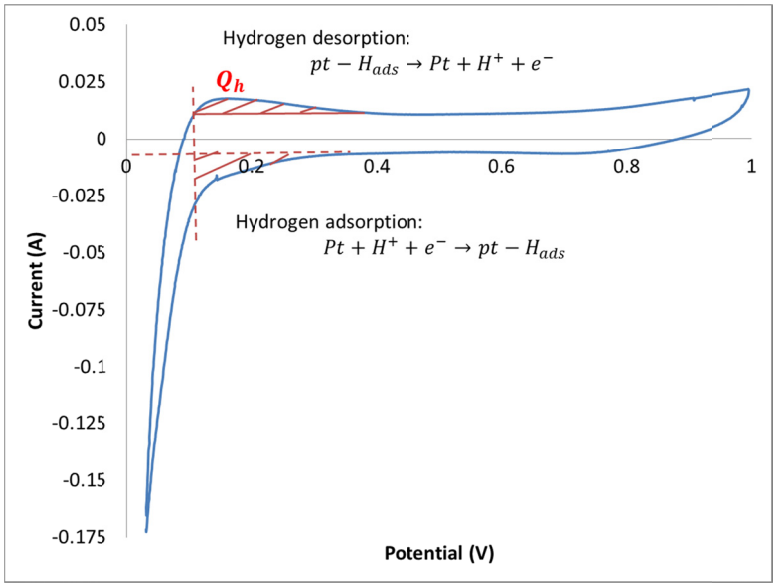

Fig. 4.5 Sample of Cyclic voltammogram: cell temperature=70℃, both anode and cathode are fully humidified; hydrogen flow rate=500 sccm, nitrogen flow rate=500 sccm; voltage scan rate=0.10V/s; ambient pressure at both anode and cathode sides.

The ECA (cm^2/mg) can be calculated based on the the hydrogen desorption charge as followings [13]:

$$ECA = \frac{Q_H}{0.21 \times [Pt]} \tag{4.3}$$

$$Q_H = \frac{Q_h}{A} \tag{4.4}$$

Where Q_h (mC)is the total hydrogen desorption charge on the electrode, A (cm^2) is the nominal electrode area, Q_H (mC/cm^2)is the hydrogen desorption charge on the electrode per unit area, 0.21 (mC/cm^2) is the hydrogen desorption charge per unit area based on a smooth platinum surface [5], [Pt] (mg/cm^2) is platinum catalyst loading per unit area.

4.4.3 Electrochemical impedance spectroscopy

Electrochemical impedance spectroscopy (EIS) is widely accepted as a method to measure the individual impedance of PEM fuel cells components, and it can be used to distinguish the ohmic resistance, charge transfer resistance and double layer resistance [13, 87]. A typical EIS is shown in Fig. 4.6.

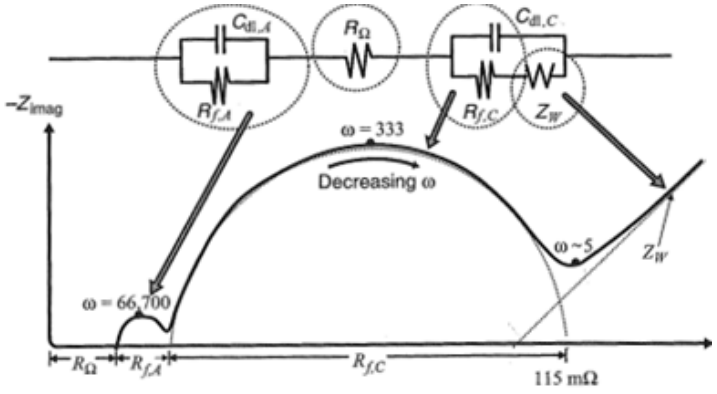

Fig. 4.6 A sample of typical EIS [5]

In this dissertation, the EIS test is conducted under different density conditions. The AC current interruption is 5% of the fuel cell DC current, and the interruption frequencies are between 10 KHz and 0.5 Hz with 10 points per decade.

CHAPTER 5

DIRECT MEASUREMENTS OF CURRENT UNDER THE CHANNELS AND THE LAND

5.1 Current under the channels and the land

Fig. 5.1 shows a sample of direct measurement results of current densities under the areas of the inlet channel, the land and the outlet channel. The fuel cell operating temperature is 70 °C, the back pressure is ambient, the flow rates for both hydrogen in the anode and air in the cathode are 500 sccm, and both the anode and cathode gases are fully humidified. The current density under the land area is higher than those under both the inlet and outlet channels. The current densities difference between the inlet channel and the land is similar to the difference between the channel and land observed in both parallel channel flow field [1] and in serpentine flow filed [2]. In the activation loss and ohmic loss dominant regions, the current density under the land is higher than that under the inlet channel. This is due to the higher electrochemical areas (ECA) [29] and lower electric resistance [55] under the land. However, in concentration loss dominant region, the current density under the inlet channel becomes higher than that under the land, indicating a high concentration loss under the land. This result is in contradiction to intuition: convection mass transfer under the land in an interdigitated flow field should lead a lower concentration loss. The fact is that the concentration loss under the land is indeed lower compared with both parallel and serpentine flow fields [1]. The reason for the difference is that the inlet land area has an even lower concentration loss due to the "impinging type" of convection mass transfer as shown in Fig. 5.2. In the inlet channel,

the gas is forced to flow down toward the catalyst layer and then through the GDL under the land area. The velocity vector forms an acute angle (<90°) with the mass flux vector, thus the local mass transfer is significantly enhanced. While under the land area, the velocity vector is approximately parallel to the mass flux vector. Besides, a minor contribution may come from the lower effective porosity under the land due to the direct compression of the land structure.

The most striking difference in current density is observed between the inlet and outlet channels. The current density under the outlet channel is markedly lower than that under the inlet channel. The most obvious reason for such a large difference is the difference in the angles formed by the velocity vector and the mass flux vector. Under the inlet channel, the gas flows into the GDL, thus the velocity vector forms an acute angle (<90°) with the mass flux vector, while under the outlet channel, the gas flows out from the GDL, thus the velocity vector forms an obtuse angle (>90°) with the mass flux vector. While the mass transfer under the inlet channel is enhanced, the mass transfer under the outlet channel is hindered, leading to a significant difference in local current densities. Note that in this study, when measuring the current density under the outlet channel, there is no catalyst in the region under the inlet channel and under the land, thus there is no effect due to average concentration reduction, i.e. the lower current density under the outlet channel is not caused by the reduction of oxygen concentration due to up-stream reactions. In a real-life fuel cell with an interdigitated flow field, the average oxygen concentration in the outlet channel will be lower than that in the inlet channel due to up-stream consumptions. Thus, the observed very large difference in current density between

the outlet channel and inlet channel is actually conservative – in a real fuel cell the difference will be greater.

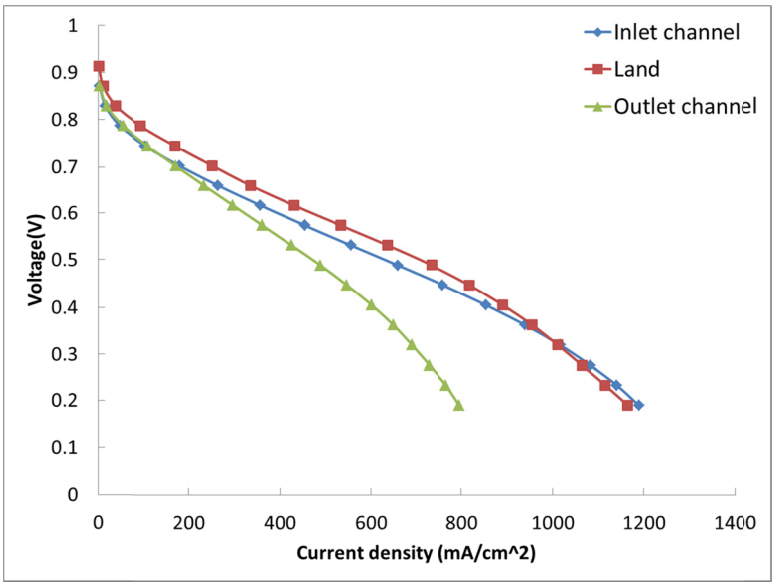

Fig. 5.1 Polarization curves comparisons under the channels and the land: cell temperature=70℃, anode and cathode are fully humidified; hydrogen flow rate=500 sccm, air flow rate=500 sccm; ambient pressure at both anode and cathode sides

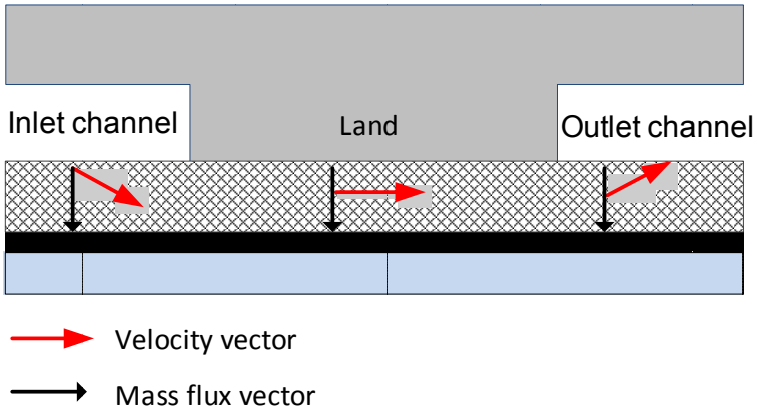

Fig. 5.2 Schematic of the angels between the velocity vector and the mass flux vector under the two channels and the land

5.2 Different cathode flow rates

As shown in Figure Fig. 5.1, the local current densities in different areas of a PEM fuel cell with an Interdigitated flow field are very different. In order to determine if such a pattern of local current density differences is a particular case or general to a wide operating conditions, comparisons are made at three different cathode flow rates. The polarization curves under the two channels and the land at three cathode flow rates are shown in Fig. 5.3. It can be clearly seen that the same pattern of local current density differences exists for all the three operating conditions. The results show that at all the three areas, the current densities are higher at higher cathode flow rate. In order to further examine the results, Fig. 5.4 is produced, where current densities at the inlet channel, the land and the outlet channel at different cell voltages are compared. All the current densities are normalized by the current density under the inlet channel. With such a detailed comparison, the same pattern is still clearly seen for all the three cases with different cathode flow rates. First, in the typical cell operating voltage range of 0.5 – 0.7 V, current densities under the land are always higher than those under the two channels. At 0.7 V the current densities under the land are about 40% higher than that under the inlet channel, while those under the outlet channel are only about 80% of those under the inlet channel. At 0.6V, differences between the land and the inlet channel become smaller, with the current density under the land being about 20% higher; while the differences between the inlet channel and the outlet channel become greater, with the current density under the outlet channel being only about 60% of those under the inlet channel. It is interesting to note that at about 0.4 V, the current densities under the inlet channel and the land become practically the same. When the cell voltage is lower than 0.4V, the current

densities under land are lower than those under the inlet channel. It is clearly seen that the current densities under the outlet channel are always the lowest among the three different locations. The detailed data used in Fig. 5.4 are also provided inTable 5.1.

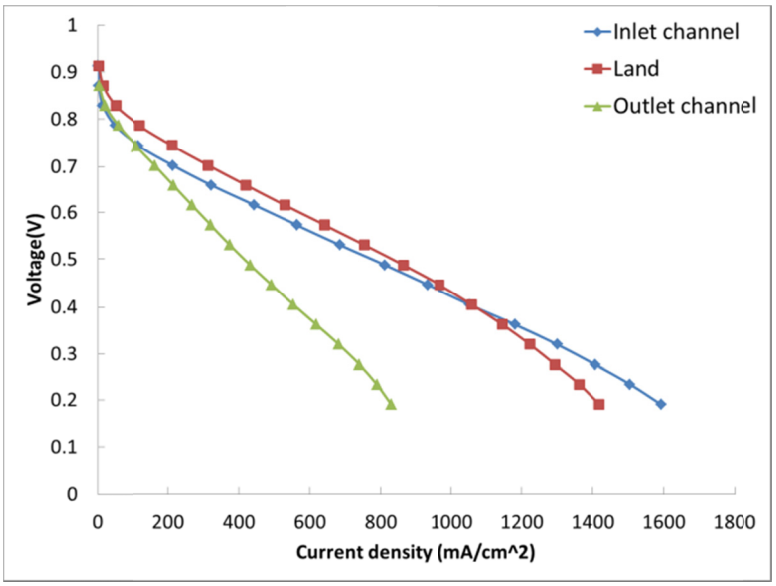

(a)

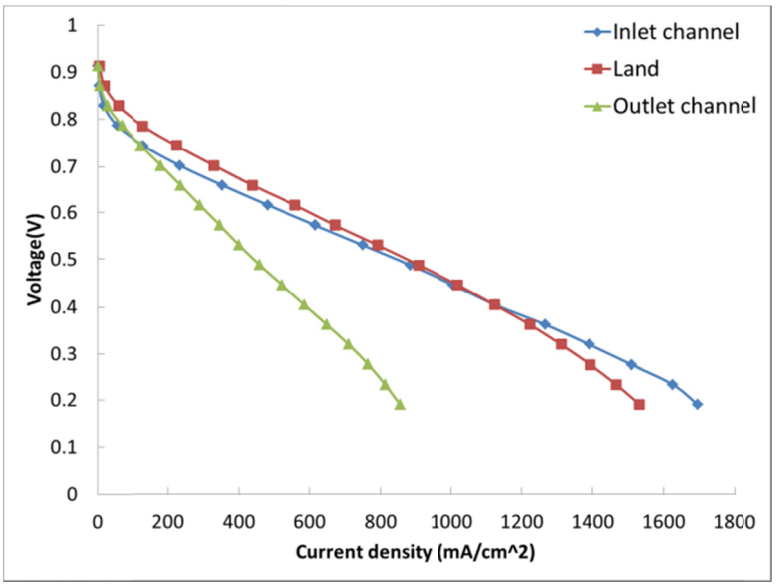

(b)

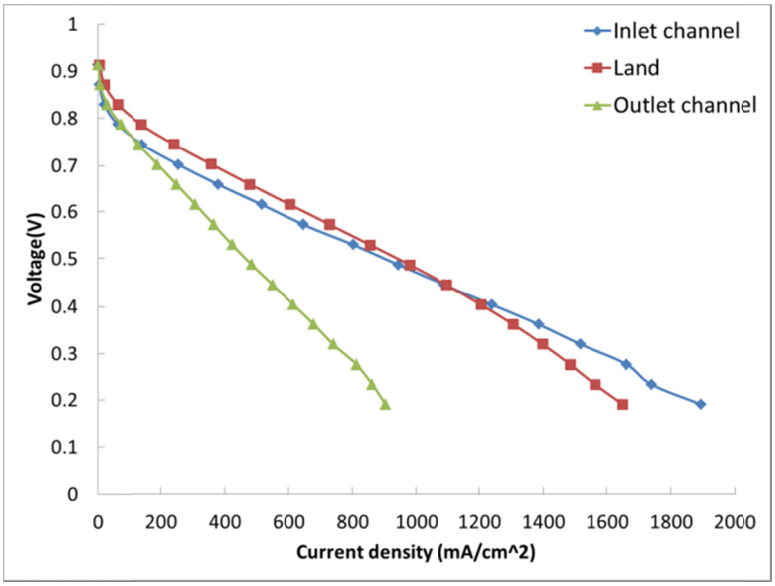

(c)

Fig. 5.3 Polarization curves under different cathode flow rates: anode and cathode are fully humidified, cell temperature=70°C; hydrogen flow rate=1000 sccm; ambient pressure at both anode and cathode sides. (a) Air flow rate=500 sccm; (b) air flow rate=1000 sccm; (c) air flow rate=1500 sccm

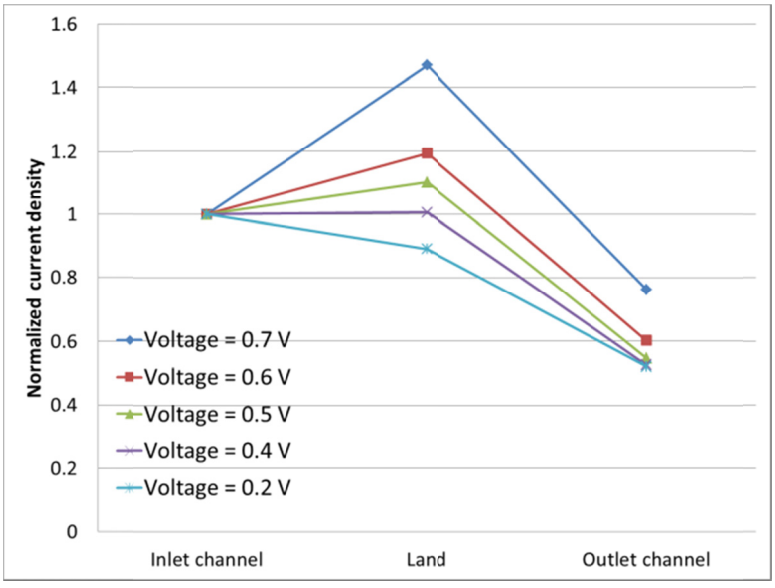

(a)

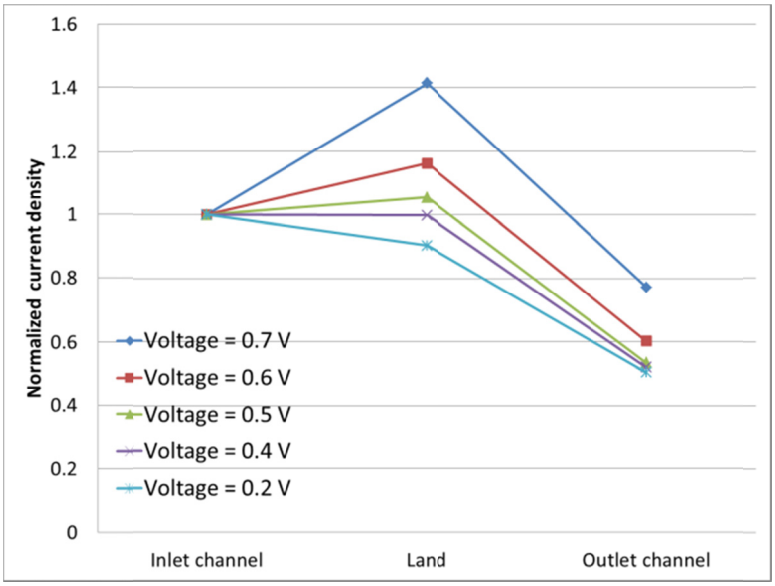

(b)

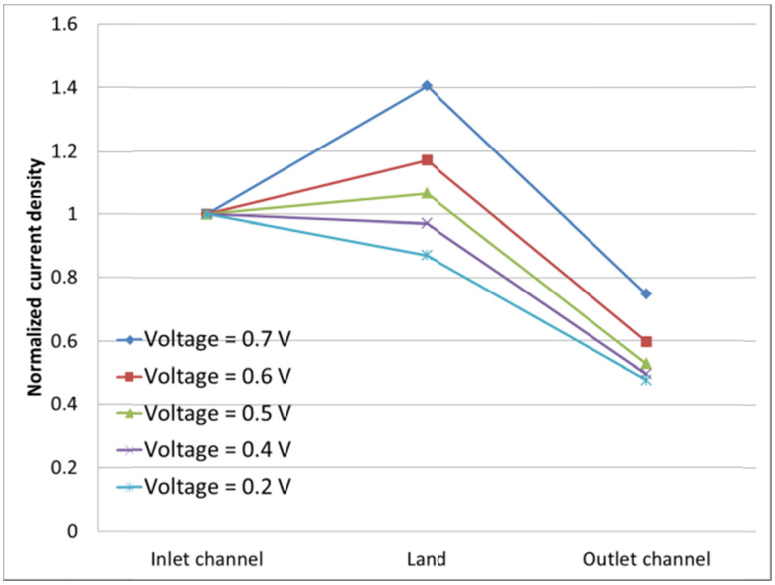

(c)

Fig. 5.4 Normalized current densities at different cathode flow rates: anode and cathode are fully humidified, cell temperature=70℃ ; hydrogen flow rate=1000 sccm; ambient pressure at both anode and cathode sides. (a) Air flow rate=500 sccm; (b) air flow rate=1000 sccm; (c) air flow rate=1500 sccm

Table 5.1 Current densities (mA/cm^2) under different cathode flow rates at certain cell voltages

Cathode flow rates (sccm)	Cell voltages (V)	Inlet channel (mA/cm^2)	Land (mA/cm^2)	Outlet channel (mA/cm^2)
500	0.7	213.16	313.55	162.63
	0.6	443.38	529.05	267.07
	0.5	684.72	753.96	374.73
	0.4	1052.39	1059.38	553.76
	0.2	1592.25	1418.09	828.93
1000	0.7	232.84	329.33	180.01
	0.6	481.34	559.01	289.84
	0.5	750.15	791.66	400.13
	0.4	1124.53	1122.68	584.75
	0.2	1695.57	1532.24	853.63
1500	0.7	254.57	358.05	190.28
	0.6	515.65	603.54	308.04
	0.5	802.87	855.44	423.33
	0.4	1241.14	1205.89	615.10
	0.2	1894.17	1649.46	903.21

5.3 Different cathode back pressures

Fig. 5.5 shows a sample of the current densities comparisons under the channels and the land at three cathode back pressures. In order to further elucidate the experimental data, Fig. 5.6 is produced. Comparing with Fig. 5.4, it shows that the cathode back pressure has negligible effect on the lateral current densities distribution pattern. Similar to Fig. 5.4, in this study, current density under the land is higher than that under the inlet

channel in the high cell voltage region (>0.4V) and lower in the low cell voltage region (<0.4V). At all typical cell voltages, the current density under the outlet channel is smaller than that under the inlet channel.

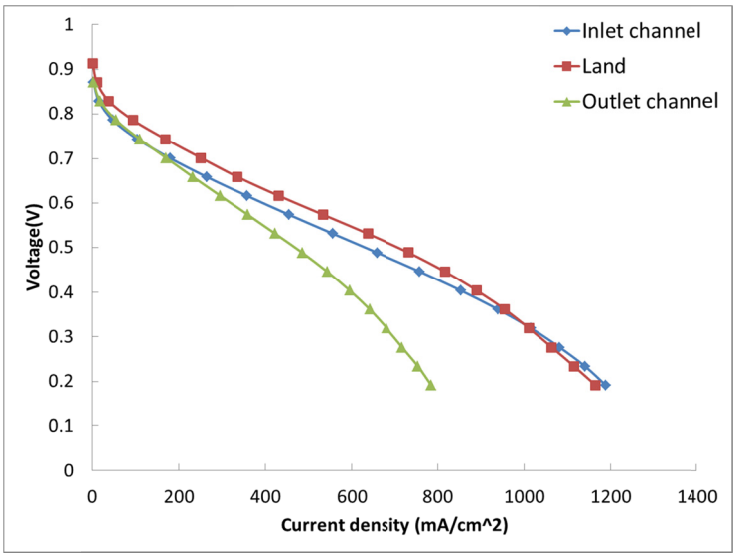

(a)

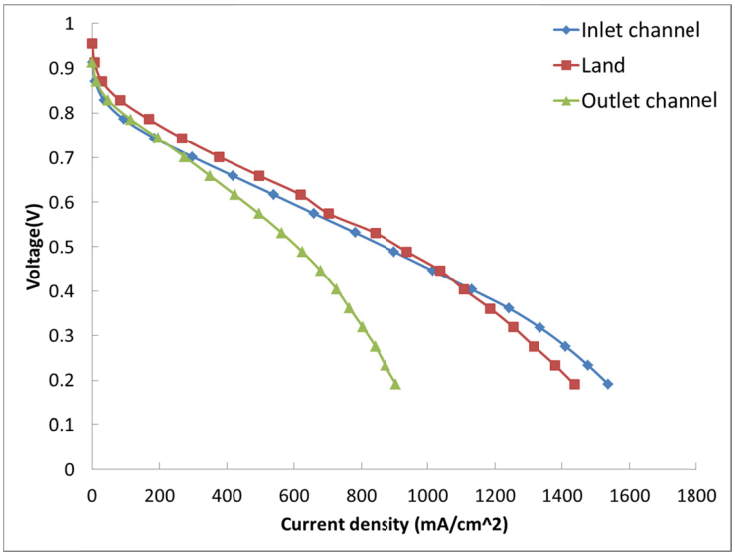

(b)

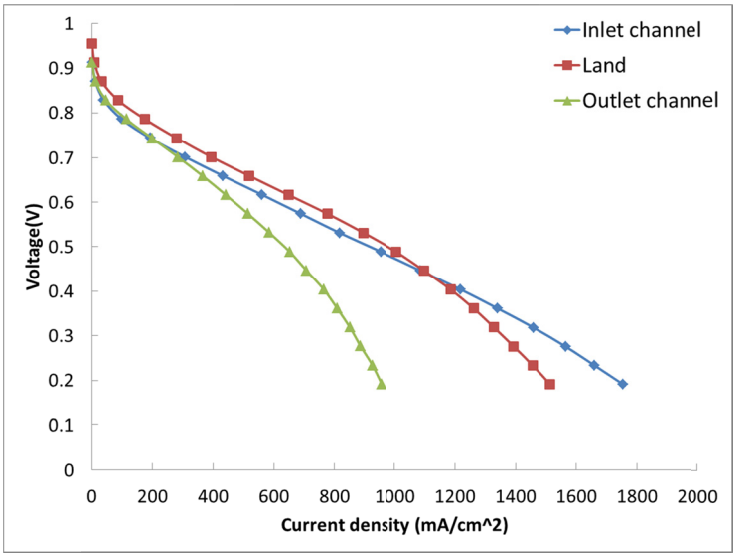

(c)

Fig. 5.5 Polarization curves under different cathode back pressures: anode and cathode are fully humidified, cell temperature=70℃ ; hydrogen flow rate=500 sccm, air flow rate=500 sccm; ambient pressure at anode side. (a) Cathode back pressure=0 KPa; (b) Cathode back pressure=200 KPa; (c) Cathode back pressure=250 KPa

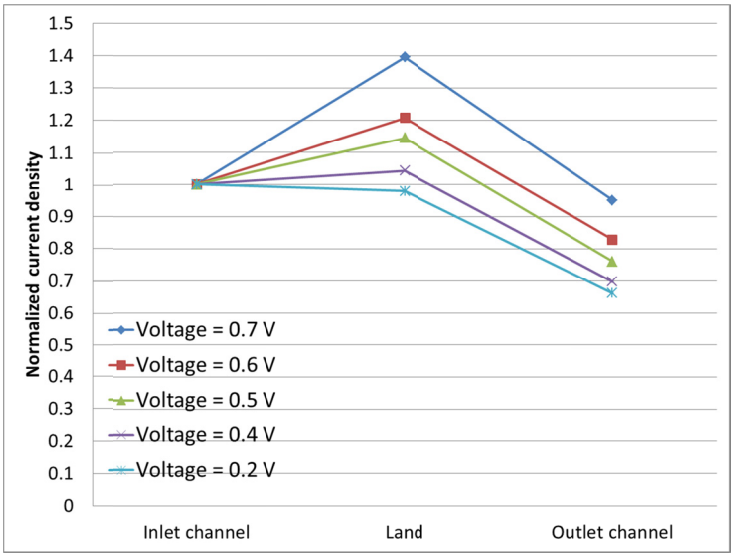

(a)

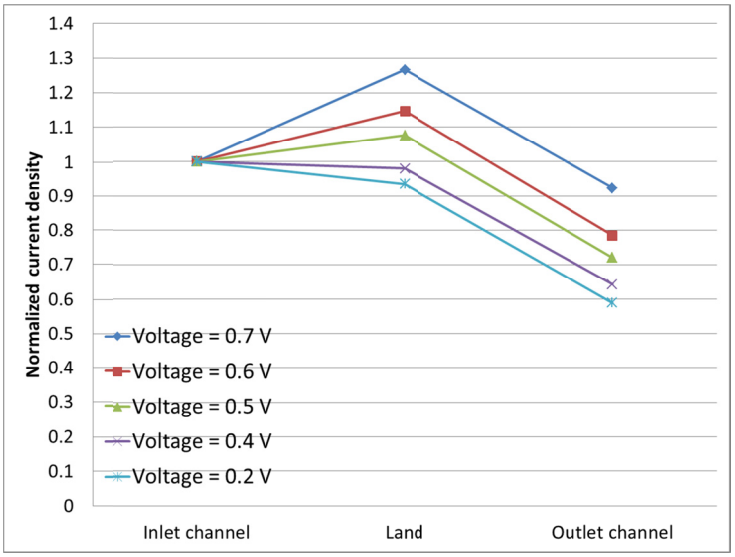

(b)

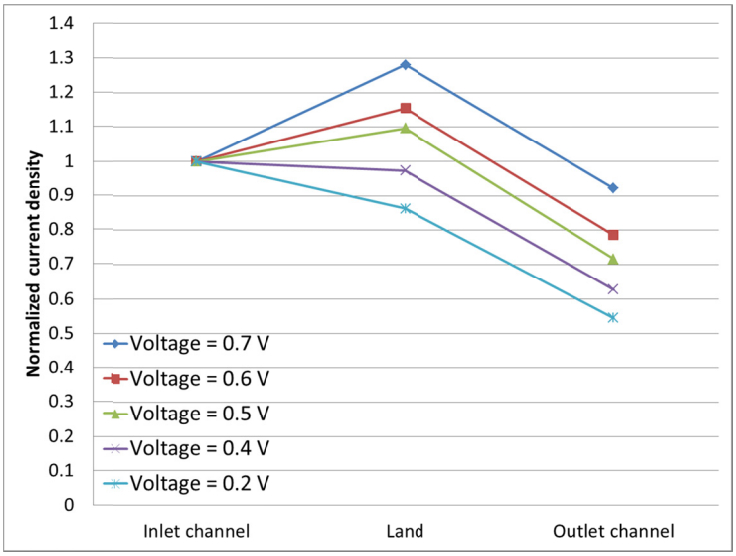

(c)

Fig. 5.6 Normalized current densities at different cathode back pressures: anode and cathode are fully humidified, cell temperature=70℃ ; hydrogen flow rate=500sccm, air flow rate=500 sccm; ambient pressure at anode side. (a) Cathode back pressure=0 KPa; (b) Cathode back pressure=200 KPa; (c) Cathode back pressure=250 KPa

5.4 Different cathode humidification temperatures

Fig. 5.7 shows a sample of direct measurement of current densities under the inlet channel, the land and the outlet channel for three CHTs. The fuel cell is operated at 70 °C, the back pressure is ambient, the hydrogen and air flow rates are 1000 and 2000 sccm, and the anode gas is fully humidified while the air gas humidification temperatures are set as 80, 70 and 30℃. When the CHT is equal to the cell temperature (70℃) as shown in Fig. 5.7 (b), the activation loss under the land is the smallest. This is due to the higher electrochemical areas (ECA) under the land [29]. When the CHT (80℃) is larger than the cell temperature (70℃) as shown in Fig. 5.7 (a), the current density comparison pattern is similar to that shown in Fig. 5.7 (b). However, the difference of activation loss under the inlet channel, the land and the outlet channel is reduced. It is consistent with the numerical results of Natarajan and Nguyen [88] that high inlet relative humidity can induce a much more uniform current distribution. When the cathode is highly dehydrated as shown in Fig. 5.7 (c), different phenomena is observed compared with Fig. 5.7 (a) and (b). The lateral current distribution becomes much more non-uniform. Due to the modeling work of Jeon et al. [89], under low cathode relative humidity condition, the water content in the channels near the outlet regions was higher than that near the inlet regions. This highly non-uniform distributed water content can lead to a highly non-uniform distributed current density.

In order to further elucidate the experimental results, Fig. 5.8 is produced to compare the current densities at different voltages. Under over humidified conditions as shown in Fig. 5.8 (a), at 0.7 V, the maximal lateral current density exists under the inlet channel, and the current density decreases along the lateral direction. Under fully

humidified conditions as shown in Fig. 5.8 (b), at 0.7 V, the current density under the inlet channel is slightly lower than the maximal lateral current density existing under the land. While under humidified as shown in Fig. 5.8 (c), at 0.7 V, the current density under the inlet channel is only about 50% of the maximum occurring under the land. So when the CHT decreases, the current density under the inlet channel decrease from the maximum current density, to only small portion of the maximum. This tendency remains the same for other cell voltages approximately. It can be seen clearly that during the change of CHT, the current density under the inlet channel undergoes tremendous change compared with that under other locations, especially at higher cell voltages

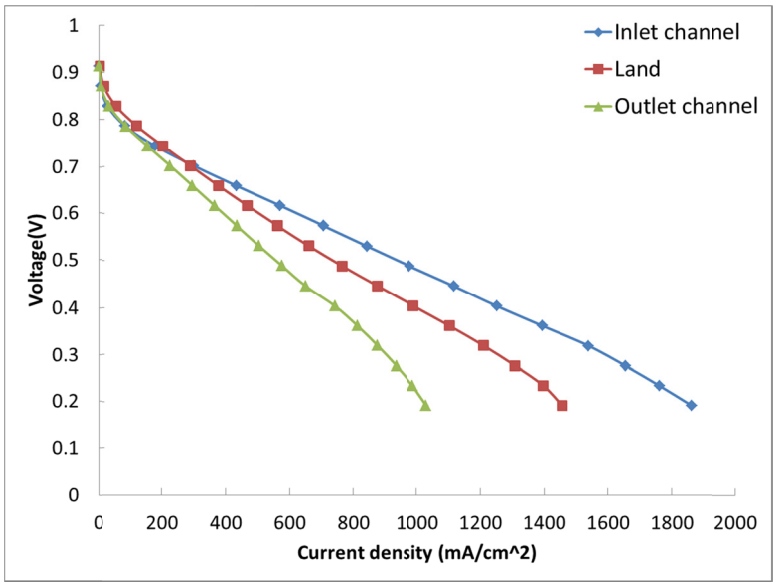

(a)

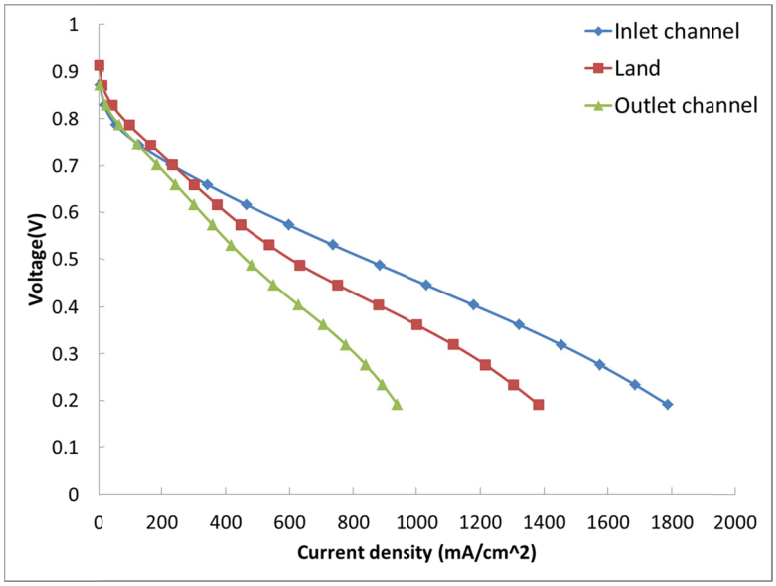

(b)

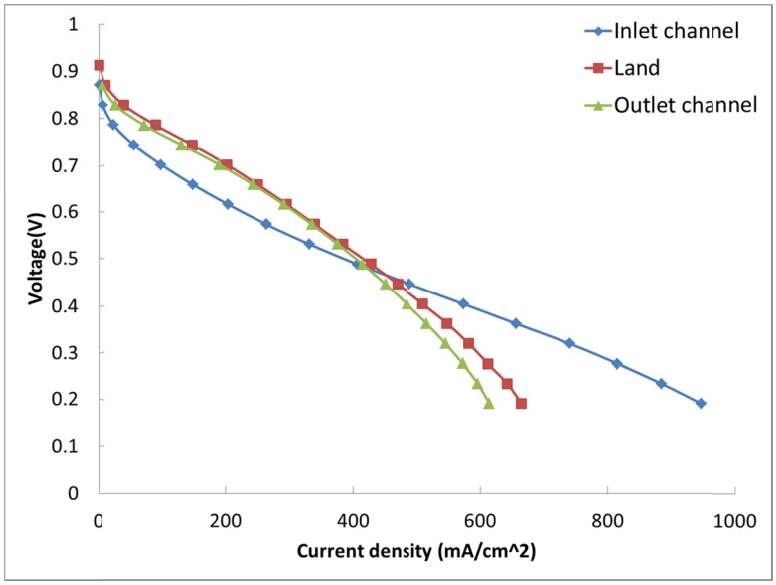

(c)

Fig. 5.7 Polarization curves under different cathode humidification temperatures (CHTs): cell temperature=70℃, anode is fully humidified; hydrogen flow rate=1000 sccm, air flow rate=2000 sccm; ambient pressure at both anode and cathode outlets. (a) CHT=80℃; (b) CHT=70℃; (c) CHT=30℃

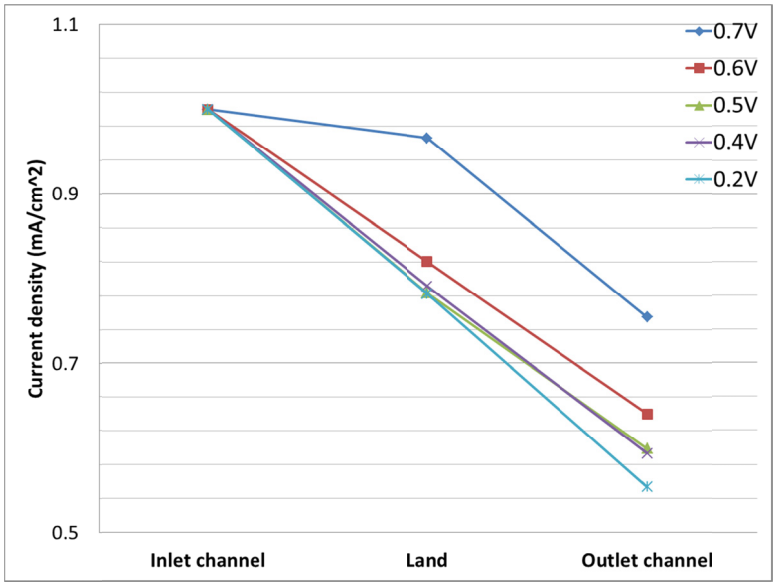
1.1
0.9
0.7
0.5
Current density (mA/cm^2)
0.7V
0.6V
0.5V
0.4V
0.2V
Inlet channel
Land
Outlet channel

(a)

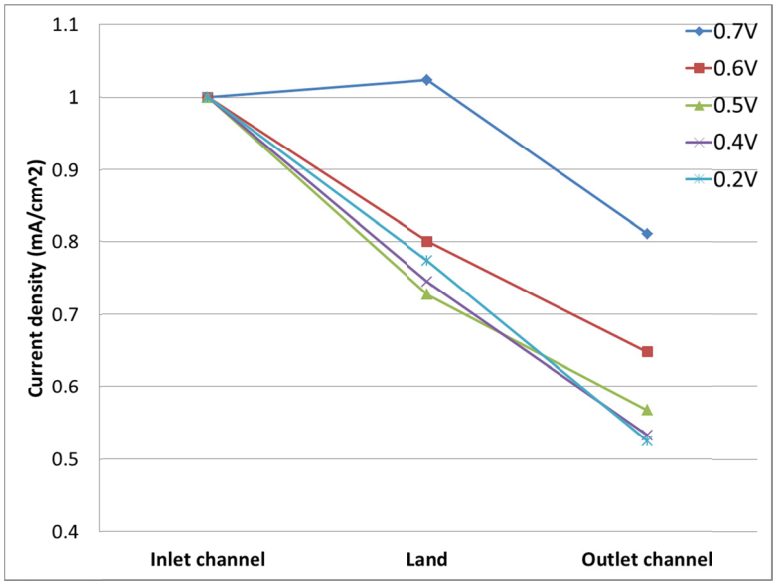
1.1
1
0.9
0.8
0.7
0.6
0.5
0.4
Current density (mA/cm^2)
0.7V
0.6V
0.5V
0.4V
0.2V
Inlet channel
Land
Outlet channel

(b)

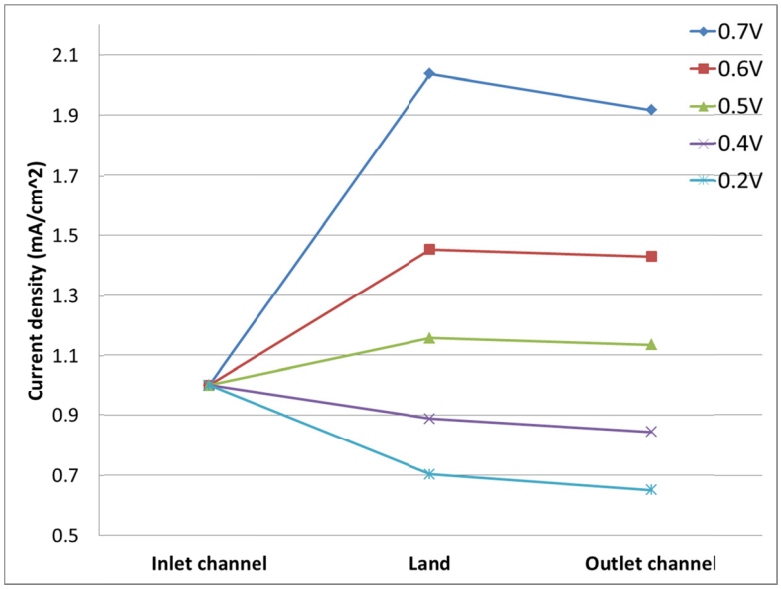

(c)

Fig. 5.8 Current density comparisons at certain cell voltages: cell temperature=70℃, anode is fully humidified; hydrogen flow rate=1000 sccm, air flow rate=2000 sccm; ambient pressure at both anode and cathode sides. (a) CHT=80℃; (b) CHT=70℃; (c) CHT=30℃

5.5 Local ECA under the channels and the land

Fig. 5.9 compares the cyclic voltammogram under the inlet channel, the land and the outlet channel at fully humidified condition. The fuel cell is operated at 70 °C, the back pressure is ambient, hydrogen is supplied at anode side at the rate of 500 sccm, and nitrogen is used at cathode side at the rate of 500 sccm. Both the anode and cathode gases are fully humidified. The voltage scan rate is 0.15 V/s. The results show that the ECA under the land is the highest. This is due to the direct compression under the land than that under the channels [29]. It should be noticed that the ECA under the outlet channel is much lower than that under the inlet channel. This difference comes from the different

"impinging type" under the two channels similar to Fig. 5.2. Under the inlet channel, the nitrogen gas flows into the GDL, while under the outlet channel, the nitrogen gas flows out from the GDL, thus the proton and catalyst accessibility under the inlet channel is much higher than that under the outlet channel.

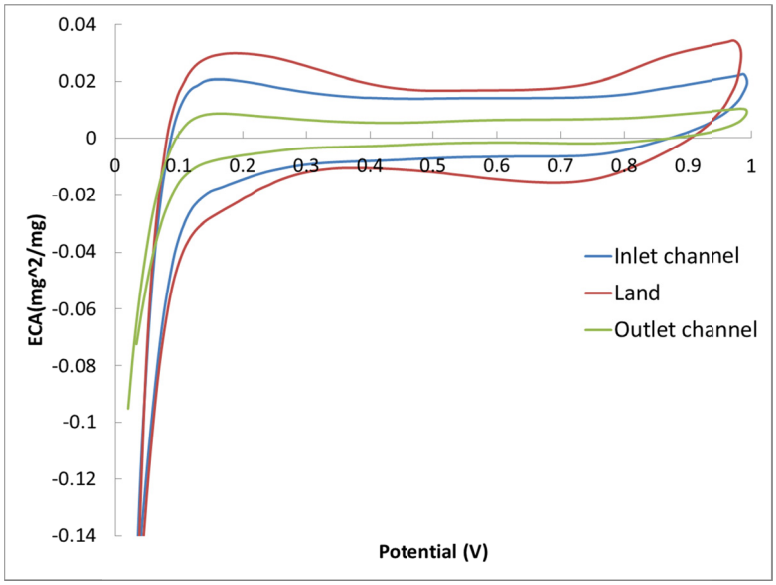

Fig. 5.9 Cyclic voltammogram comparisons: cell temperature=70℃, anode and cathode are fully humidified; hydrogen flow rate=500 sccm, nitrogen flow rate=500 sccm; ambient pressure at both anode and cathode outlets; voltage scan rate=0.15 V/s

5.6 Summary

Partially-catalyzed MEA method is used to separately measure the current densities under the inlet channel, the land and the outlet channel in a PEM fuel cell with an interdigitated cathode flow field. The local current densities under the three different areas are also made at three different cathode flow rates, different cathode back pressures

and different cathode humidification temperatures (CHTs), in order to study if these operation conditions have significant effects on the variation pattern of the local current densities. The electrochemical areas (ECA) under the inlet channel, the land and the outlet channel are also measured. The following conclusions can be made from the experimental results.

- Current density under the outlet channel is much lower than that under the inlet mainly due to the difference in the angles formed by the velocity vector and the mass flux vector.
- Cathode flow rate does not affect the pattern of relative magnitudes of local current densities among the three different areas. Current density under the land is higher than that under the inlet channel in the high cell voltage region (>0.4V in this study) and lower in the low cell voltage region (<0.4V in this study).
- Cathode back pressures have negligible effect on the pattern of relative magnitudes of local current densities.
- The humidification temperature affects the local current density in different patterns. The current density under the inlet channel decreases significantly due to the lower local water content.
- ECA under the outlet channel is smaller than that under the inlet channel mainly may due to the different proton and catalyst accessibility under the two channels.

CHAPTER 6

LATERAL CURRENT DISTRIBUTION

6.1 Lateral current density distribution

From Fig. 4.4, it shows that in order to obtain the lateral current distribution of interdigitated flow field, the current under seven different lateral positions are measured. The polarization curves under seven positions are plotted in Fig. 6.1. First of all, at the same positions, the current is increased with larger cathode flow rate. Besides that, under different air flow rates, the polarization curves differences between different locations shows similar tendency.

In order to view the tendency clearly, the current density in the lateral direction under high and low voltages are shown in Fig. 6.2 and Fig. 6.3. P1-P7 are experimental measurement points for this 1mm-2 mm-1mm flow field geometry. The flow scenarios difference between this field and the full interdigitated flow field should be noticed.

For the flow distribution in full interdigitated flow field, the gas in each inlet channel would distribute to two adjacent outlet channels by convection, and each outlet channel would receive gas from two adjacent inlet channels. However, in the geometry of this study, gas could only go from one inlet channel to one outlet channel. So this 1mm-2mm-1mm geometry can be used to simulate the flow scenario in full interdigitated flow field with 2 mm-2 mm-2mm geometry. By this consideration, no flux boundary conditions are applied to P0 and P8. So the current density of P0 is set to be equal to that of P1, and the current density of P8 is set to be equal to that of P7. For all the cases, it is shown that the

current density under the land is the highest, and the current density under the outlet channel is the lowest. The reasons of the performance difference among that under the inlet channel, the land and the outlet channel will be discussed later by electrochemical methods, i.e. CV and EIS methods.

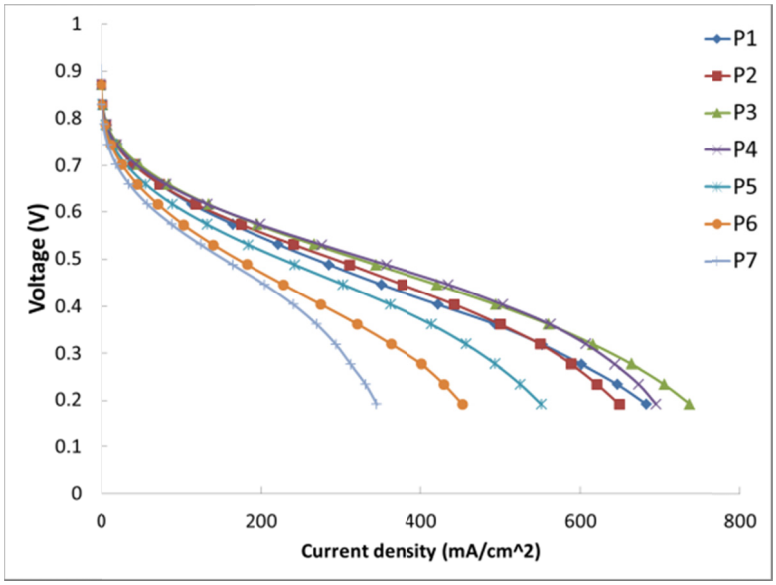

(a)

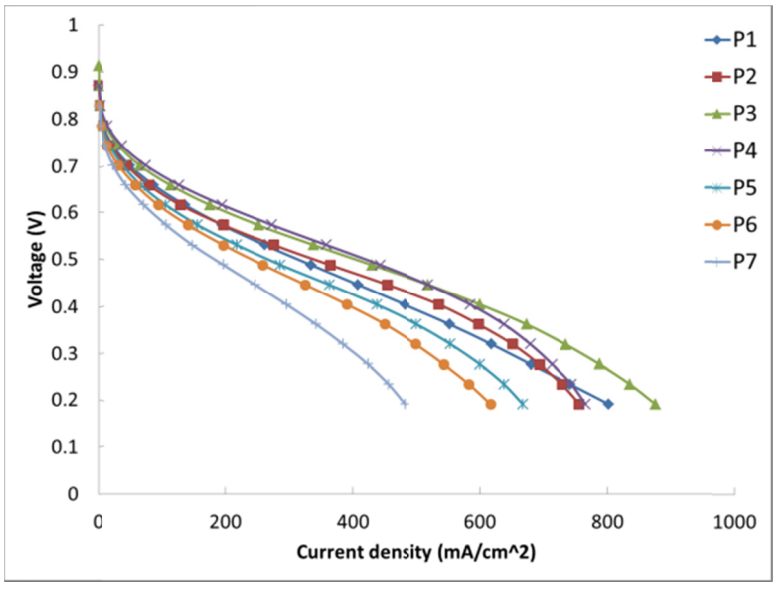

(b)

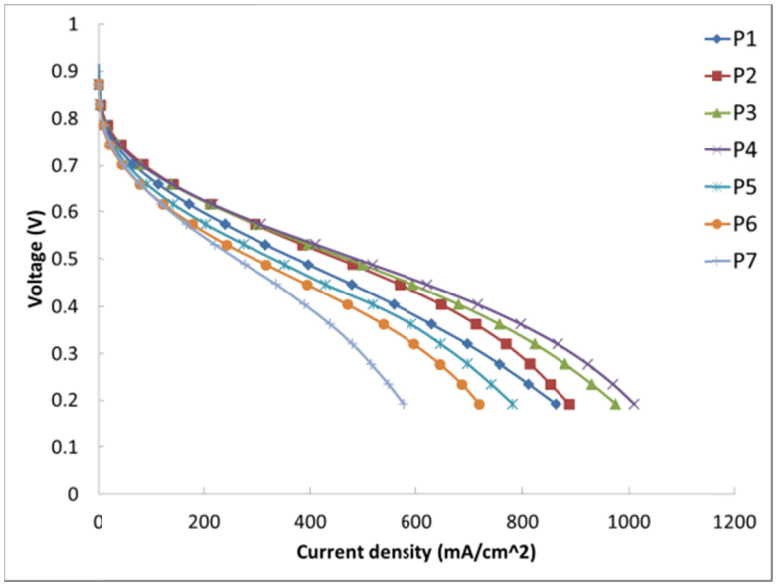

(c)

Fig. 6.1 Polarization curves comparisons under different locations: anode and cathode are fully humidified, cell temperature=70℃; hydrogen flow rate=500 sccm; ambient pressure at both anode and cathode sides. (a) Air flow rate=500 sccm; (b) Air flow rate=800 sccm; (c) Air flow rate=1000 sccm.

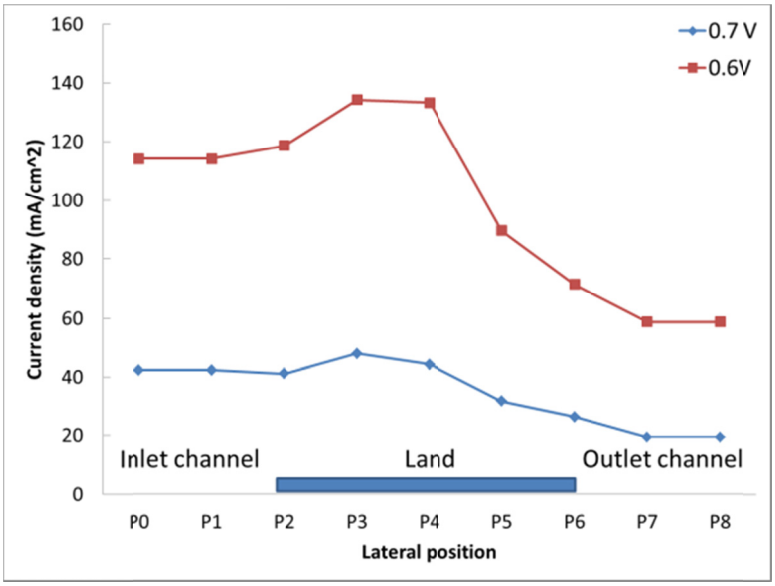
0.7 V
0.6V
Current density (mA/cm^2)
160
140
120
100
80
60
40
20
0
Inlet channel
Land
Outlet channel
P0
P1
P2
P3
P4
P5
P6
P7
P8
Lateral position

(a)

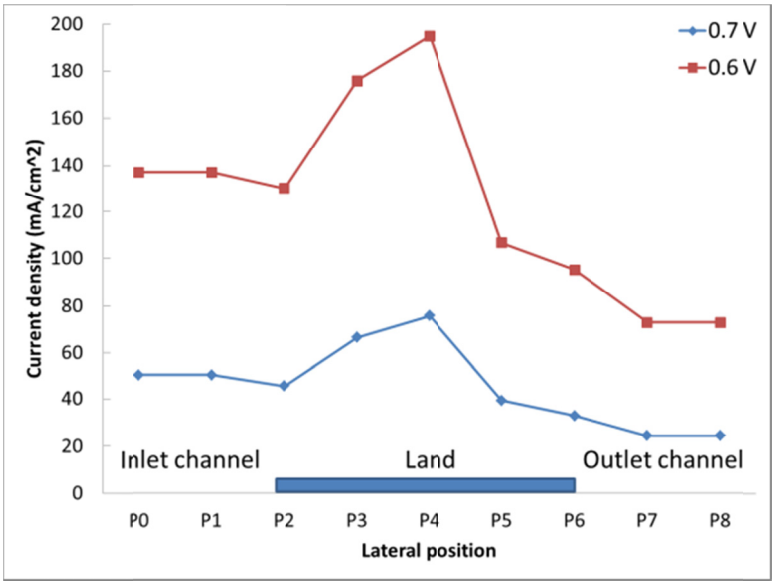
0.7 V
0.6 V
Current density (mA/cm^2)
200
180
160
140
120
100
80
60
40
20
0
Inlet channel
Land
Outlet channel
P0
P1
P2
P3
P4
P5
P6
P7
P8
Lateral position

(b)

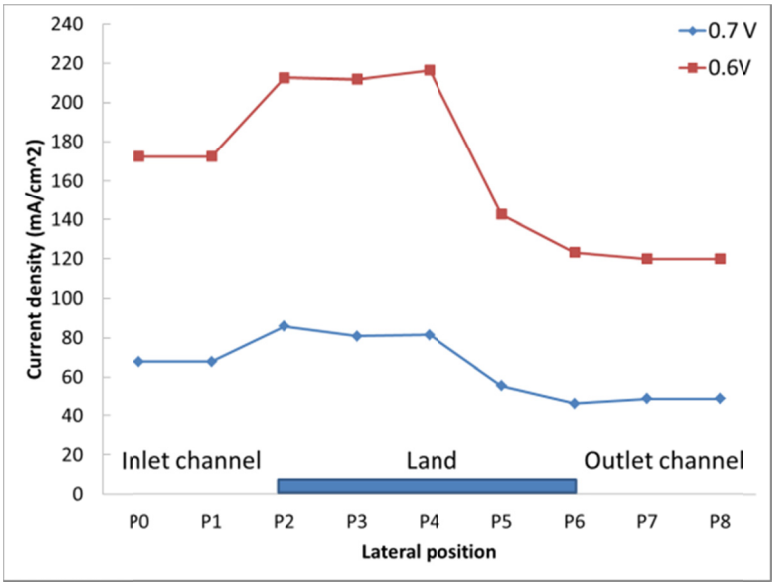

(c)

Fig. 6.2 Current density comparisons under different locations: anode and cathode are fully humidified, cell temperature=70℃; hydrogen flow rate=500 sccm; ambient pressure at both anode and cathode sides; cell voltage= 0.7V, 0.6V. (a) Air flow rate=500 sccm; (b) Air flow rate=800 sccm; (c) Air flow rate=1000 sccm.

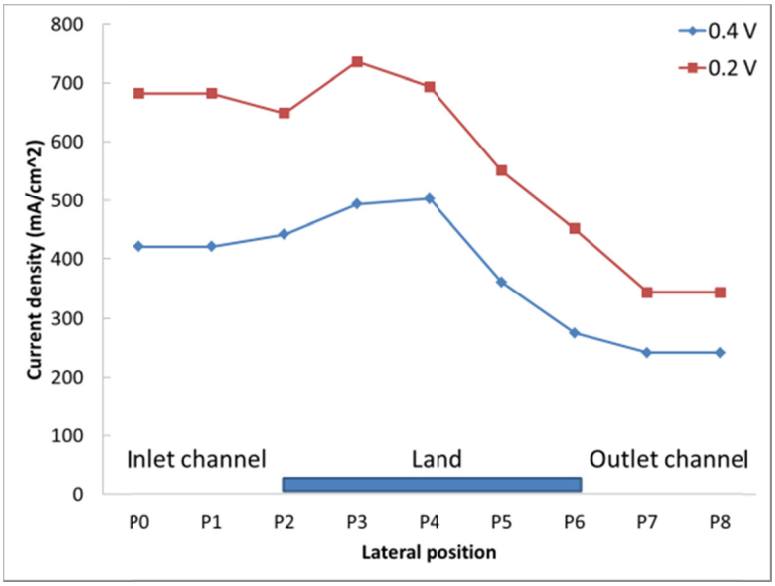
800
700
600
500
400
300
200
100
0
Current density (mA/cm^2)
0.4 V
0.2 V
Inlet channel
Land
Outlet channel
P0
P1
P2
P3
P4
P5
P6
P7
P8
Lateral position

(a)

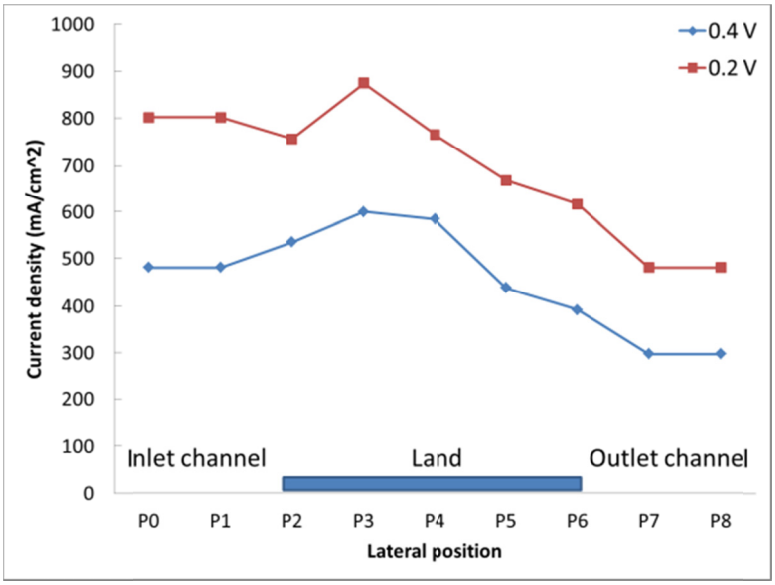
1000
900
800
700
600
500
400
300
200
100
0
Current density (mA/cm^2)
0.4 V
0.2 V
Inlet channel
Land
Outlet channel
P0
P1
P2
P3
P4
P5
P6
P7
P8
Lateral position

(b)

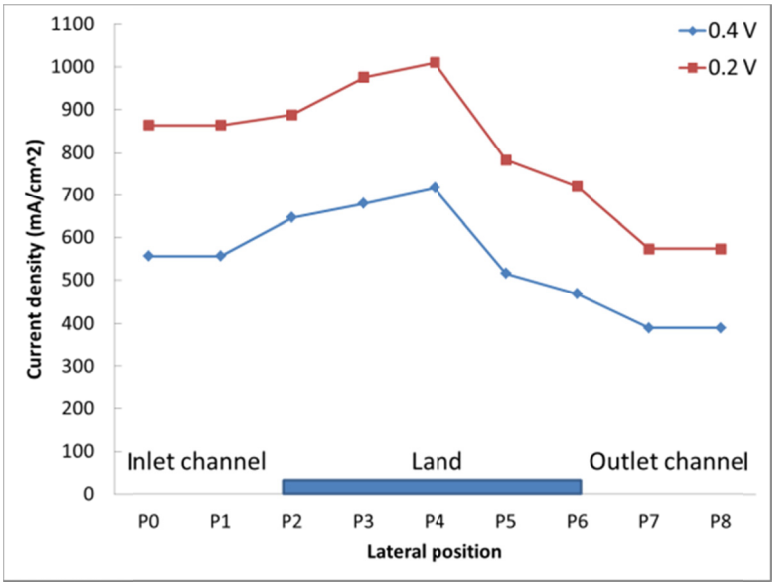

(c)

Fig. 6.3 Current density comparisons under different locations: anode and cathode are fully humidified, cell temperature=70℃; hydrogen flow rate=500 sccm; ambient pressure at both anode and cathode sides; cell voltage= 0.4V, 0.2V. (a) Air flow rate=500 sccm; (b) Air flow rate=800 sccm; (c) Air flow rate=1000 sccm.

6.2 Lateral ECA distribution

Fig. 6.4 shows the lateral ECA distribution. There are two phenomenon should be noticed. First of all, the ECA under the land is higher than that under the channels. This is due to the higher direct compression under the land [29]. Besides, the ECA under the outlet channel is lower than that under the inlet channel. Under ideal compression condition, the local compression forces under the two channels are equal. Comparing with the ECA under the inlet channel, the lower ECA under the outlet channel may be not due to the smaller compression force, but the possible different catalyst and protons utilizations under the two channels as discussed in Chapter 5. Since ECA is an important

factor to determine current density, this non-uniform lateral ECA distribution can be one of the reasons for the non-uniform lateral current density distribution. The distribution pattern of Fig. 6.4 is consistent with that of Fig. 6.2 and Fig. 6.3.

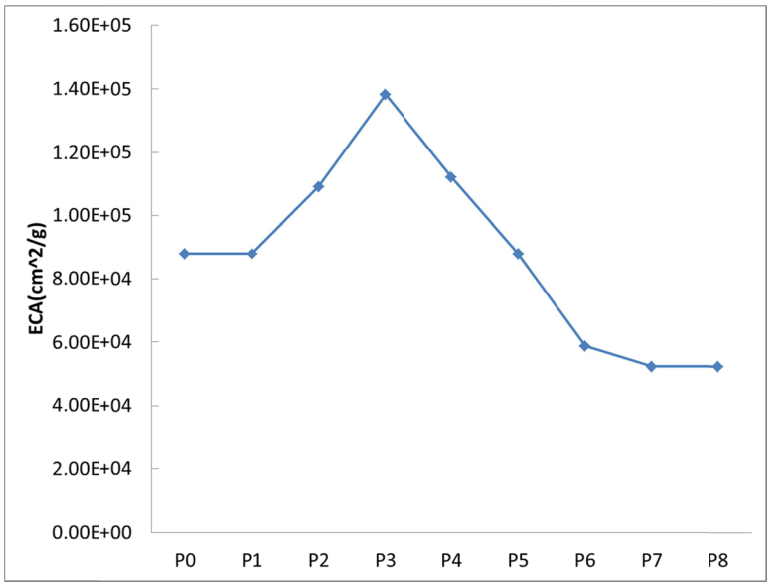

Fig. 6.4 Electrochemical areas (ECA) comparisons under different locations

6.3 Lateral impedance distribution

An equivalent circuit model used in this study is shown in Fig. 6.5. R_o is the ohmic resistance of the PEM fuel cell. Both anode and cathode reaction kinetics are considered. The impedance of a surface with electrochemical reactions can be modeled as a parallel combination of a resistor and a capacitor [5]. The double layer capacitances are modeled by capacitors $CPEa$ and $CPEc$. The resistors which present the charge transfer resistances are R_a and R_c. In this study, since the EIS tests are conducted within the activation loss dominate and ohmic loss dominate regions, the mass transport loss is neglected.

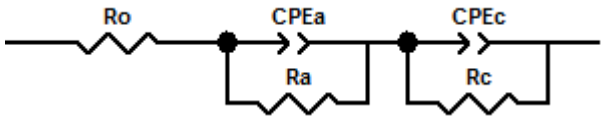

Fig. 6.5 Equivalent circuit model of electrochemical impedance spectroscopy (EIS)

The Nyquist plots under different locations are measured. Fig. 6.6 and Fig. 6.7 show the EIS experimental and model results under the current densities of 50 and 100(mA/cm^2) for the air flow rate of 1000, 800, 500 sccm. The ohmic resistance, anode and cathode charge transfer resistances are shown in Fig. 6.8. From Fig. 6.8, the ohmic resistances under different conditions change little. Because ohmic resistance is mainly determined by the contact resistance between contacting components and the ohmic resistance of each components [87], the results are reasonable since the air flow rate and EIS test current density cannot change the intrinsic electrical properties of PEM fuel cells components. The anode charge transfer resistance does not change obviously under different conditions. Since the anode reaction rate is so fast that the operation condition does not affect the anode charge transfer resistance significantly. However, the lateral cathode charge transfer resistance is not uniform distributed. The cathode charge transfer resistance under the land is the smallest, and cathode charge transfer resistances under the two channels are close to each other. Since the charge resistance of oxygen reduction reaction (ORR) is one of the indicators of the catalyst utilization and ECA [87], it is reasonable to state that the catalyst utilization and ECA distribution in the lateral direction is not uniform. The non-uniform lateral cathode charge transfer resistance distribution could be another reason for the non-uniform lateral current density distribution.

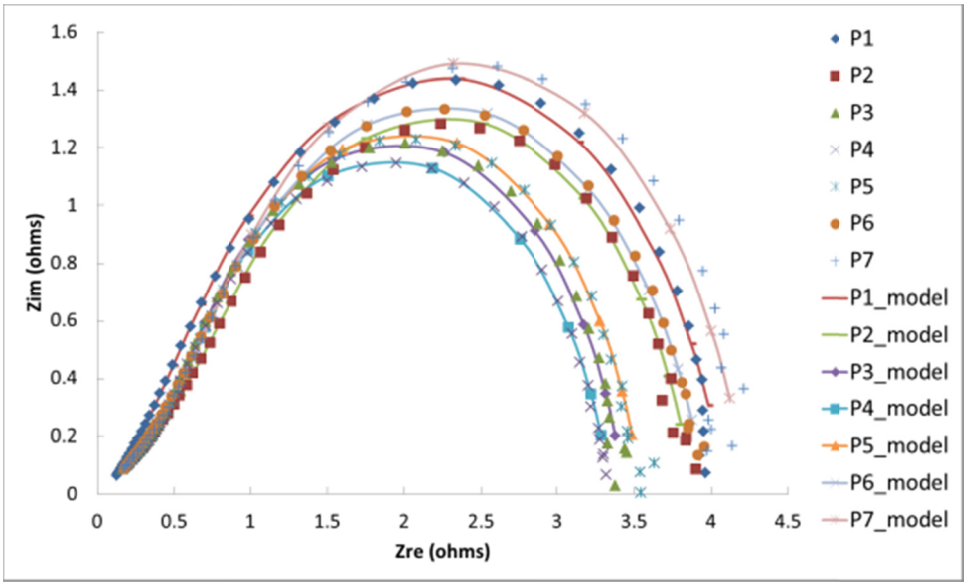
Zim (ohms)
Zre (ohms)
P1
P2
P3
P4
P5
P6
P7
P1_model
P2_model
P3_model
P4_model
P5_model
P6_model
P7_model

(a)

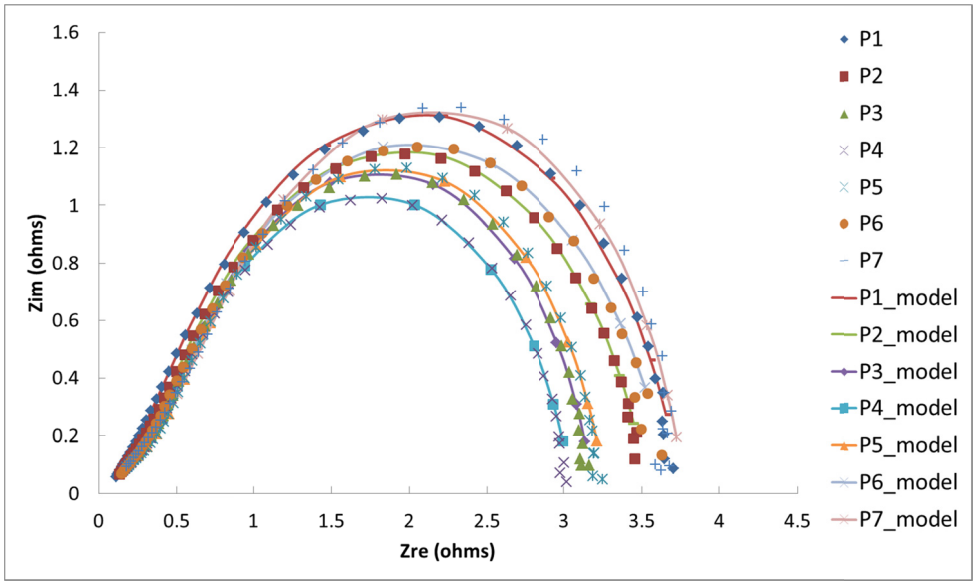
Zim (ohms)
Zre (ohms)
P1
P2
P3
P4
P5
P6
P7
P1_model
P2_model
P3_model
P4_model
P5_model
P6_model
P7_model

(b)

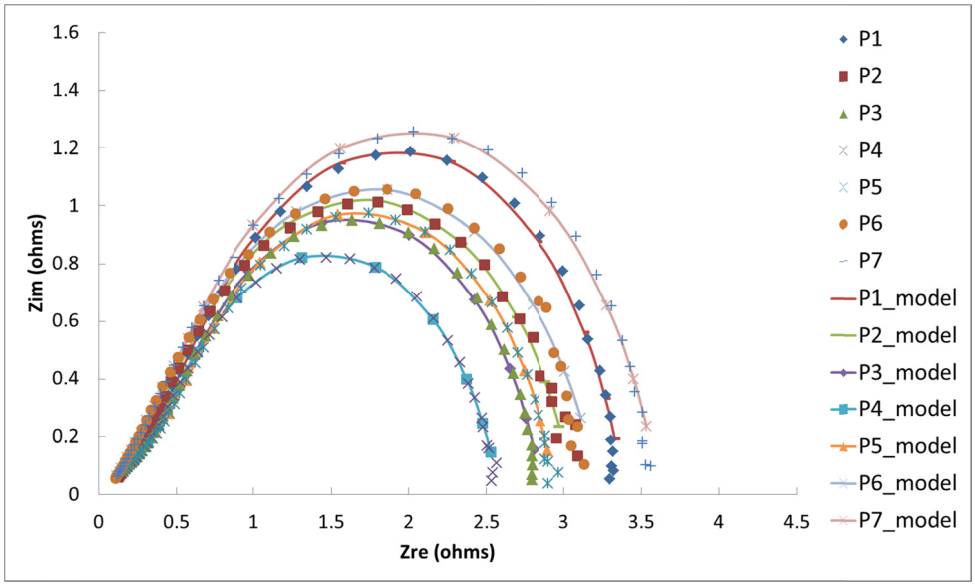

(c)

Fig. 6.6 Electrochemical impedance spectroscopy (EIS) comparisons under different locations when current density = $50 mA/cm^2$: hydrogen flow rate=500 sccm (a) Air flow rate = 500 sccm; (b) Air flow rate = 800 sccm; (c) Air flow rate = 1000 sccm.

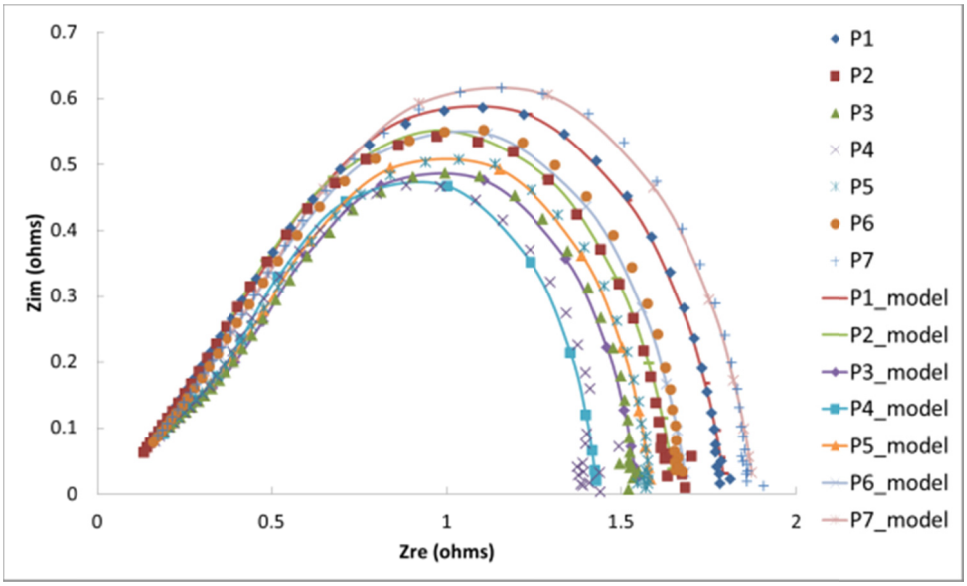
0.7
0.6
0.5
0.4
0.3
0.2
0.1
0
Zim (ohms)
0
0.5
1
1.5
2
Zre (ohms)
P1
P2
P3
P4
P5
P6
P7
P1_model
P2_model
P3_model
P4_model
P5_model
P6_model
P7_model

(a)

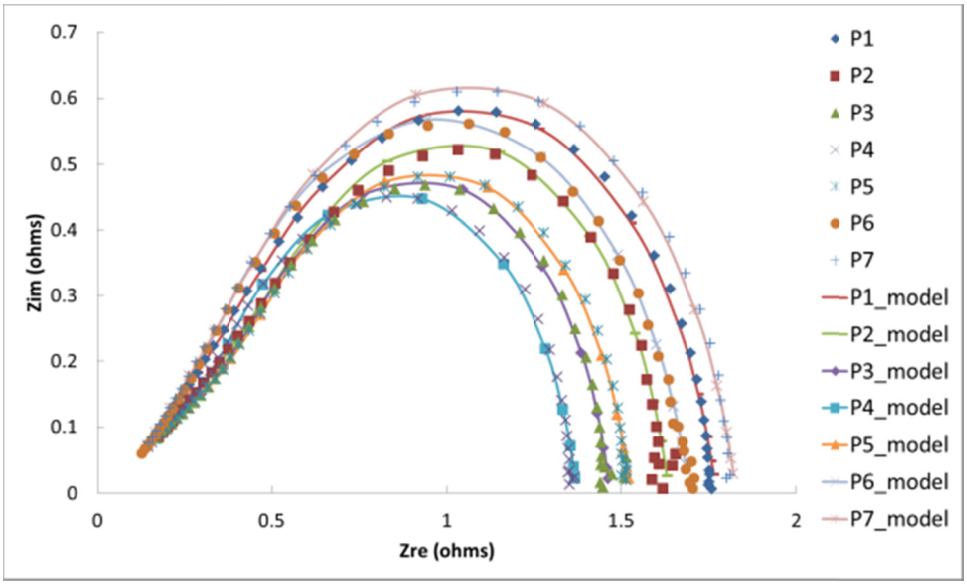
0.7
0.6
0.5
0.4
0.3
0.2
0.1
0
Zim (ohms)
0
0.5
1
1.5
2
Zre (ohms)
P1
P2
P3
P4
P5
P6
P7
P1_model
P2_model
P3_model
P4_model
P5_model
P6_model
P7_model

(b)

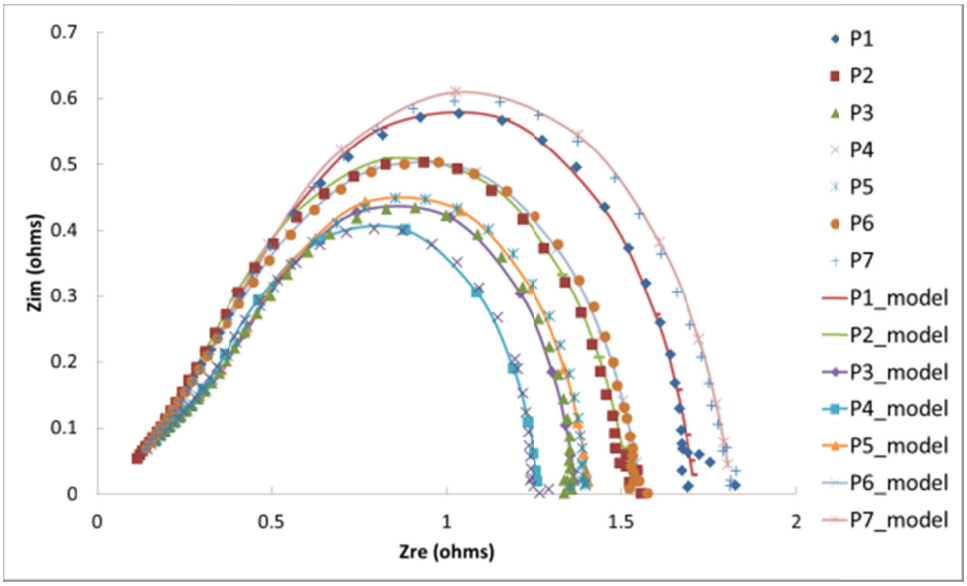

(c)

Fig. 6.7 Electrochemical impedance spectroscopy (EIS) comparisons under different locations when current density = $200\mathrm{mA/cm^2}$: hydrogen flow rate=500 sccm (a) Air flow rate = 500 sccm; (b) Air flow rate = 800 sccm; (c) Air flow rate = 1000 sccm.

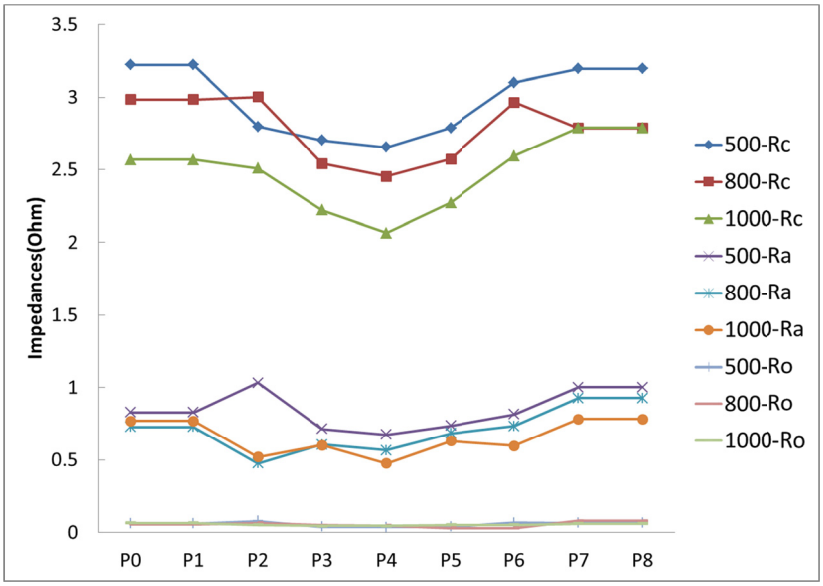

(a)

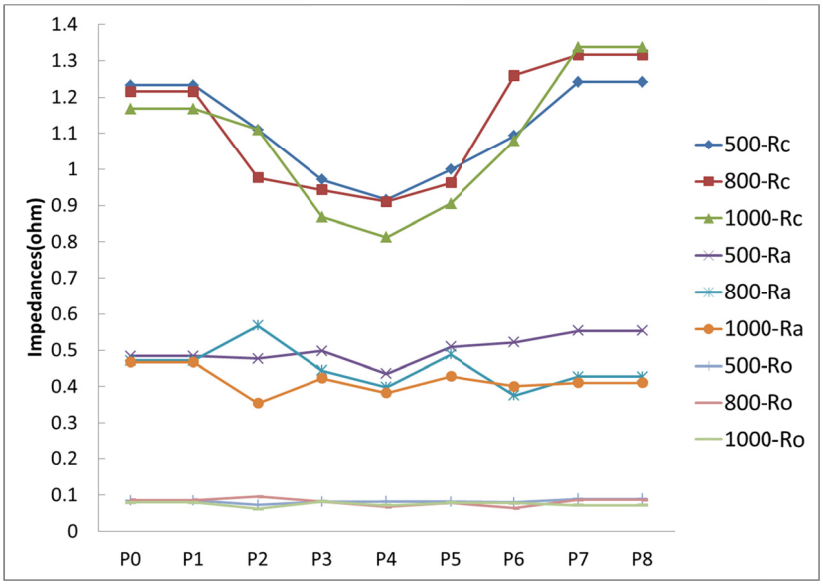

(b)

Fig. 6.8 Normalized resistance (Legend: 500, 800, 1000 represent air flow rate; R_c, R_a, R_o represent cathode, anode charge transfer resistance, ohmic resistance). (a) $50mA/cm^2$; (b) $200mA/cm^2$.

6.4 Summary

The lateral current distribution in a PEM fuel cell is experimentally studied. The following conclusions could be concluded through this study:

- The lateral current density is not uniformly distributed in a PEM fuel cell with a single interdigitated flow field. In most typical PEM fuel cells operation voltages, the current under the land is the highest, and the current under the inlet channel is much higher than that under the outlet channel.
- The non-uniform ECA distribution is one of reasons for the non-uniform lateral current density distribution. The ECA under the land is the highest, and the ECA under the outlet channel is lower than that under the inlet channel.
- In addition, the non-uniform cathode charges transfer resistance (R_c) distribution also contributes to the non-uniform lateral current density distribution. The R_c under the land is the smallest, and the R_c under the two channels are close to each other.

CHAPTER 7

MODELING METHODOLOGY

7.1 Computation domain

In this study, a two-dimensional model is developed. Fig. 7.2 shows the schematic of a full interdigitated flow field. In a full interdigitated flow field, both inlet and outlet are divided into many channels, which are separated by the lands.

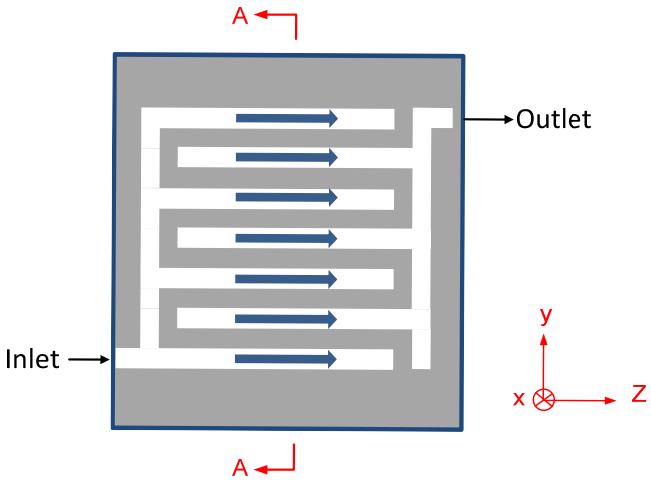

Fig. 7.1 Schematic of a full interdigitated flow field

Fig. 7.2 shows one representative unit of A-A view of the full flow field. In order to save computation time, the computation domain is selected as in Fig. 7.2. This model contains both anode and cathode, and the computation domain includes gas diffusion layers, catalyst layers, proton exchange membrane. The widths of the two channels are 1 mm, and the width of the land is 2 mm.

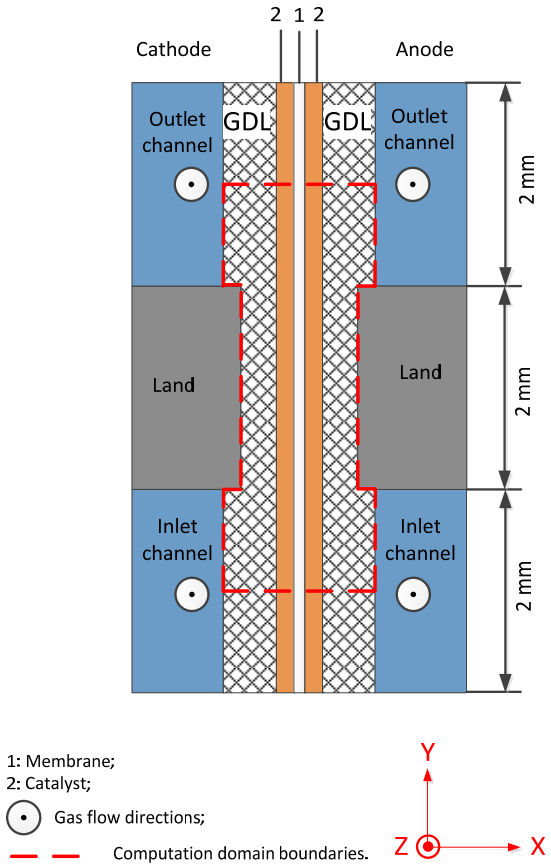

Fig. 7.2 Schematic of computation domain: one representative unit of A-A view

7.2 Model equations

- Mass conservation [90]:

$$\nabla(\rho \boldsymbol{u}) = \begin{cases} 0 & GDL, Membrane \\ R_i & Catalyst\ layer \end{cases} \tag{7.1}$$

Where ρ is density ($\mathrm{kg/m^3}$), $\boldsymbol{u}$ is velocity ($\mathrm{m/s}$), and R_i is mass source term ($\mathrm{kg/m^3 \cdot s}$)and defined in Eq. (7.12).

- Momentum equation [91]:

$$\frac{\rho}{\varepsilon_p}\left((\boldsymbol{u}\cdot\nabla)\frac{\boldsymbol{u}}{\varepsilon_p}\right) = -\nabla p + \nabla\cdot\left[\frac{1}{\varepsilon_p}\mu\left(\nabla\boldsymbol{u}+(\nabla\boldsymbol{u})^{\mathrm{T}}\right)-\frac{2}{3\varepsilon_p}\mu(\nabla\cdot\boldsymbol{u})I\right] + \begin{cases}-\frac{\mu}{\kappa}\boldsymbol{u} & GDL, Membrane\\ -\left(\frac{\mu}{\kappa}+R_i\right)\boldsymbol{u} & Catalyst\ layer\end{cases} \quad (7.2)$$

Where ε_p is porosity, μ is dynamic viscosity ($\mathrm{kg/m\cdot s}$), κ is the permeability ($\mathrm{m^2}$).

- Species transport equation:

Maxwell-Stefan diffusion model is considered [92]:

$$\rho(\boldsymbol{u}\cdot\nabla)\omega_i = \nabla\cdot\left(\rho\omega_i\sum_{k=1}^{Q}D_{ik}^{*}\,d_k\right)+\begin{cases}0 & GDL\\ R_i & Catalyst\ layer\end{cases} \quad (7.3)$$

$$d_k = \nabla x_k + \frac{1}{p}[(x_k-\omega_k)\nabla p] \quad (7.4)$$

Where ω_i is the mass fraction, x_k is the mole fraction, D_{ik}^{*} is the multicomponent Fick diffusivities(m^2/s), and d_k is the diffusion driving force acting on specie k ($1/m$).

The multicomponent Fick diffusivities $\mathrm{D_{ik}^{*}}$ could be related to the multicomponent Maxwell-Stefan diffusivities$\mathrm{D_{ik}}$ [92]:

$$\frac{x_i x_k}{D_{ik}} = -\omega_i\omega_k\frac{\sum_{j\neq i}(adjB_i)_{jk}}{\sum_{j\neq i}D_{ij}^{*}(adjB_i)_{jk}}, (B_i)_{kj} = D_{kj}^{*}-D_{ij}^{*}, i\neq j \quad (7.5)$$

Where $(adjB_i)_{jk}$ is the j^{th} component of the adjoint of the matrix B_i.

- Potential equation:

  Membrane phase potential equations [91]:

$$\nabla(-\sigma_m \nabla\Phi_m) = \begin{cases} j^a & anode\ catalyst\ layer \\ j^c & cathode\ catalyst\ layer \\ 0 & Membrane \end{cases} \tag{7.6}$$

Where σ is the conductivity $(\mathrm{S/m})$, Φ is the potential (V), j is the local current density $(\mathrm{A/m^2})$. Subscript m represents membrane phase. Superscripts a and c represent anode and cathode sides.

- Solid phase potential equations [91]:

$$\nabla(-\sigma_s \nabla\Phi_s) = \begin{cases} -j^a & anode\ catalyst\ layer \\ -j^c & cathode\ catalyst\ layer \\ 0 & GDL \end{cases} \tag{7.7}$$

In this equation, subscript s represents solid phase.

- Reaction rate equation:

The reaction rate j^a and j^c could be calculated as [90]:

$$j^a = a_v^a j_0^{a,ref} \left(\frac{C_{H_2}}{C_{H_2}^{ref}}\right)^{0.5} \left(\frac{(\alpha_a^a + \alpha_c^a)F}{RT}\right)\eta^a \tag{7.8}$$

$$j^c = a_v^c j_0^{c,ref} \left(\frac{C_{O_2}}{C_{O_2^{ref}}}\right)\left(\exp\left(\frac{\alpha_a^c F\eta^c}{RT}\right) - \exp\left(\frac{-\alpha_c^c F\eta^c}{RT}\right)\right) \tag{7.9}$$

Where a_v is the specific reaction area $(1/\mathrm{m})$, j_0 is the exchange current density $(\mathrm{A/m^2})$, C is the mole concentration $(\mathrm{mol/m^3})$, α_a is the anodic charge transfer coefficient, α_c is the cathodic charge transfer coefficient, η is the overpotential (V), F is the Faraday constant (96,487 C/mol), R is the universal gas constant (8.314 $J \cdot mol^{-1} \cdot K^{-1}$), and T is the temperature (K).

The specific reaction area a_v is given by [93]:

$$a_v = \frac{[Pt]ECA}{t_{cl}} \tag{7.10}$$

Where $[Pt]$ is the catalyst loading (mg/cm^2), ECA is the electrochemical areas (cm^2/kg) and t_{cl} is the catalyst thickness (m).

The overpotential η is given by [91]:

$$\eta = \Phi_s - \Phi_m - E_{OCV} \tag{7.11}$$

Where E_{OCV} is the open circuit voltage (V).

- Mass source terms [90]:

$$R_{H_2} = -\frac{j^a}{2F} M_{H_2}$$

$$R_{O_2} = -\frac{j^c}{4F} M_{O_2} \tag{7.12}$$

$$R_{H_2O} = \frac{j^c}{2F} M_{H_2O}$$

Where M is the molar mass (kg/mol).

7.3 Boundary conditions

In order to illustrate the boundary conditions clearly, each boundary is numbered as shown in Fig. 7.3. The boundary conditions are summarized in Table 7.1. It should be noticed that the cathode catalyst layer has been divided into eight segments. The current under each segment will be evaluated. Since inside domain, all the model equations are continuous, no specific model equations are needed at the interface between GDL and catalyst layer at both sides. For the same reasons, only continuous conditions are applied at the boundaries between two adjacent segments.

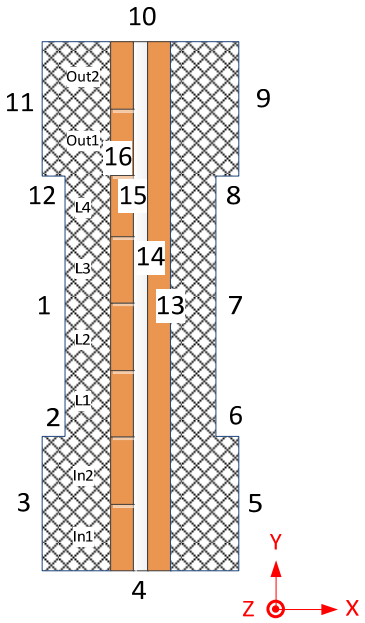

Fig. 7.3 Boundaries notations of domain

Table 7.1 Boundaries conditions summary

B.C.S	Boundaries	Expression
Electric isolation	2, 3,4, 5, 6, 8, 9, 10, 11, 12	$-\boldsymbol{n}\cdot\boldsymbol{i}=0$
No flux for all species	1, 2, 4, 6, 7, 8, 10, 12	$-\boldsymbol{n}\cdot\boldsymbol{u_i}=0$ ($\boldsymbol{u_i}$: $velocity\ of\ species\ i$)
No flux for gases	14, 15	$-\boldsymbol{n}\cdot\boldsymbol{u_i}=0$ ($\boldsymbol{u_i}$: $velocity\ of\ gas\ i$)
No slip wall	1, 2, 4, 6, 7, 8, 10, 12, 14, 15	$\boldsymbol{u}=\boldsymbol{0}$
Anode inlet	5	Mass fraction: $\omega_i=\omega_{0,i}$ Constant flow rate
Anode outlet	9	Pressure: $P_{anode\ out}=0$
Cathode inlet	3	Mass fraction: $\omega_i=\omega_{0,i}$ Contant flow rate
Cathode outlet	11	Pressure: $P_{cathode\ out}=0$

7.4 Assumptions summary

- The flow is laminar flow within the computation domain;
- Steady state and single phase flow scenarios are assumed;
- The gas is compressible and ideal;
- Besides Darcy term, additional Brinkman term in momentum equation is added with the consideration of possible transition flow between boundaries;
- Instead of Fick's diffusion equation, the Maxwell-Stefan diffusion model is used which could be used to model the non-dilute mixture and the interacting effect among species of the mixture.

7.5 Geometric parameters and physical properties

The geometric parameters are listed in Table 7.2. Besides, Table 7.2 also shows the physical properties of this model, and some are basic physical properties, and others are calculated from the basic physical properties.

Table 7.2 Geometric parameters and properties

Symbol	Description	Value	Expression	Reference
W^{IC}	Inlet channel width	$1 \times 10^{-3}\ m$		Lab measured
W^{OC}	Outlet channel width	$1 \times 10^{-3}\ m$		Lab measured
W^{L}	Land width	$2 \times 10^{-3}\ m$		Lab measured
t_g^C	GDL thickness under channels	$3.8 \times 10^{-4}\ m$	$t_{gdl}^{channel} = t_{gdl}^{origin}$	Lab measured
t_m	Membrane thickness	$5.08 \times 10^{-5}\ m$		Lab measured
t_g^L	GDL thickness under land	$2 \times 10^{-4}\ m$	$t_{gdl}^{land} = t_{gasket}$	Lab measured
t_{acl}	Anode catalyst thickness	$1 \times 10^{-5}\ m$		[16]

t_{ccl}	Cathode catalyst thickness	$1 \times 10^{-5}\ m$		[16]
ε_g^c	GDL porosity under channels	0.5		[16]
ε_g^L	GDL porosity under land	0.3		[16]
ε_{cl}^c	Catalyst layer porosity under channels	0.5		[16]
ε_{cl}^L	Catalyst layer porosity under land	0.3		[16]
κ_g^c	GDL permeability under channels	$1.76 \times 10^{-11}\ m^2$		[16]
κ_g^L	GDL permeability under land	$1.76 \times 10^{-11}\ m^2$		[16]
κ_{cl}	Catalyst layer permeability	$1.76 \times 10^{-13}\ m^2$		[16]
σ_g^x	GDL conductivity in x direction	$1250\ S/m$		[94]
σ_g^y	GDL conductivity in y direction	$4000\ S/m$		[95]
σ_m	Membrane conductivity	$17.916\ S/m$	$10.9798e^{\left(1268\left(\frac{1}{303}-\frac{1}{T}\right)\right)}$	[96]
$[Pt]$	Catalyst loading	$0.4mg/cm^2$		Manufacture
$D_{H_2-H_2O}$	H_2 and H_2O binary diffusion coefficient	$1.11 \times 10^{-4}\ m^2/s$	$9.15 \times 10^{-5}\left(\frac{T}{307.1}\right)^{1.75}$	[97]
$D_{N_2-H_2O}$	N_2 and H_2O binary diffusion coefficient	$3.11 \times 10^{-5}\ m^2/s$	$2.56 \times 10^{-5}\left(\frac{T}{307.1}\right)^{1.75}$	[97]
$D_{O_2-N_2}$	O_2 and N_2 binary diffusion coefficient	$2.90 \times 10^{-5}\ m^2/s$	$2.20 \times 10^{-5}\left(\frac{T}{293.2}\right)^{1.75}$	[97]
$D_{O_2-H_2O}$	O_2 and H_2O binary diffusion coefficient	$3.41 \times 10^{-5}\ m^2/s$	$2.82 \times 10^{-5}\left(\frac{T}{308.1}\right)^{1.75}$	[97]
μ^a	Anode viscosity	$9.74 \times 10^{-6}\ Pa \cdot s$		[98, 99]
μ^c	Cathode viscosity	$2.03 \times 10^{-5}\ Pa \cdot s$		[99]
T	Cell temperature	$343.15\ K$		
p^{ref}	Reference pressure	$1.01 \times 10^5 Pa$		[90]
$C_{O_2}^{ref}$	O_2 reference concentration	$40.88\ mol/m^3$		[100]
$C_{H_2}^{ref}$	H_2 reference concentration	$40.88\ mol/m^3$		[100]

p^{sat}	H_2O saturation pressure	$30710Pa$	$log_{10} p^{sat} = -2.1794 + 0.02957T - 9.1837 \times 10^{-5}T^2 + 1.4454 \times 10^{-7}T^3$	[5]
χ_{H_2O}	H_2O mole fraction at anode and cathode	0.30406	p^{sat}/p^{ref}	
χ_{O_2}	O_2 mole fraction at cathode	0.14615	$0.21 \times (1 - \chi_{H_2O})$	
χ_{N_2}	N_2 mole fraction at cathode	0.54980	$0.79 \times (1 - \chi_{H_2O})$	
χ_{H_2}	H_2 mole fraction at anode	0.69594	$1 - \chi_{H_2O}$	
α_a^a	Anodic transfer coefficient of anode	0.5		[101]
α_c^a	Cathodic transfer coefficient of anode	0.5		[101]
α_a^c	Anodic transfer coefficient of cathode	0		[100]
α_c^c	Cathodic transfer coefficient of cathode	1		[100]
j_0^a	Anode exchange current density	$9.10 \frac{A}{m^2}$		[102]
j_0^c	Cathode exchange current density	$6.0 \times 10^{-5} \frac{A}{m^2}$		[103]
ECA^y	Cathode ECA distribution along y direction	$Gaussian\ fitting$		Experiment

Comparing with other models, in this study, the experimental ECA distribution from previous chapter is implemented, which will make this model conditions closer to the real situations. The ECA curve fitting is shown in Fig. 7.4.

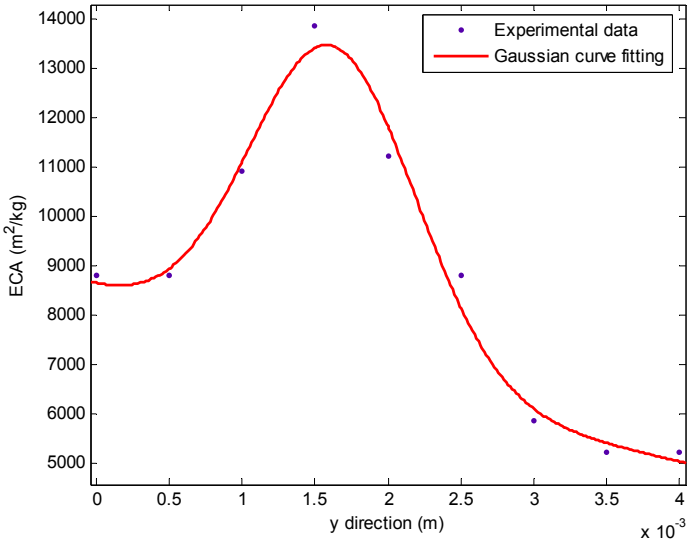

Fig. 7.4 ECA curve fitting of the experimental data

The Gaussian curve fitting equation for ECA distribution is shown as:

$$ECA(y) = a_1 \exp\left[-\left(\frac{y-b_1}{c_1}\right)\right] + a_2 \exp\left[-\left(\frac{y-b_2}{c_2}\right)\right] \tag{7.13}$$

$$\begin{aligned} a_1 &= 6.534 \times 10^3; b_1 = 0.001623; c_1 = 0.0008066; \\ a_2 &= 4.918 \times 10^{18}; b_1 = -0.5193; c_1 = 0.08907 \end{aligned} \tag{7.14}$$

7.6 Computation procedure

In this dissertation, the model is developed in commercial software COMSOL 4.3a. Numerical computation is important to engineering and many types of commercial software have been developed in recent years. COMSOL stands up due to its reliability, flexibility and user friendly [104]. The graphical user interface (GUI) of COMSOL 4.3a is shown in Fig. 7.5.

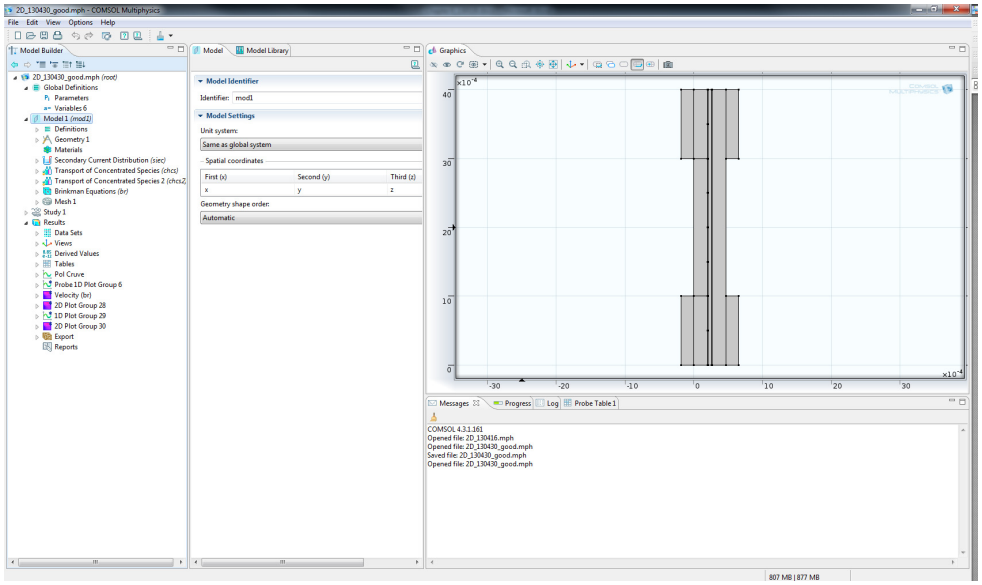

Fig. 7.5 Graphical user interface (GUI) of COMSOL 4.3a

In this dissertation, the computation procedure of the model is illustrated in Fig. 7.6.

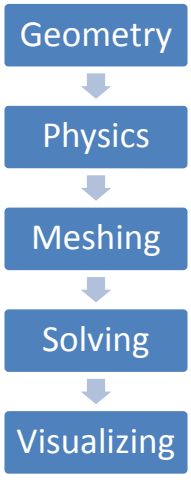

Fig. 7.6 Computation procedure of the model

- Geometry

Geometry contains computation domains, boundaries. Built-in computer aided design (CAD) tool in COMSOL can be used to develop one-dimensional (1D), two-dimensional (2D) and three-dimensional (3D) geometries. The geometry used in COMSOL is shown in Fig. 7.7.

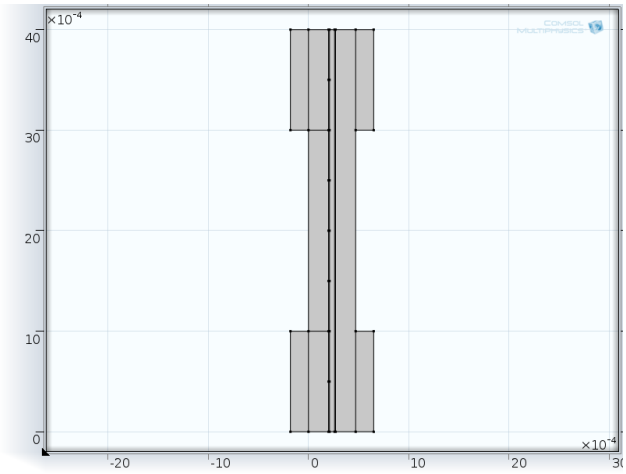

Fig. 7.7 Model geometry in COMSOL

- Physics

COMSOL 4.3a can be used for multiphysics problems. In multiphysics problems, more than one type of physics are coupled together, which makes the solving it analytically difficult. In this model, one software interface can be used to model one single mechanism, and finally, all of them can be integrated.

The secondary current distribution interface is used to model the electrochemical kinetics. Ohms law is applied as governing equation to solve the potential both in solid phase and electrolyte phase. Bulter-Volmer equation is used to calculate the current density.

The transport of concentrated species interface is used to calculate the species concentration via Maxwell-Stefen equation. Mass fraction of all the species can be obtained.

The free and porous media flow interface is used to calculate velocity and pressure. In this model, brinkman equation is considered.

These three interfaces are coupled together as shown in Fig. 7.8. All the three interfaces are coupled with the mass source term. The transport of concentrated species interface is coupled with the free and porous media flow interface via velocity and pressure fields.

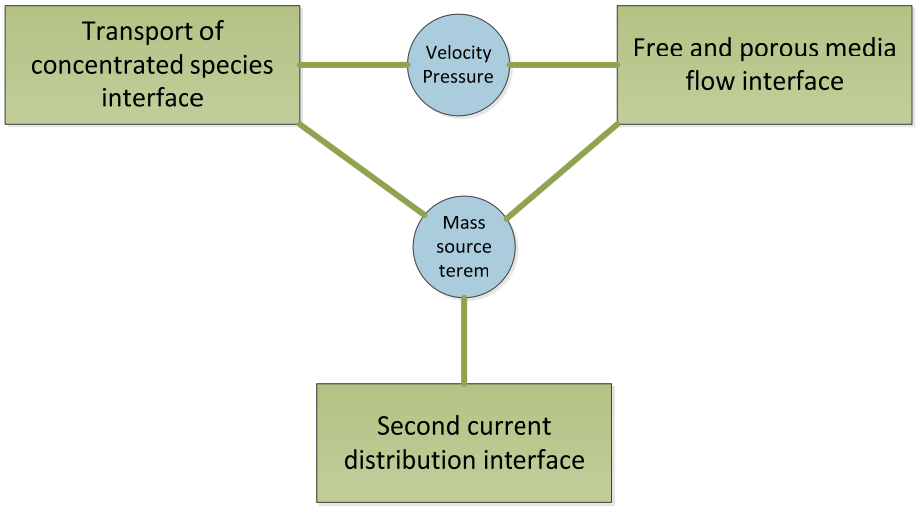

Fig. 7.8 Coupling relations between three physics interfaces

- Meshing

For 2D geometry, COMCOL can discretize the domains into triangular or quadrilateral mesh elements [105]. In this model, a meshing map with non-uniform size is developed. By doing so, the meshing map can be easily modified and controlled. The

catalyst contains the smallest sizes of mesh elements since the electrochemical reactions occur there. One example of the meshing is shown in Fig. 7.9.

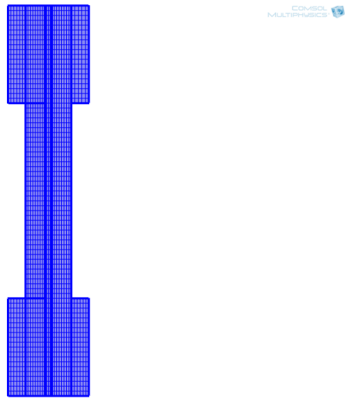

Fig. 7.9 Model meshing in COMSOL

- Solving

COMSOL provides many types of solvers. In this model, stationary segregated solver is chosen. By applying this solver, the model is easier to converge, and also computation time is shorter than fully coupled solver. In each segregated step, multifrontal massively parallel sparse direct solver (MUMPS) is applied.

- Visualization

After computation, results will be stored. It is necessary to plot the results to obtain better understanding. COMSOL provides powerful 1D, 2D and 3D plot to express the final results.

CHAPTER 8

MODELING RESULTS OF CURRENT DISTRIBUTION

8.1 Model validation

This model has been validated in two aspects. First, the mesh element independence check is conducted. The mesh elements in x and y direction have been calculated and compared. The criterion is the velocity profile in x and y direction, which are shown in Fig. 8.1. It is clearly shown that the velocity profile becomes much smooth when the mesh element is increased. Considering the time and accuracy, 66 elements in x direction and 80 elements in y direction are chosen.

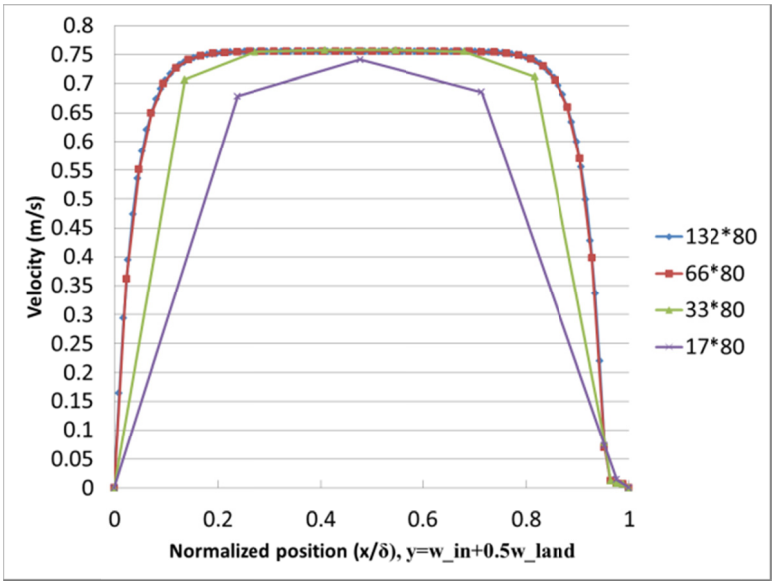

(a)

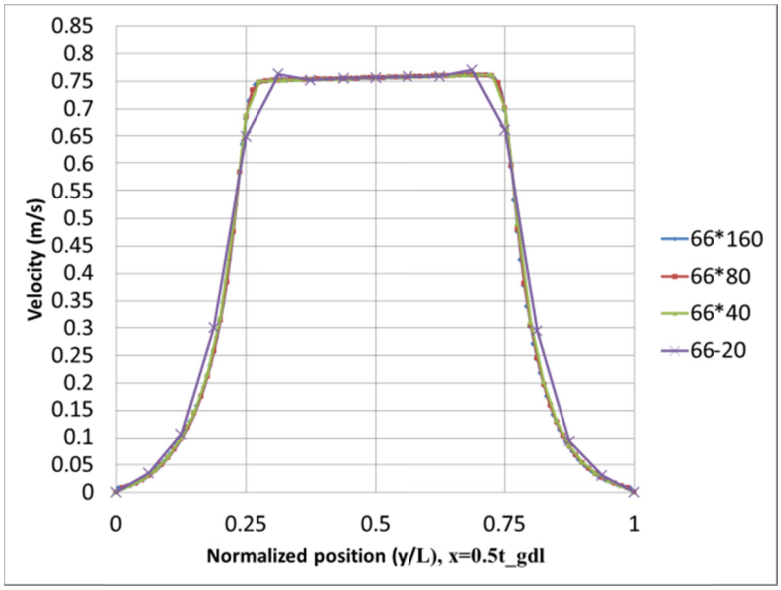

(b)

Fig. 8.1 Mesh element independence check: (a) x direction mesh element; (b) y direction mesh element.

Then, the modeling result is compared with the experimental data as shown in Fig. 8.2. The experiment is conducted under the following major conditions: both anode and cathode flow rates are 600 sccm. Cell temperature is 70 ℃, and both anode and cathode reactant are fully humidified. From Fig. 8.2 (a), it shows that the modeling and experimental stoichiometric number is close to each other. So the modeling conditions are same as the experimental conditions. From Fig. 8.2 (b), it is shown that the model predicts the experiment current density very well in most practical operation voltages.

By these two steps, it is reasonable to state that this model can capture the fundamental mechanism of the fuel cells very well.

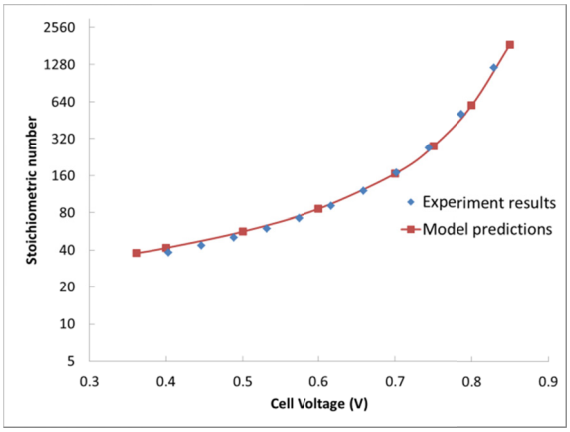

(a)

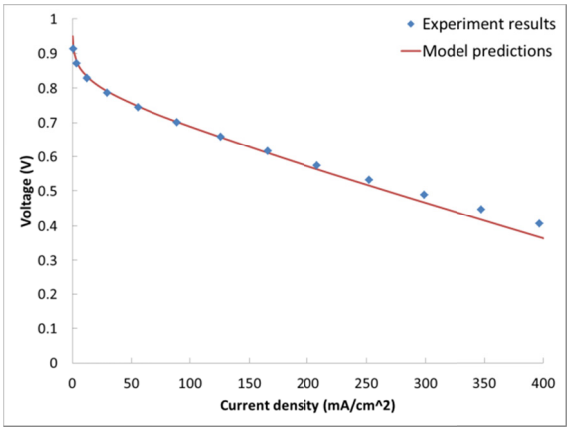

(b)

Fig. 8.2 Experimental results and model predictions comparisons. (a) Stoichiometric number; (b) polarization curves

8.2 Basic distributions

The velocity distribution inside the GDL and catalyst layer is shown in Fig. 8.3. The reactant is impinging onto the catalyst surface under the inlet channel while leaving the catalyst surface under the outlet channel. It is shown that the reactant is more likely to cross the land region by the shortest path, and reactant flows much faster around the land corners of the inlet channel and outlet channel.

At y/W=0.5 (Cell total width W=4 mm), the velocity distribution profile is shown in Fig. 8.4. Highly non-uniform velocity distribution is developed inside the GDL and catalyst layer. The velocity changes little except the regions near the boundaries. The velocity drops very fast at the interfaces of GDL/land and GDL/catalyst, and finally becomes zero at the interfaces of GDL/land and catalyst/membrane due to the non-slip boundaries conditions.

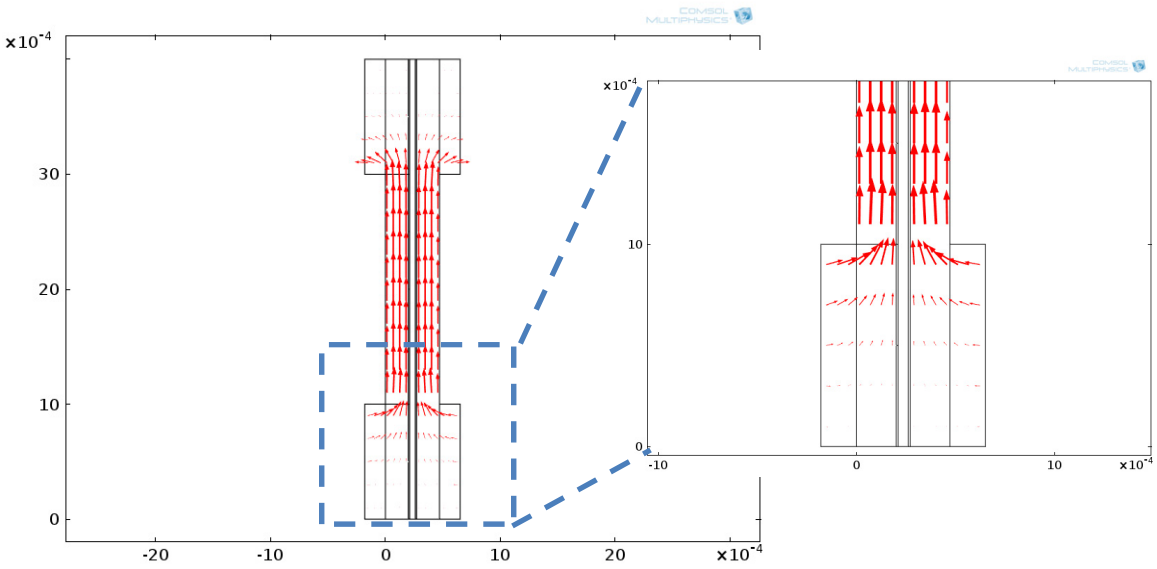

Fig. 8.3 Overall velocity distribution

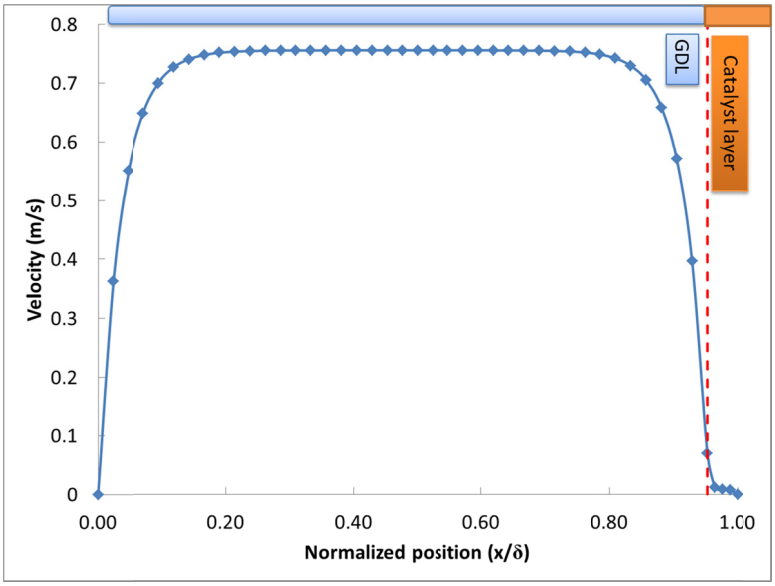

Fig. 8.4 Velocity distribution at y/L=0.5 (Cell total width L=4 mm)

The oxygen and hydrogen molar concentrations are shown in Fig. 8.5. Due to reaction consumption, the reactant is gradually decreasing along the lateral direction, and the concentration in the inlet channel is the highest, and that under the outlet channel is the lowest. However, in this case, only small concentration variations are observed due to the high stoichiometric ratio inlet conditions. If smaller stoichiometric ratio is applied as the inlet conditions, the lateral reactant concentration will be enlarged, and finally, some downstream locations may undergo reactant starvation.

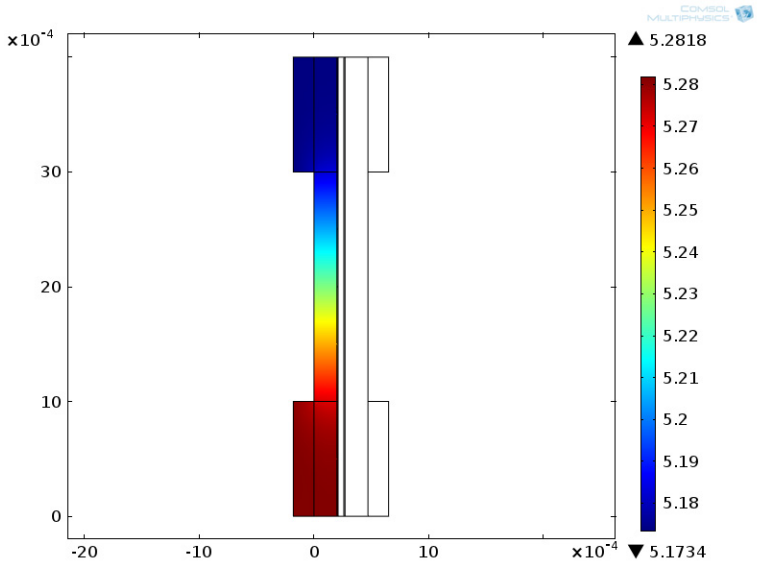

(a)

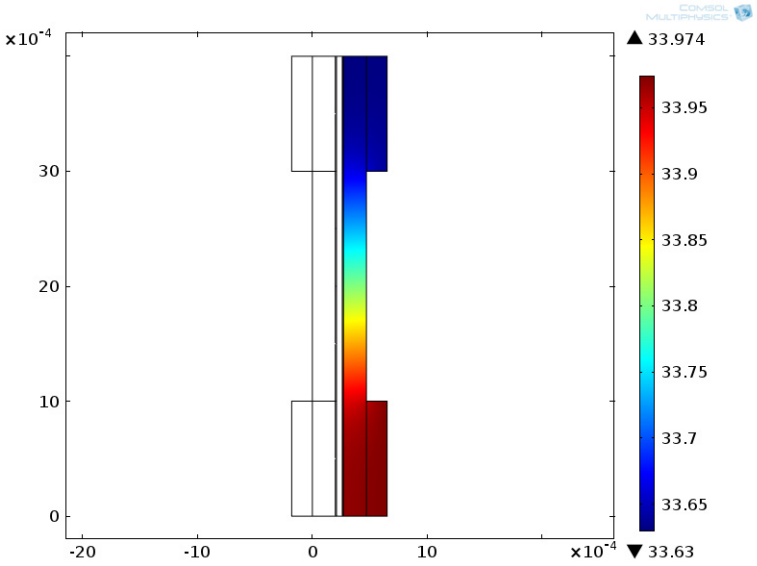

(b)

Fig. 8.5 Reactant molar concentration. (a) Oxygen; (b) hydrogen.

8.3 Lateral current distribution

From experiments, the lateral current density distribution has been obtained by measuring seven different locations as shown in Fig. 8.6. Besides, in the model, the

cathode catalyst has been divided into eight segments as shown in Fig. 8.7. In order to compare the experimental results and modeling prediction under each location, some manipulations are needed as shown in Table 8.1. For example, if the modeling results of current density under P1 location is needed, the current density under Parts In1 and In2 should be averaged. By doing this, the discretized modeling current density distribution can be obtained.

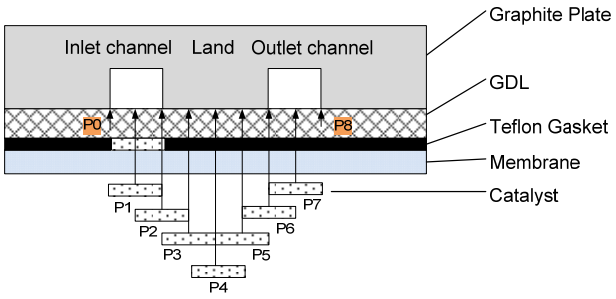

Fig. 8.6 Experimental measuring locations

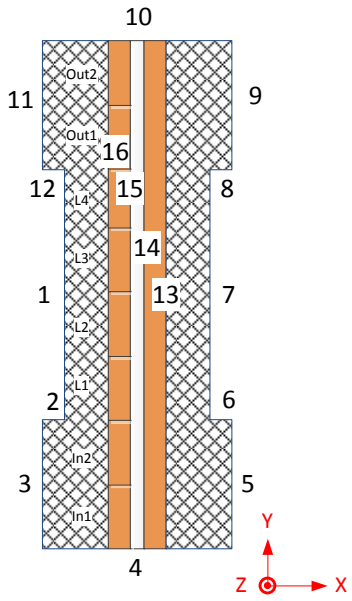

Fig. 8.7 Modeling segments under cathode catalyst layer

Table 8.1 Experimental and modeling equivalent evaluation points

Experimental test points	Modeling equivalent points
P1	Average(In1+In2)
P2	Average (In2+L1)
P3	Average (L1+L2)
P4	Average (L2+L3)
P5	Average (L3+L4)
P6	Average (L4+Out1)
P7	Average (Out1+Out2)

By manipulations stated above, the discretized lateral current densities under the same location with experiments are shown in Fig. 8.8. The continuous lateral current density distribution is shown in Fig. 8.9. These two figures clearly show that after integrating the non-uniform ECA distribution, the lateral current density shows high non-uniform distribution characteristics. The current density under the land is the highest, and the current density under the inlet channel is much higher than that under the outlet channel. This non-uniform lateral current distribution is the combined effect of non-uniform ECA and reactant concentration. Furthermore, by applying constant ECA ($ECA = 1 \times 10^4\ m^2/kg$), the local current density distribution is mainly determined by concentration distribution, which is shown as Fig. 8.10. However, in this case, due to the large stoichiometric ratio inlet conditions, the effect of concentration distribution on the lateral current distribution is not significant.

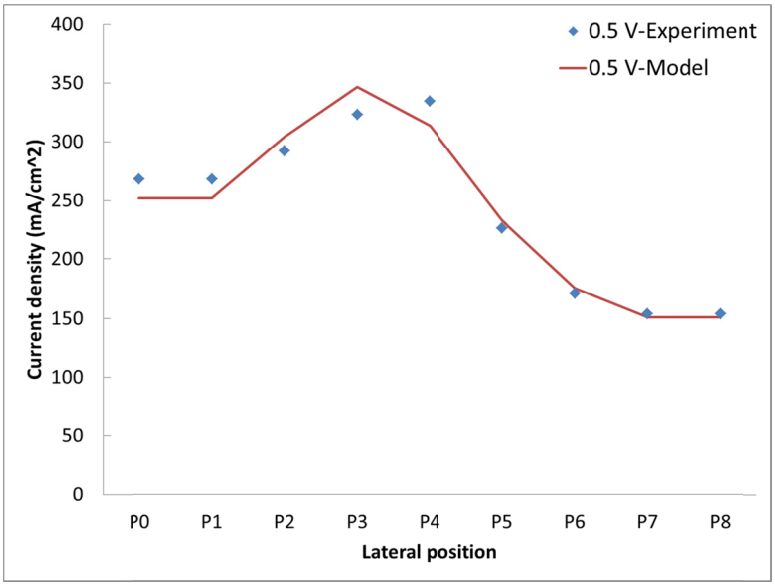

Fig. 8.8 Discrete lateral current density distribution

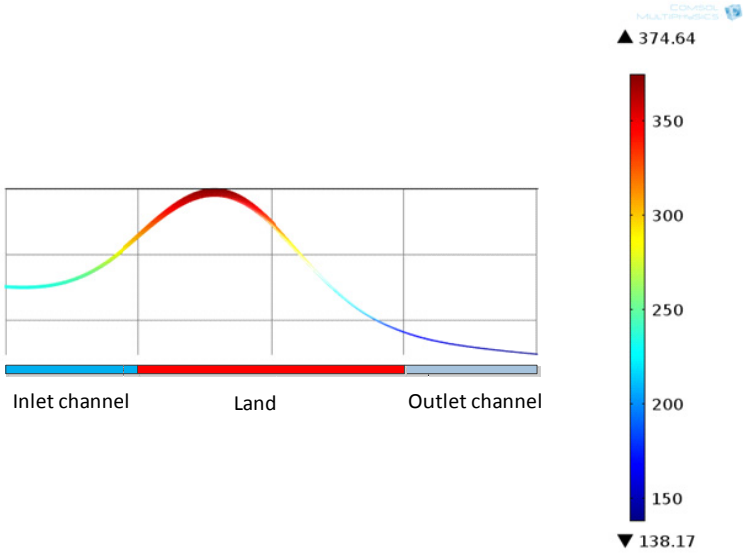

Fig. 8.9 Continuous lateral current density distribution

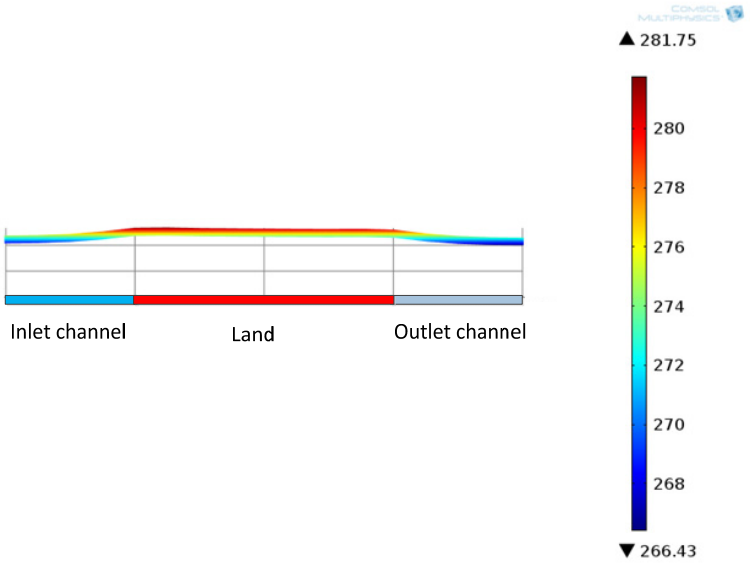

Fig. 8.10 Lateral current density distribution with constant ECA

8.4 Model optimizations

In this study, the ratio of the outlet channel width to the inlet channel width, the land width to the inlet channel width, the GDL thickness to the base GDL thickness are optimized.

For all the optimization cases, the cathode inlet stoichiometric ratios are three, and the cell voltages are 0.5 V. For PEM fuel cell optimizations, it is straight forward to maximize the current density and power density. In addition, for a complete fuel cell system, energy input is required to pump the air and water into the fuel cell, and it is one of the important energy consumption sources for the whole system. So the net power density is also one of the important indexes for PEM fuel cell system optimization, which is calculated by the following equation:

$$P_{net} = \frac{JE - \frac{Q \cdot \Delta p}{\eta_p}}{A} \tag{8.1}$$

Where P_{net} is the net power density (W/cm^2), J is the current (A), E is the cell voltage (V), Q is the inlet flow rate (m^3/s), Δp is the pressure difference (Pa), η_p is the air pump efficiency (0.85), A is the fuel cell area (cm^2).

In this study, the main objective is to obtain the maximal net power density.

8.4.1 Outlet channel width/inlet channel width

In this case, the outlet/inlet channel width ratio is optimized when land width is kept as 1mm. From Fig. 8.11, it is shown that a smaller outlet channel width can lead to a higher current density and power density, consistently for three different inlet channel widths. Due to the smaller ECA under the outlet channel, smaller outlet channel can increase the averaged total current density. Besides that, one can observe that the 1 mm inlet channel is preferred among the three types of inlet channel width.

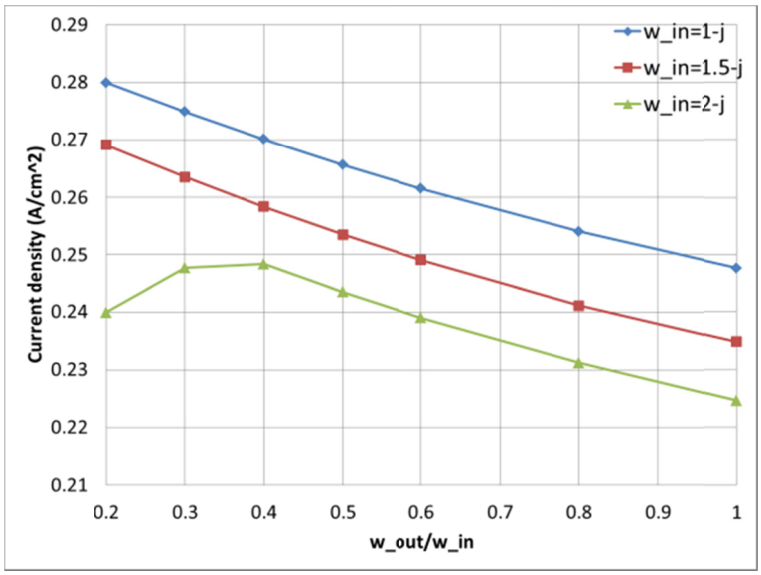

(a)

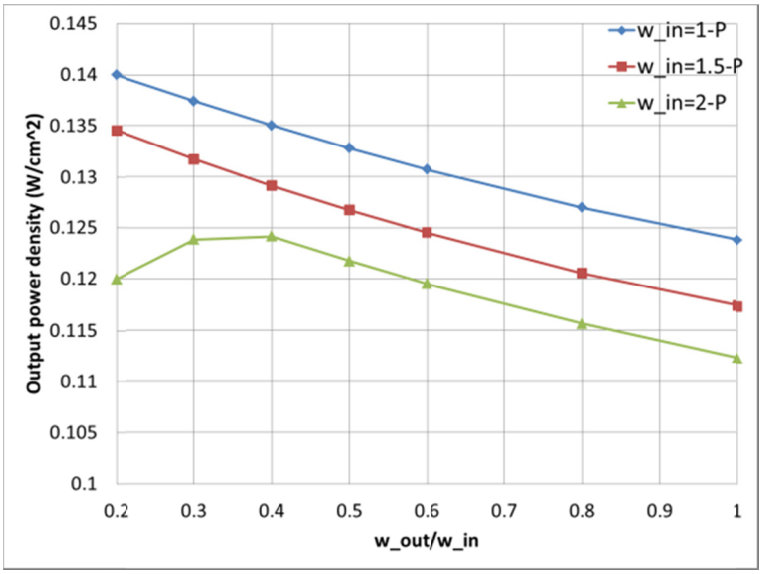

(b)

Fig. 8.11 Outlet/inlet channel width optimization (Land width=1mm): (a) current density; (b) power density.

The net power density is shown in Fig. 8.12. In this case, the optimization results stay the same with or without consideration of the pumping power consumed. Although smaller outlet channel widths can lead to larger pumping power consumption, still, a smaller outlet channel width can lead to a higher net power density.

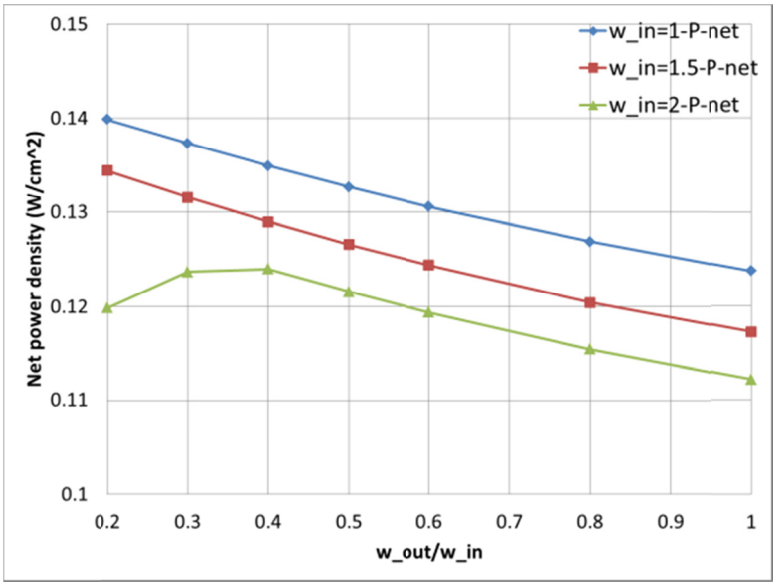

Fig. 8.12 Outlet/inlet channel width optimization (Land width=1mm): net power density comparison.

The current densities and net power densities for each inlet channel width are shown in Fig. 8.13.

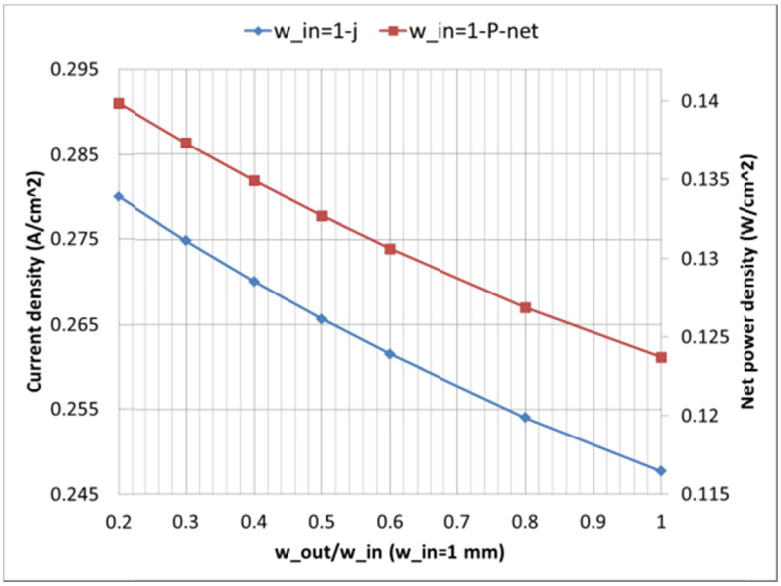

(a)

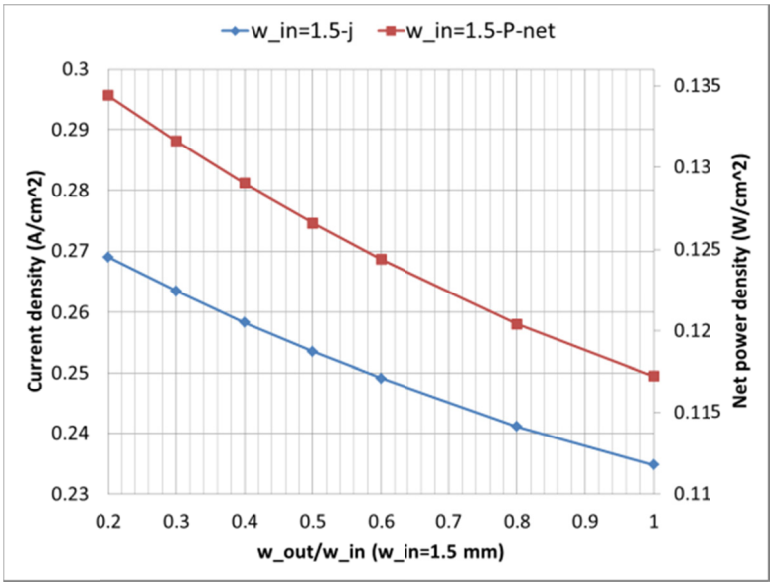

(b)

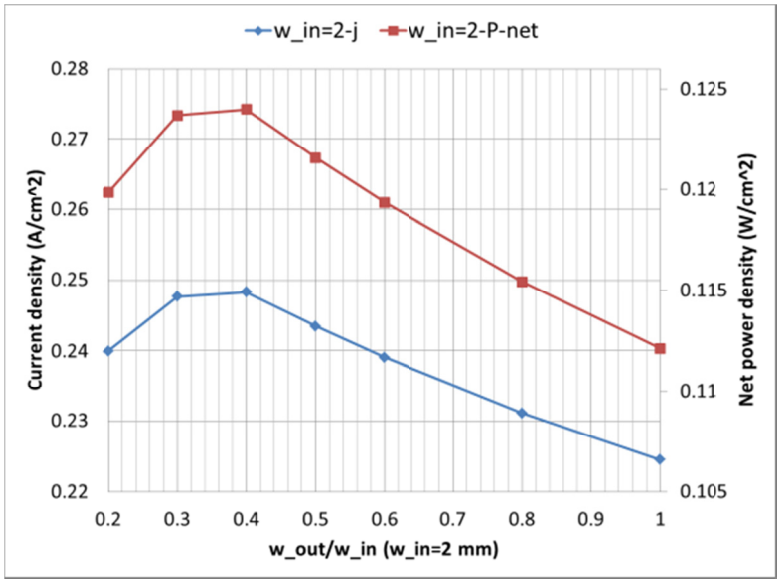

(c)

Fig. 8.13 Outlet/inlet channel width optimization (Land width=1mm): (a) inlet channel width=1mm; (b) inlet channel width=1.5mm; (c) inlet channel width=2mm.

8.4.2 Land/inlet channel width

In this case, the land/inlet channel width ratio is optimized when outlet channel width is kept as 1mm. From Fig. 8.14, it is shown that a larger land width can lead to a higher current density and power density for three different inlet channel widths. Due to the larger ECA under the land, larger land is preferred. One should notice that at the same land/inlet channel width ratios, larger inlet channel width will lead to larger land width, which is the reason of the larger current density for the wider inlet channel.

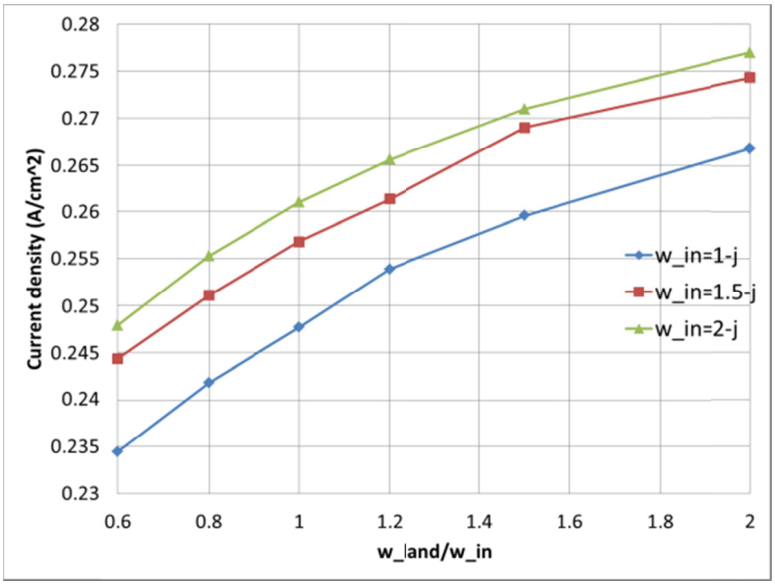

(a)

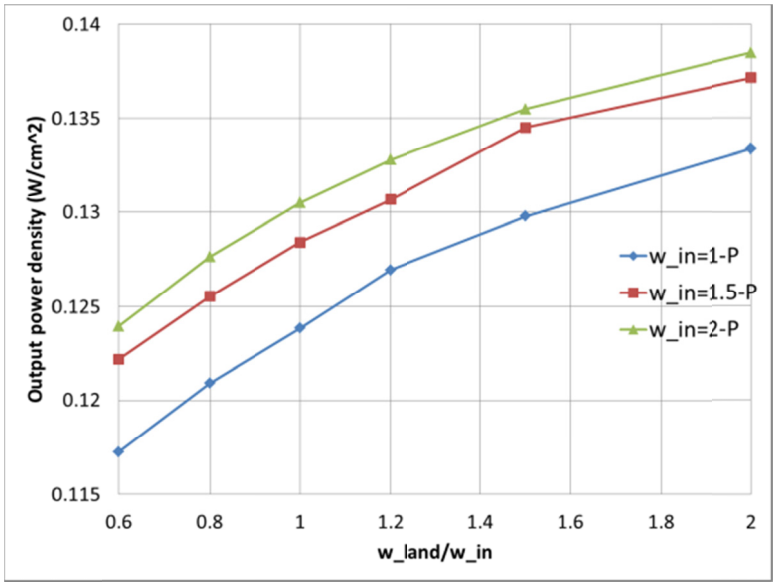

(b)

Fig. 8.14 Land/inlet channel width optimization (Outlet channel width=1mm): (a) current density; (b) power density.

The net power density is shown in Fig. 8.15. It is clearly shown that a larger land width can lead to a higher net power density.

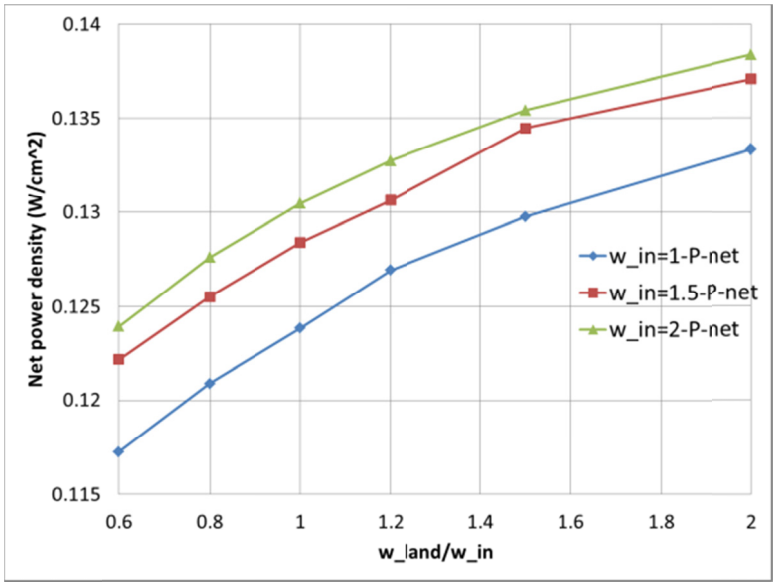

Fig. 8.15 Land/inlet channel width optimization (Outlet width=1mm): net power density comparison.

The current densities and net power densities for each inlet channel width are shown in Fig. 8.16.

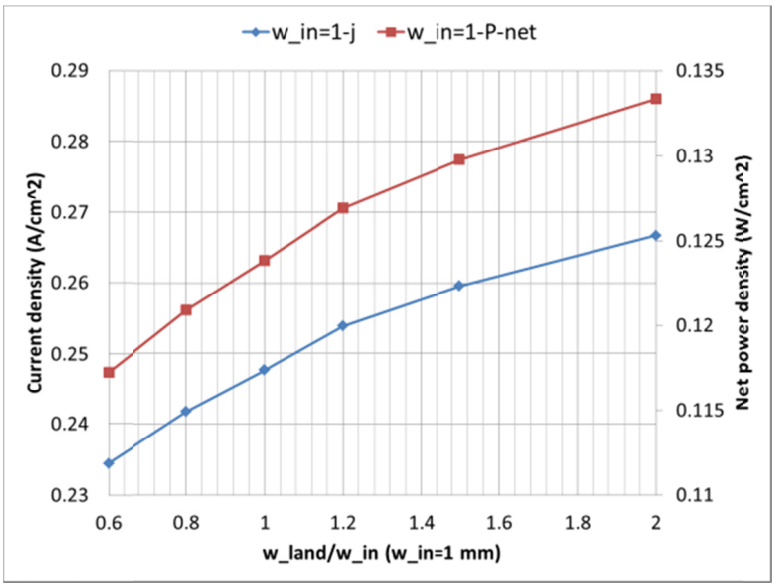

(a)

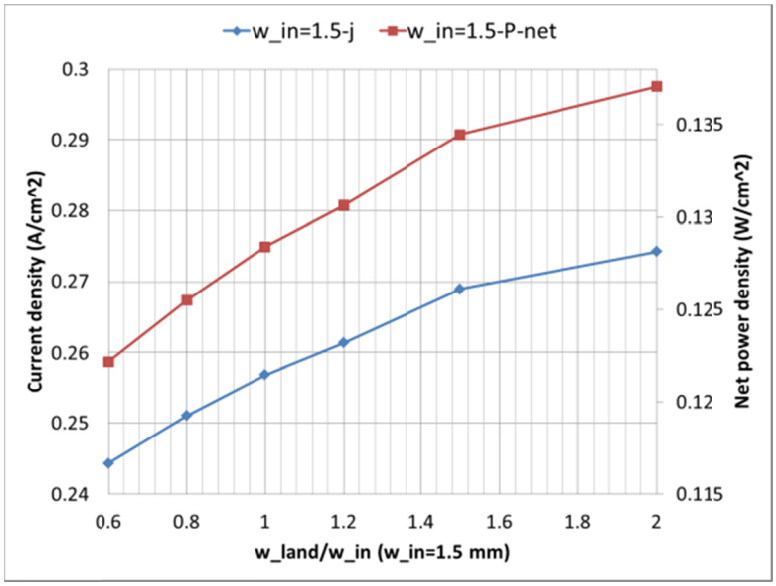

(b)

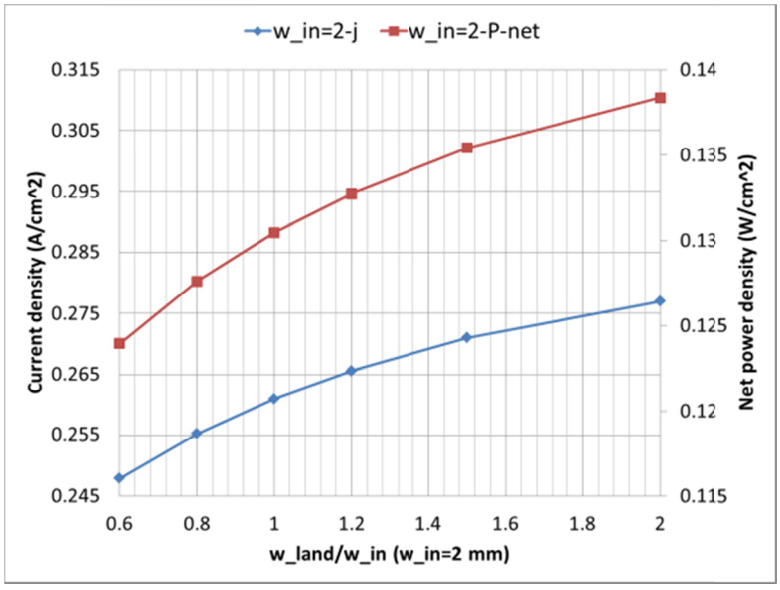

(c)

Fig. 8.16 Land/inlet channel width optimization (Outlet width=1mm): (a) inlet channel width=1mm; (b) inlet channel width=1.5mm; (c) inlet channel width=2mm.

8.4.3 GDL thickness

During the calculations in this case, the inlet channel, the land and the outlet channel widths are kept as 1 mm. GDL thickness under the land can be different due to different compression forces, different gasket thickness assembled, and it will affect the pressure drop between two channels, the cross flow velocity and reactant diffusion.

In order to view the tendency clearly, three PEM fuel cells with representative dimensions are used in this case, which are shown in Table 8.2.

Table 8.2 Three representative cell dimensions for GDL thickness optimizations

Dimensions (mm)	Inlet channel	Land	Outlet channel
Cell A	1	1	1
Cell B	1	2	1
Cell C	1	2	0.2

From Fig. 8.17, it is shown that for different GDL thickness, no significant change is observed for the current density and power density.

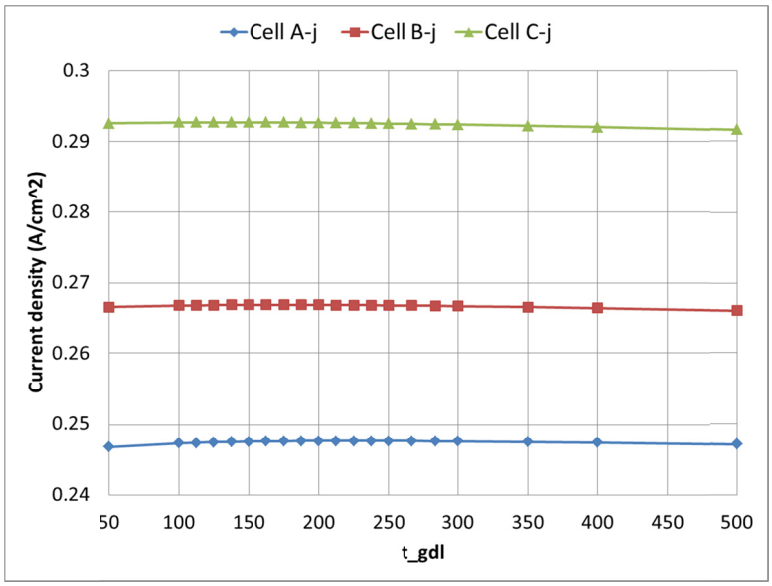

(a)

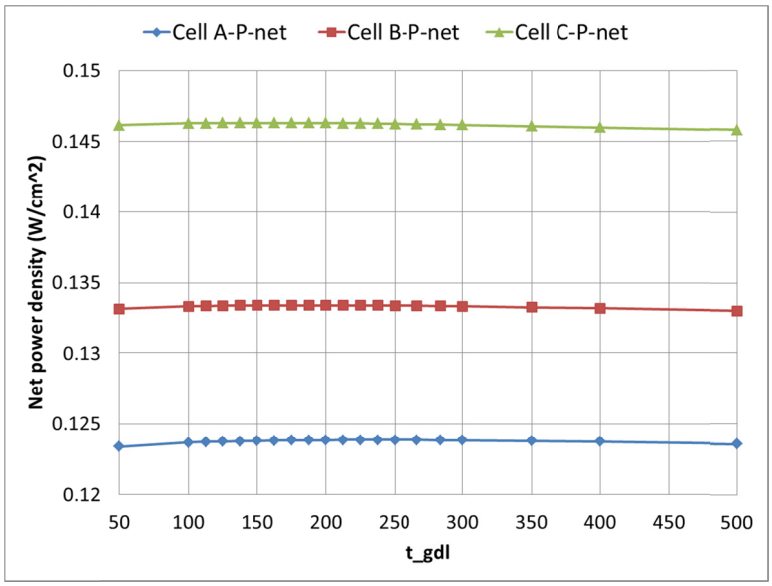

(b)

Fig. 8.17 GDL/base GDL thickness optimization (Inlet channel=land=Outlet channel width=1mm): (a) current density; (b) power density.

The net power density is shown in Fig. 8.18. It is clearly shown that the net power density changes little.

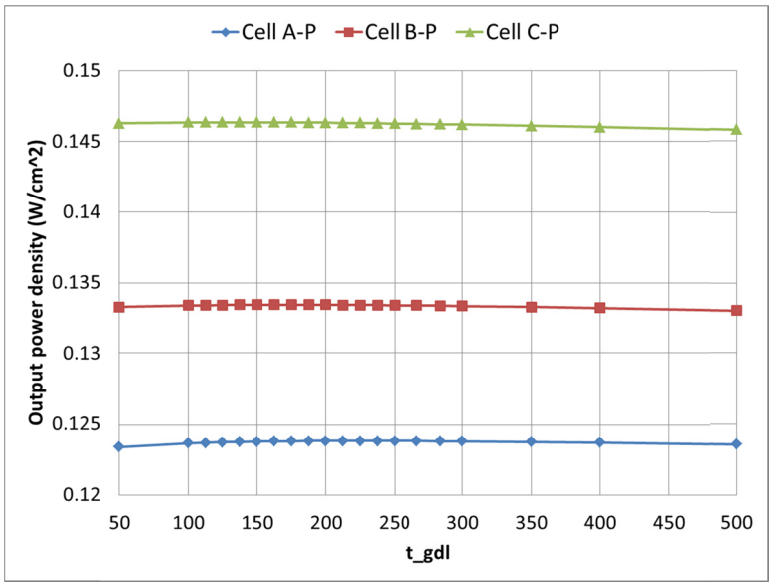

Fig. 8.18 GDL/base GDL thickness optimization (Inlet channel=land=Outlet channel width=1mm): net power density comparison.

The current densities and net power densities for each inlet channel width are shown in Fig. 8.19. Although from Fig. 8.18, the net power density changes little due to the scale, however, From Fig. 8.19, if comparing the current density and net power density for each cell separately, similar tendency still can be observed. The optimal GDL thickness for each cell is shown as in Table 8.3. If compare Cell A and Cell B, it is shown that thinner GDL is preferred for the fuel cells with wider land. Similarly, if compare Cell B and Cell C, it is also shown that thinner GDL is essential to obtain higher net power density for fuel cells with narrower outlet channels.

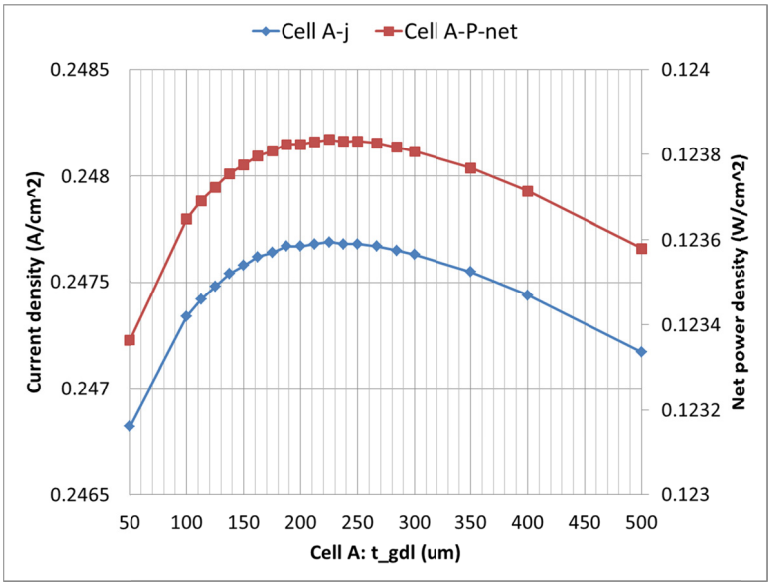
Cell A-j
Cell A-P-net
0.2485
0.248
0.2475
0.247
0.2465
0.124
0.1238
0.1236
0.1234
0.1232
0.123
Current density (A/cm^2)
Net power density (W/cm^2)
50
100
150
200
250
300
350
400
450
500
Cell A: t_gdl (um)

(a)

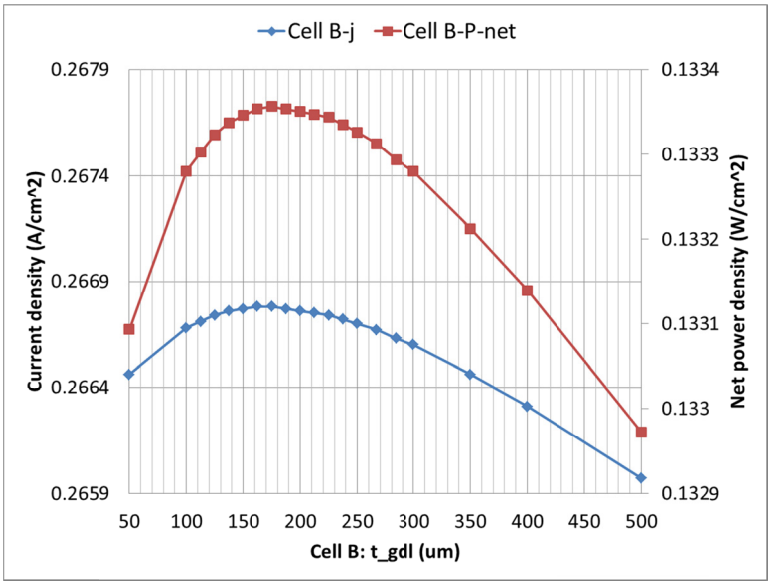
Cell B-j
Cell B-P-net
0.2679
0.2674
0.2669
0.2664
0.2659
0.1334
0.1333
0.1332
0.1331
0.133
0.1329
Current density (A/cm^2)
Net power density (W/cm^2)
50
100
150
200
250
300
350
400
450
500
Cell B: t_gdl (um)

(b)

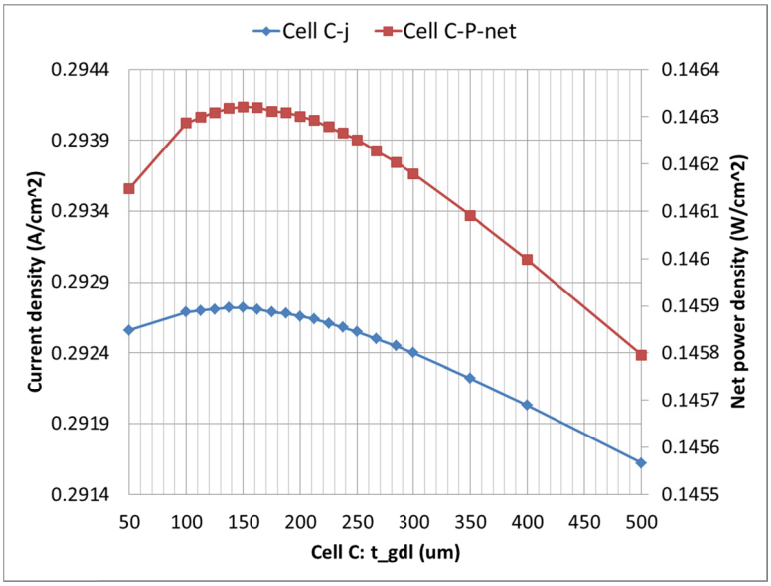

(c)

Fig. 8.19 GDL/base GDL thickness optimization (Inlet channel=land=Outlet channel width=1mm): (a) inlet channel width=1mm; (b) inlet channel width=1.5mm; (c) inlet channel width=2mm.

Table 8.3 Optimal GDL thickness for each cell

Dimensions (mm)	Inlet channel	Land	Outlet channel	Optimum(μm)
Cell A	1	1	1	225
Cell B	1	2	1	175
Cell C	1	2	0.2	150

8.5 Summary

A two-dimensional PEM fuel cell model is developed by COMSOL software to study the lateral current distribution in interdigitated flow field. Comparing with previous models, non-uniform ECA distribution is integrated into this model, and the modeling predictions agree with the experimental data very well. The modeling results show that the lateral current distribution in interdigitated flow field is not uniform, and the current under the land is the highest, and the current under the outlet channel is much lower than that under the inlet channel.

The dimensions of the interdigitated flow field are also investigated in order to maximize the power density and net power density. The modeling results reveal that narrower outlet channel and wider land is preferred in interdigitated flow field. Besides that, it also shows that for fuel cells with wider lands and narrower outlet channels, thinner GDL is essential to enhance the net power density.

CHAPTER 9

CONCLUSIONS AND SUGGESTIONS FOR FURTHER RESEARCH

9.1 Conclusions

In this dissertation, a comprehensive study has been conducted on the lateral current density variation of PEM fuel cells with interdigitated flow fields. Specifically, in order to determine the lateral current distribution in interdigitated flow field, both experimental and modeling work has been carried out systematically.

In the experimental study, in-house partially-catalyzed membrane electrolyte assembly (MEA) method was utilized to measure the current density variations in the channel-land direction. Firstly, separate current densities under the inlet channel, the land and the outlet channel were measured directly. Then, the local current densities under these three different locations were also measured under different cathode flow rates, cathode back pressures and cathode humidification temperatures, to study if these operation conditions affect the variation pattern of local current densities. Furthermore, in order to obtain the lateral current density distribution in higher resolution, experiments were conducted by further refining the MEAs under channels and land, which in this study, seven MEAs under different locations were implemented. Finally, cyclic voltammetry (CV) and electrochemical impedance spectroscopy (EIS) methods were used to investigate the underlying causes of the lateral current density variations.

Based on the experimental study, the following conclusions can be drawn.

- The lateral current density is not uniformly distributed in interdigitated flow fields for PEM fuel cells. Current density under the outlet channel is much

lower than that under the inlet channel mainly due to the difference in the angles formed by the velocity vector and the mass flux vector. Current density under the land is higher than that under the inlet channel in the high cell voltage region (>0.4V in this study) and lower in the low cell voltage region (<0.4V in this study).

- Cathode flow rate does not affect the pattern of relative magnitudes of local current densities among the three different areas.
- Cathode back pressure does not affect the pattern of relative magnitudes of local current densities among the three different areas.
- The humidification temperature affects the local current density in different patterns. The current density under the inlet channel decreases significantly due to the lower local water content.
- The ECA is found to play a significant role in determining the current distribution. The ECA under the land is the highest due to the direct compression. The ECA under the inlet channel is much higher than that under the outlet channel.
- The cathode charge transfer resistance results are consistent with the ECA results. The cathode charge transfer resistance under the land is the smallest, while the resistances under the two channels are close to each other.

In addition to the experimental study, a two-dimensional model was developed in order to undermine the physics of electrochemical kinetics, mass transport and momentum of PEM fuel cells. Comparing with previous modeling studies, this model integrated the non-uniform experimental ECA distribution in order to obtain a better

understanding of the lateral current distribution. Besides, the effects of land width, outlet channel width and the under land gas diffusion layer (GDL) thickness were studied to obtain the maximal net power density of PEM fuel cells system.

Based on the modeling work, the following conclusions can be obtained.

- This non-uniform ECA integrated model captures the experimental results very well. Comparing with the constant ECA integrated model, this modeling condition is closer to the practical situations.
- A narrower outlet channel is beneficial to the power density. Although a narrower outlet channel will increase the input pumping power, it is still preferred in order to maximize the net power density.
- A wider land can improve the power density. Although a wider land will increase the pressure drop significantly, the net power density drop due to the increased input pumping power is overwhelmed by the net power density enhancement due to the large incremental ECA under the land.
- For fuel cells with wider lands and narrower outlet channels, thinner GDL is suggested to enhance the net power density.

Overall, the experimental and modeling studies have presented methods to measure the current distribution in channel-land direction, to study the local current change under different operation conditions, to undermine the underlying reasons for lateral current variations, and finally proposed optimal designs for interdigitated flow field in order to improve the net power density.

9.2 Suggestions for further research

Based on this work, the following suggestions for future work can be summarized:

- Conduct a comprehensive mechanism study on the local *in situ* ECA measurement. First, investigate the effects of CV test conditions, especially the zero and non-zero nitrogen flow rates, on the ECA results. In addition, measure the ECA distribution of a MEA, which is either assembled inside PEM fuel cells or disassembled from PEM fuel cells.
- Study the *in situ* catalyst utilization variation regarding to different locations in the flow field, and local operation conditions.
- Optimize the interdigitated flow field dimensions by three-dimensional models. Finally, conduct experiments to prove the modeling results.
- Design novel flow fields by both model and experiment. The core guidance of designing a novel flow field is to increase the land area, decrease the outlet channel area and maintain higher under land cross flow.

The extreme case of maximizing the land area is shown as in Fig. 9.1. In this case, no conventional flow field is used; instead, porous media is used as flow distributor. In order to prevent gas leakage, the thickness of the porous media is suggested larger than the depth of the frame shell. The porous media will be compressed into the frame after the fuel cell assembled. Besides, the mobile compression plate shown in Fig. 9.1 (a) is served as both current collector and direct compression land. Moreover, the compression force is controllable, which is accomplished by the compression screw as shown in Fig. 9.1 (b).

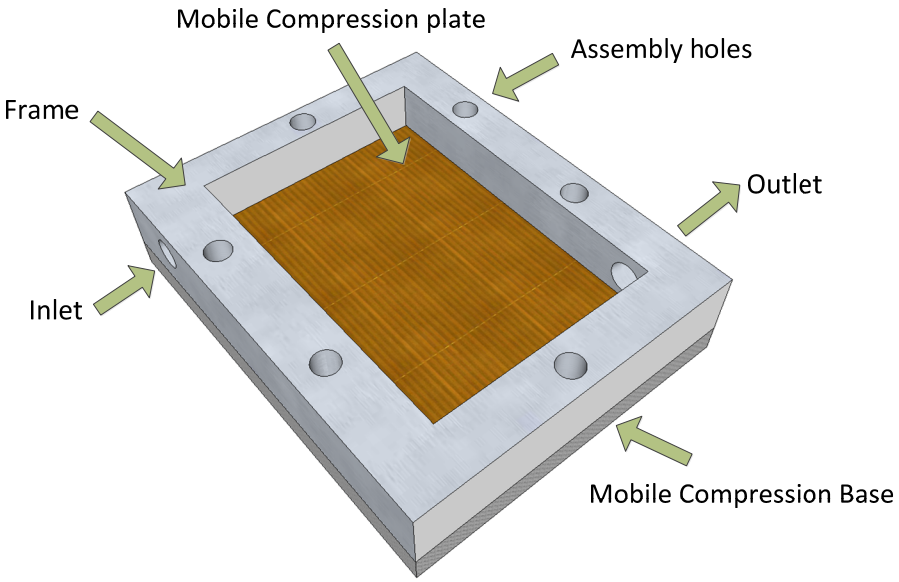
Mobile Compression plate
Assembly holes
Frame
Outlet
Inlet
Mobile Compression Base

(a)

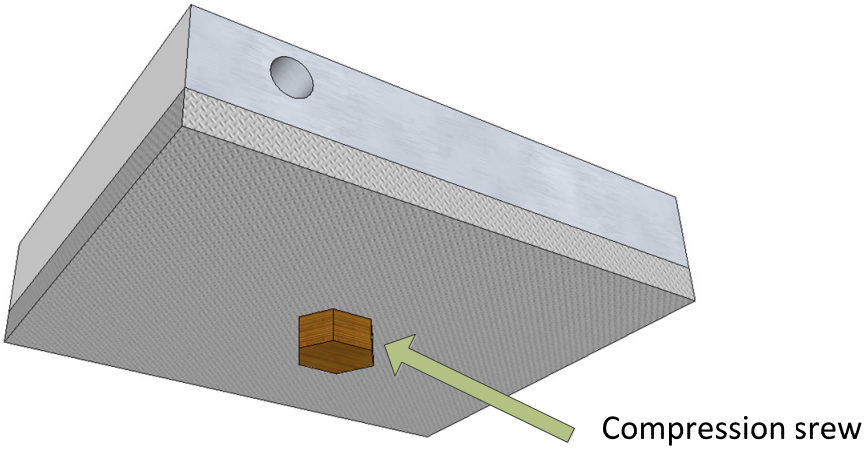
Compression srew

(b)

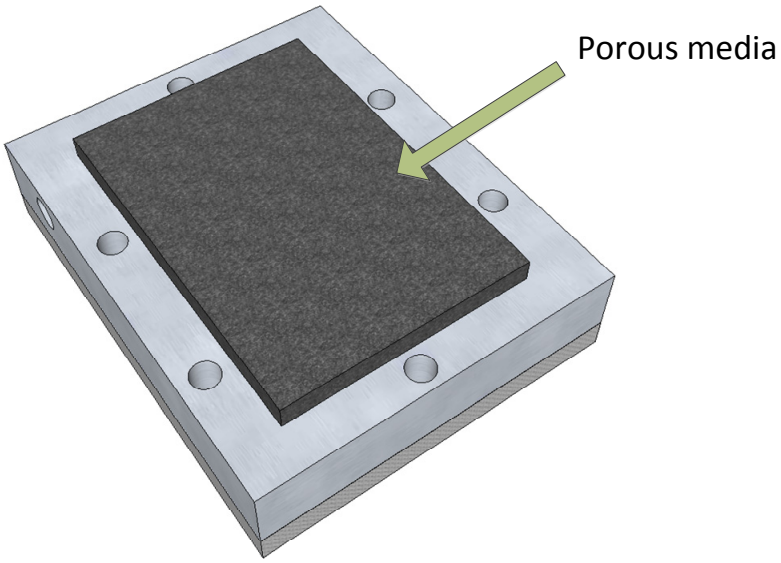

(c)

Fig. 9.1 Mobile compression fuel cell with porous media as flow distributor. (a) Compression frame; (b) compression screw; (c) compression frame with porous media

REFERENCES

[1] Wang L, Liu H. Separate measurement of current density under the channel and the shoulder in PEM fuel cells. J Power Sources. 2008;180:365-72.

[2] Higier A, Liu H. Direct measurement of current density under the land and channel in a PEM fuel cell with serpentine flow fields. J Power Sources. 2009;193:639-48.

[3] U.S. Energy Information Administration. Annual energy review 2011.

[4] Larminie J, Dicks A. Fuel cell systems explained (Second edition) 2003.

[5] O'hayre R, Cha S-W, Colella W, Prinz F. B. Fuel cell fundamentals. 2009.

[6] Taira H. "Under-land Convection in a PEM Fuel Cell" (2012). Open Access Dissertations. Paper 819. 2012.

[7] FuelCellToday. The fuel cell industry review 2012.

[8] Wang Y, Chen KS, Mishler J, Cho SC, Adroher XC. A review of polymer electrolyte membrane fuel cells: Technology, applications, and needs on fundamental research. Appl Energy. 2011;88:981-1007.

[9] James BD, Kalinoski JA. Mass production cost estimation for direct H_2 PEM fuel cell systems for automotive applications: 2008 Update. Contract No. GS-10F-0099J

[10] Papageorgopoulos D. An introduction to the 2010 fuel cell pre-solicitation workshop.

[11] Schmittinger W, Vahidi A. A review of the main parameters influencing long-term performance and durability of PEM fuel cells. J Power Sources. 2008;180:1-14.

[12] Rorup R, et al. Scientific aspects of polymer electrolyte fuel cell durability and degradation. Chem. Rev. 2007, 107, 3904-3951

[13] Wu J, Yuan XZ, Wang H, Blanco M, Martin JJ, Zhang J. Diagnostic tools in PEM fuel cell research: Part I Electrochemical techniques. Int J Hydrogen Energ. 2008;33:1735-46.

[14] Pilatowsky I, Romero RJ, Isaza CA, Gamboa SA, Sebastian PJ, Rivera W. Cogeneration fuel cell-sorption air conditioning systems. 2011:25-36.

[15] Jung CY, Kim WJ, Yi SC. Computational analysis of mixed potential effect in proton exchange membrane fuel cells. Int J Hydrogen Energ. 2012;37:7654-68.

[16] Taira H, Liu HT. Numerical analysis of the cross-flow under the land in a serpentine flow field of a pem fuel cell. Proceedings of the International Mechanical Engineering Congress & Exposition, IMECE2011, November 11-17, 2011, Denver, Colorado, USA.

[17] El-kharouf A, Mason TJ, Brett DJL, Pollet BG. Ex-situ characterisation of gas diffusion layers for proton exchange membrane fuel cells. J Power Sources. 2012;218:393-404.

[18] Cleghorn SJC, Derouin CR, Wilson MS, Gottesfeld S. A printed circuit board approach to measuring current distribution in a fuel cell. J Appl Electrochem. 1998;28:663-72.

[19] Brett DJL, Atkins S, Brandon NP, Vesovic V, Vasileiadis N, Kucernak AR. Measurement of the current distribution along a single flow channel of a solid polymer fuel cell. Electrochem Commun. 2001;3:628-32.

[20] Stumper J, Campbell SA, Wilkinson DP, Johnson MC, Davis M. In-situ methods for the determination of current distributions in PEM fuel cells. Electrochim Acta. 1998;43:3773-83.

[21] Liu ZX, Mao ZQ, Wu B, Wang LS, Schmidt VM. Current density distribution in PEFC. J Power Sources. 2005;141:205-10.

[22] Noponen M, Mennola T, Mikkola M, Hottinen T, Lund P. Measurement of current distribution in a free-breathing PEMFC. J Power Sources. 2002;106:304-12.

[23] Wilkinson M, Blanco M, Gu E, Martin JJ, Wilkinson DP, Zhang JJ, et al. In situ experimental technique for measurement of temperature and current distribution in proton exchange membrane fuel cells. Electrochem Solid-State Lett. 2006;9:A507.

[24] Wieser CH, Helmbold A, Gülzow E. A new technique for two-dimensional current distribution measurements in electrochemical cells. J Appl Electrochem. 2000;30:803-7.

[25] Geiger AB, Eckl R, Wokaun A, Scherer GG. An approach to measuring locally resolved currents in polymer electrolyte fuel cells. J Electrochem Soc. 2004;151:A394.

[26] Sun H, Zhang GS, Guo LJ, Liu HT. A novel technique for measuring current distributions in PEM fuel cells. J Power Sources. 2006;158:326-32.

[27] Freunberger SA, Reum M, Evertz J, Wokaun A, Büchi FN. Measuring the current distribution in PEFCs with sub-millimeter resolution. J Electrochem Soc. 2006;153:A2158.

[28] Freunberger SA, Reum M, Wokaun A, Büchi FN. Expanding current distribution measurement in PEFCs to sub-millimeter resolution. Electrochem Commun. 2006;8:1435-8.

[29] Higier A, Liu HT. Separate in situ measurements of ECA under land and channel in PEM fuel cells. J Power Sources. 2012;215:11-7.

[30] Kazim A, Liu HT, Forges P. Modelling of performance of PEM fuel cells with conventional and interdigitated flow fields. J Appl Electrochem. 1999;29:1409-16.

[31] He WS, Yi JS, Nguyen TV. Two-phase flow model of the cathode of PEM fuel cells using interdigitated flow fields. Materials, Interfaces, and Electrochemical Phenomena. 2000;46:2053-64.

[32] Liu XL, Tan YW, Tao WQ, He YL. A hybrid model of cathode of PEM fuel cell using the interdigitated gas distributor. Int J Hydrogen Energ. 2006;31:379-89.

[33] Um S, Wang CY. Three-dimensional analysis of transport and electrochemical reactions in polymer electrolyte fuel cells. J Power Sources. 2004;125:40-51.

[34] Hu G, Fan JR, Chen S, Liu YJ, Cen K. Three-dimensional numerical analysis of proton exchange membrane fuel cells (PEMFCs) with conventional and interdigitated flow fields. J Power Sources. 2004;136:1-9.

[35] Yi JS, Nguyen TV. Multicomponent transport in porous electrodes of proton exchange membrane fuel cells using the interdigitated gas distributors. J Electrochem Soc. 1999;146:28-45.

[36] Weng FB, Su A, Jung GB, Chiu YC, Chan SH. Numerical prediction of concentration and current distributions in PEMFC. J Power Sources. 2005;145:546-54.

[37] Shyam Prasad KB, Maharudrayya SJ. Flow maldistribution in interdigitated channels used in PEM fuel cells. J Power Sources. 2006;159:595-604.

[38] Chen L, Luan HB, He YL, Tao WQ. Pore-scale flow and mass transport in gas diffusion layer of proton exchange membrane fuel cell with interdigitated flow fields. Int J Therm Sci. 2012;51:132-44.

[39] Wang L, Liu HT. Performance studies of PEM fuel cells with interdigitated flow fields. J Power Sources. 2004;134:185-96.

[40] Guvelioglu GH, Stenger HG. Flow rate and humidification effects on a PEM fuel cell performance and operation. J Power Sources. 2007;163:882-91.

[41] Ding YL, Bi XT, Wilkinson DP. 3D simulations of the impact of two-phase flow on PEM fuel cell performance. Chemical Engineering Science. 2012.

[42] Boyer C, Gamburzey S, Appleby AJ. Evaluation of methods to increase the oxygen partial pressure in PEM fuel cells. J Appl Electrochem. 1999;29:1095-102.

[43] Sadiq Al-baghdadi MAR, Shahad Al-janabi HAK. Effect of operating parameters on the hygro–thermal stresses in proton exchange membranes of fuel cells. Int J Hydrogen Energ. 2007;32:4510-22.

[44] Maddirala VK, Subramanian VR. An approximate closed form solution for pressure and velocity distribution in the cathode chamber of a PEM fuel cell. J Power Sources. 2005;143:173-8.

[45] Saleh MM, Okajima T, Hayase M, Kitamura F, Ohsaka T. Exploring the effects of symmetrical and asymmetrical relative humidity on the performance of H2/air PEM fuel cell at different temperatures. J Power Sources. 2007;164:503-9.

[46] Zhang J, Tang Y, Song C, Cheng X, Zhang J, Wang H. PEM fuel cells operated at 0% relative humidity in the temperature range of 23–120°C. Electrochim Acta. 2007;52:5095-101.

[47] Song CJ, Chua CJ, Tang YH, Zhang JL, Li J, Wang K, et al. Voltage jump during polarization of a PEM fuel cell operated at low relative humidities. Int J Hydrogen Energ. 2008;33:2802-7.

[48] Huang BT, Chatillon Y, Bonnet C, Lapicque F, Leclerc S, Hinaje M, et al. Experimental investigation of air relative humidity (RH) cycling tests on MEA/cell aging in PEMFC Part II: study of low RH cycling test with air RH at 62%/0%. Fuel Cells. 2012;12:347-55.

[49] Natarajan D, Nguyen TV. Current distribution in PEM fuel cells. Part 2: Air operation and temperature effect. Aiche J. 2005;51:2599-608.

[50] Sun H, Zhang GS, Guo LJ, Shang DH, Liu HT. Effects of humidification temperatures on local current characteristics in a PEM fuel cell. J Power Sources. 2007;168:400-7.

[51] Abdullah AM, Mohammad AM, Okajima T, Kitamura F, Ohsaka T. Effect of relative humidity on temperature and current distributions within a segmented H2/Air PEM fuel cell. ECS Trans. 2011;35:293-302.

[52] Reshetenko TV, Bender G, Bethune K, Rocheleau R. Systematic studies of the gas humidification effects on spatial PEMFC performance distributions. Electrochim Acta. 2012;69:220-9.

[53] Brett DJL, Atkins S, Brandon NP, Vesovic V, Vasileiadis N, Kucernak A. Localized impedance measurements along a single channel of a solid polymer fuel cell. Electrochem Solid-State Lett. 2003;6:A63.

[54] Schneider IA, Kramer D, Wokaun A, Scherer GG. Effect of inert gas flow on hydrogen underpotential deposition measurements in polymer electrolyte fuel cells. Electrochem Commun. 2007;9:1607-12.

[55] Higier A, Liu HT. Effects of the difference in electrical resistance under the land and channel in a PEM fuel cell. Int J Hydrogen Energ. 2011;36:1664-70.

[56] Yoon YG, Lee WY, Park GG, Yang TH, Kim CS. Effects of channel and rib widths of flow field plates on the performance of a PEMFC. Int J Hydrogen Energ. 2005;30:1363-6.

[57] Hsieh S-S, Chu K-M. Channel and rib geometric scale effects of flowfield plates on the performance and transient thermal behavior of a micro-PEM fuel cell. J Power Sources. 2007;173:222-32.

[58] Goebel SG. Impact of land width and channel span on fuel cell performance. J Power Sources. 2011;196:7550-4.

[59] Sun W, Peppley BA, Karan K. Modeling the Influence of GDL and flow-field plate parameters on the reaction distribution in the PEMFC cathode catalyst layer. J Power Sources. 2005;144:42-53.

[60] Shimpalee S, Van zee JW. Numerical studies on rib & channel dimension of flow-field on PEMFC performance. Int J Hydrogen Energ. 2007;32:842-56.

[61] Peng LF, Lai XM, Liu DA, Hu P, Ni J. Flow channel shape optimum design for hydroformed metal bipolar plate in PEM fuel cell. J Power Sources. 2008;178:223-30.

[62] Wang XD, Zhang XX, Liu T, Duan YY, Yan WM, Lee DJ. Channel geometry effect for proton exchange membrane fuel cell with serpentine flow field using a three-dimensional two-phase model. Journal of Fuel Cell Science and Technology. 2010;7:051019.

[63] Manso AP, Marzo FF, Mujika MG, Barranco J, Lorenzo A. Numerical analysis of the influence of the channel cross-section aspect ratio on the performance of a PEM fuel cell with serpentine flow field design. Int J Hydrogen Energ. 2011;36:6795-808.

[64] Lu Z, Kim C, Karlsson AM, Cross JC, Santare MH. Effect of gas diffusion layer modulus and land–groove geometry on membrane stresses in proton exchange membrane fuel cells. J Power Sources. 2011;196:4646-54.

[65] Tüber K, Oedegaard A, Hermann M, Hebling C. Investigation of fractal flow-fields in portable proton exchange membrane and direct methanol fuel cells. J Power Sources. 2004;131:175-81.

[66] Liu HC, Yan WM, Soong CY, Chen F. Effects of baffle-blocked flow channel on reactant transport and cell performance of a proton exchange membrane fuel cell. J Power Sources. 2005;142:125-33.

[67] Thitakamol V, Therdthianwong A, Therdthianwong S. Mid-baffle interdigitated flow fields for proton exchange membrane fuel cells. Int J Hydrogen Energ. 2011;36:3614-22.

[68] Jang JY, Cheng CH, Huang YX. Optimal design of baffles locations with interdigitated flow channels of a centimeter-scale proton exchange membrane fuel cell. Int J Heat Mass Tran. 2010;53:732-43.

[69] Sun L, Oosthuizen PH, McAuley KB. A numerical study of channel-to-channel flow cross-over through the gas diffusion layer in a PEM-fuel-cell flow system using a serpentine channel with a trapezoidal cross-sectional shape. Int J Therm Sci. 2006;45:1021-6.

[70] Chiang MS, Chu HS, Chen CoK, Jian SR. Electrochemical reaction and performance of proton exchange membrane fuel cells with a novel cathode flow channel shape. J Power Sources. 2007;166:362-75.

[71] Xu C, Zhao TS. A new flow field design for polymer electrolyte-based fuel cells. Electrochem Commun. 2007;9:497-503.

[72] Kuo JK, Yen TH, Chen CK. Three-dimensional numerical analysis of PEM fuel cells with straight and wave-like gas flow fields channels. J Power Sources. 2008;177:96-103.

[73] Yan WM, Li HY, Chiu PC, Wang XD. Effects of serpentine flow field with outlet channel contraction on cell performance of proton exchange membrane fuel cells. J Power Sources. 2008;178:174-80.

[74] Kloess JP, Wang X, Liu J, Shi Z, Guessous L. Investigation of bio-inspired flow channel designs for bipolar plates in proton exchange membrane fuel cells. J Power Sources. 2009;188:132-40.

[75] Roshandel R, Arbabi F, Moghaddam GK. Simulation of an innovative flow-field design based on a bio inspired pattern for PEM fuel cells. Renew Energ. 2012;41:86-95.

[76] Min CH. Performance of a proton exchange membrane fuel cell with a stepped flow field design. J Power Sources. 2009;186:370-6.

[77] Wang XD, Huang YX, Cheng CH, Jang JY, Lee DJ, Yan WM, et al. An inverse geometry design problem for optimization of single serpentine flow field of PEM fuel cell. Int J Hydrogen Energ. 2010;35:4247-57.

[78] Chaparro AM, Martín AJ, Folgado MA, Gallardo B, Daza L. Comparative analysis of the electroactive area of Pt/C PEMFC electrodes in liquid and solid polymer contact by underpotential hydrogen adsorption/desorption. Int J Hydrogen Energ. 2009;34:4838-46.

[79] Song W, Hou JB, Yu HM, Hao LX, Shao ZG, Yi BL. Kinetic investigation of oxygen reduction reaction in sub-freezing acid media. Int J Hydrogen Energ. 2008;33:4844-8.

[80] Matsuoka K, Sakamoto S, Nakato K, Hamada A, Itoh Y. Degradation of polymer electrolyte fuel cells under the existence of anion species. J Power Sources. 2008;179:560-5.

[81] Merzougui B, Swathirajan S. Rotating disk electrode investigations of fuel cell catalyst degradation due to potential cycling in acid electrolyte. J Electrochem Soc. 2006;153:A2220.

[82] Uno M, Tanaka K. Pt/C catalyst degradation in proton exchange membrane fuel cells due to high-frequency potential cycling induced by switching power converters. J Power Sources. 2011;196:9884-9.

[83] Chen CY, Cha HC. Strategy to optimize cathode operating conditions to improve the durability of a direct methanol fuel cell. J Power Sources. 2012;200:21-8.

[84] Kim HT, Song KY, Reshetenko TV, Han SI, Kim TY, Cho SY, et al. Electrochemical analysis of polymer electrolyte membrane fuel cell operated with dry-air feed. J Power Sources. 2009;193:515-22.

[85] Song KY, Kim HT. Effect of air purging and dry operation on durability of PEMFC under freeze/thaw cycles. Int J Hydrogen Energ. 2011;36:12417-26.

[86] Pozio A, De Francesco M, Cemmi A, Cardellini F, Giorgi L. Comparison of high surface Pt/C catalysts by cyclic voltammetry. J Power Sources. 2002;105:13-9.

[87] Yuan X, Wang H, Colinsun J, Zhang J. AC impedance technique in PEM fuel cell diagnosis—a review. Int J Hydrogen Energ. 2007;32:4365-80.

[88] Natarajan D, Nguyen TV. Three-dimensional effects of liquid water flooding in the cathode of a PEM fuel cell. J Power Sources. 2003;115:66-80.

[89] Jeon DH, Kim KN, Baek SM, Nam JH. The effect of relative humidity of the cathode on the performance and the uniformity of PEM fuel cells. Int J Hydrogen Energ. 2011;36:12499-511.

[90] Ubong EU, Shi Z, Wang X. Three-dimensional modeling and experimental study of a high temperature PBI-based PEM fuel cell. J Electrochem Soc. 2009;156:B1276.

[91] COMSOL. Batteries and fuel cells module users guide. 2012.

[92] COMSOL. Chemical reaction engineering module users guide. 2012.

[93] Marr C, Li XG. Composition and performance modelling of catalyst layer in a proton exchange membrane fuel cell. J Power Sources. 1997;77:17–27.

[94] Toray industries Inc. Toray carbon fiber paper "TGP-H".

[95] Alhazmi N, Ingham DB, Ismail MS, Hughes KJ, Ma L, Pourkashanian M. Effect of the anisotropic thermal conductivity of GDL on the performance of PEM fuel cells. Int J Hydrogen Energ. 2013;38:603-11.

[96] Springer TE, Zawodzinski TA, Gottesfeld S. Polymer electrolyte fuel cell model. J Electrochem. Society. 1991;138.

[97] Wesselingh JA, Krishna R. Mass Transfer in Multicomponent Mixtures. 2000.

[98] M. J Assael SM, W. A. Wakeham. The viscosity and thermal conductivity of normal hydrogen in the limit of zero density. J Phys. Chem. Ref. Data. Vol. 15, No. 4, 1986.

[99] Munson Y, Okiishi. Fundamentals of fluid mechanics, third edition.

[100] Basu S, Wang C-Y, Chen KS. Phase Change in a Polymer Electrolyte Fuel Cell. J Electrochem Soc. 2009;156:B748.

[101] Wang L Husar A, Zhou TH, Liu HT. A parametric study of PEM fuel cell performances. Int J Hydrogen Energ. 2003;28:1263-72.

[102] Tao WQ, Min CH, Liu XL, He YL, Yin BH, Jiang W. Parameter sensitivity examination and discussion of PEM fuel cell simulation model validation. J Power Sources. 2006;160:359-73.

[103] Zhou TH, Liu HT. A 3D model for PEM fuel cells operated on reformate. J Power Sources. 2004.

[104] COMSOL. Introduction to COMSOL multiphysics. 2012.

[105] COMSOL. COMSOL multiphysics users guide. 2012.